4MSDS FINAL PROJECT REPORT

REPORT SUBJECT :
Study METIMAGE/3MI synthetic observation – Final Project Report
Simulation of Observation geometries and geolocation synthetic files for VII and 3MI

DISTRIBUTION : Thierry MARBACH (EUMETSAT)
Pepe PHILLIPS (EUMETSAT)
Jérôme RIEDI (LOA)
Jürgen FISCHER (FUB)
Jacques DESCLOITRES (ICARE)
Didier RAMON (HYGEOS)

INFORMATION : A study performed by University of Lille /Freie Universität Berlin with support from HYGEOS-Earth Observation

REPORT EDITOR : J. RIEDI VISA :

REF. : LOA/4M-SDS-FR01/JR

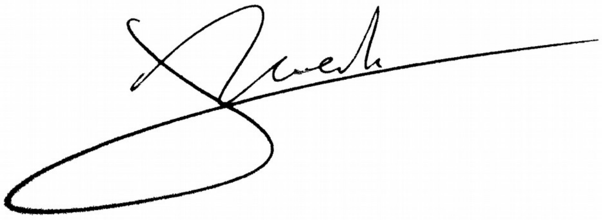

REPORT DATE: 4th February 2015
LAST UPDATED: 22nd April 2015

Revision history

- Revision 01 : 4th February – Initial delivery
- Revision 02 : 25th March - Technical corrections
- Revision 03 : 1srt April - Updated VII full resolution illustration and added AVHRR comparison.
- Revision Final : 22nd May - Final revision after EUMETSAT review and last comments

THIS PAGE INTENTIONNALY LEFT BLANK.

ACKNOWLEDGEMENTS

The study responsible and report editor would like to express its most sincere acknowledgements to the entire team who contributed to this effort and resulted in the high quality of the delivered synthetic dataset. This includes all members of LOA, ICARE and FUB identified in the proposal but special thanks are also due to :

- F. Thieuleux from LOA for its dedicated support to orbit simulation, data format definition, file structure creation and general engineering support,
- M. Compiègne from HYGEOS (formerly at LOA) for outstanding achievement regarding radiative simulator setup, computational optimisation and general dedication to the project
- L. Doppler for its long term motivation and dedication to the project that has extended far beyond its official duties
- N. Henriot from ICARE for continuous, proactive and reactive support in provision of ancillary data and computational resources
- P. Phillips and T. Marbach for their exceptionally constructive study monitoring approach and constant feedback. acknowledgements

Thanks to all,

Sincerely

Jérôme RIEDI

Table of Contents

Figures Index

Index of Tables

EXECUTIVE SUMMARY

This study "EPS Second Generation – Test data for the METimage and 3MI instruments" has been performed to provide realistic synthetic test data for the VII (METimage) and 3MI instruments in support to the ground processor development. Given the EPS-SG orbit and instrument viewing geometries, top of the atmosphere (TOA) radiances for the full range of representative atmospheric and surface conditions have been generated for each instrument.

For this purpose a full orbit propagation has been performed based on orbital parameters provided by EUMETSAT and corresponding to the 3 test orbits. Observation geometries (sensor reference frame) for the two instruments have been simulated based on instrument sampling characteristics (instantaneous FOV, scan period and limit angles for VII, spectral sampling chronograph for 3MI). Geolocation and sampling geometries have served as input to radiative transfer simulator in which surface and atmosphere (clouds, aerosols, gas) have been realistically described based on ancillary information obtained for dates and time of required simulation (among which AVHRR products for clouds, MACC reanalysis for aerosols, ECMWF reanalysis for atmospheric state, MODIS albedo climatology). The simulated TOA radiances have been generated at level 1b, equivalent to the calibrated and geolocated measurements made by each instrument.

Outcomes of the study consists of a synthetic dataset composed of several hdf files (herein referred as granules) each corresponding to approximately 5 minutes of data acquisition. Information for geolocation and sampling geometries, ancillary input to simulators and simulated synthetic radiances are provided in separate files and for each instrument.

1 Introduction

1.1 Scope

This study "EPS Second Generation – Test data for the METimage and 3MI instruments" has been performed to provide realistic synthetic test data for the METimage and 3MI instruments in support to the ground processor development. Given the EPS-SG orbit and instrument viewing geometries, top of the atmosphere (TOA) radiances for the full range of representative atmospheric and surface conditions had to be generated for each instrument. The simulated TOA radiances have been generated at level 1b, equivalent to the calibrated and geolocated measurements made by each instrument.

This final report present the simulation assumptions for the instrument observations and sampling geometries, the numerical models used for simulations of TOA radiances and the ancillary data sets used to described the atmospheric and surfaces properties work accomplished study and provides documentation for the associated deliverables.

1.2 General approach

The METimage instrument will be a passive cross-track scanning imaging spectro-radiometer measuring reflected solar and emitted terrestrial radiation in the visible to infrared spectral domain between 0.445 and 13 µm. It will yield from a low earth orbit a moderate spatial resolution of 0.5 km over a swath with a minimum width of 2800 km. Derived from a whisk-broom scanner principle, the instrument records a small number of image lines simultaneously during each scan across-track (38 lines for the 500m channels). By proper selection of rotation frequency, the scanner produces a gap-free scan pattern on ground. As an output of the present study the single scan period has been adjusted with respect to the initial SOW and set to 2.843 sec. Output is an image sampled at discrete locations, the sampling within each line is performed at constant scan angle increments.

The 3MI instrument will be a wide field of view VIS, NIR and SWIR imager consisting of two separate optical heads for the VIS/NIR and NIR/SWIR. It will provide multi-viewing capability with 14 views (fore and aft) of the same target and polarization measurements in 9 of its 13 spectral channels. The VIS/NIR field of view of about 114° will yield a 2200 km minimum swath width with no gaps between measurements and on-ground spatial sampling of 4 km at nadir. Currently the SWIR along-track field of view of 3MI is required to be at least half-size of the VNIR, requiring double frame-rate for SWIR acquisition to achieve the required 14 views (see details of sequence acquisition chronograph given by Figure 2.7).

Further details about the VII and 3MI can be found at :
http://www.eumetsat.int/website/home/Satellites/FutureSatellites/EUMETSATPolarSystemSecondGeneration/EPSSGDesign/index.html

Note that this study does not intend to provide multi-directional product for the 3MI as it would require either crude assumption for the multi-angle collocation or the development of a specific processor which falls outside of the scope of the intended studies. If deemed necessary, it is suggested that a nearest pixel collocation approach could be used to create a multi-directional level 1c product similar for what has been historically provided for the different POLDER missions but this question is not being addressed by the current study.

1.3 Report organisation

Following this introductory section we provide hereafter relevant elements for the simulation methodology and assumption for the sampling geometries (section 2), followed by a description of the numerical tools for simulation of TOA radiances (section 3). A description of the ancillary data sources used as input to radiative transfer simulation and dataset format is provided in section 4. We then illustrate the simulated datasets and provide a complete list of delivered data in section 5.

It should be noted that some detailed specifications or assumption contained in intermediate reports produced for tasks 1, 2 and 3 as described in the SOW might have been modified over the course of the study. These points will be clearly identified within this report and concern mainly the sampling assumption for 3MI (position of the SWIR focal plane) and VII (250 m sampling dropped, scan period adjusted) as well as the acquisition chronograph details for 3MI (channel ordering).

2 Orbital and instrument sampling simulation

2.1 Simulation method and assumptions

Creating a database for EPS-SG orbit and scan geometry has been subdivided into two sub tasks. First, the orbital parameters for the EPS-SG platform itself and the viewing geometry of the 3MI and METImage sensor have been generated. Second, the footprint of each spatial and spectral pixel on the realistic surface of the earth have been established.

It had been initially proposed to establish the orbital parameters based on the provided AVHRR data which could have been interpolated to provide orbital position and parameters of EPS-SG at required time-stamps. However, we have finally performed a full propagation of the orbit based on TLEs provided for the example orbits. This allows for a more generic observation simulator in which in particular attitude laws can be specifically defined.

After the spacecraft position in the orbital plane is established, application of the Local Nadir Pointing and yaw steering laws [RD-1] from the SOW can be applied to the spacecraft reference frame. These provide the attitude parameters of the platform reference frame with respect to the orbital reference frame. Once the attitude is known, we can then compute the viewing geometry and cone of sight for each spatial and spectral pixel first in the spacecraft frame and then with respect to the orbital reference frame by applying roll, pitch and yaw rotation.

Using these information, we can then compute a footprint polygon for each spatial and spectral pixel within the high spatially resolved DEM ACE-2 data set and produce correction for the ground pixel elevation over the reference ellipsoid.

It should be noted that spectral acquisitions can not be performed simultaneously for 3MI so that orbital parameters and therefore viewing geometries must be determined for each sequence and each of the 13 [1] 3MI channels separately. Parameters of the Stokes vector are the requested quantity for this study so knowledge of radiance for each polarization filter for a given spectral channel is not being simulated. Therefore only one set of observation geometry is provided for the 3 polarisers of any given spectral channel.

It is also stressed out here that VNIR and SWIR sampling for 3MI are not identical as double frame-rate are needed in the SWIR channels to meet the 14 multi-viewing directions requirements under the constraint that the SWIR FOV along track will be half of the VNIR one.

The resulting METimage sampling geometries and associated parameters are finally provided in a swath oriented dataset similar to existing AVHRR data currently distributed by EUMETSAT using hdf5 file format.

The resulting 3MI sampling geometries and associated parameters are provided in a sequence oriented dataset organized by sequence number and spectral channel,

1 Strictly speaking only 12 different spectral bands are acquire but the 910 nm channel is duplicated on the VIS/NIR and the SWIR optical head with different FOV hence 13 channels are actually sampled with different geometries and simulated here.

using similar hdf5 file format.

2.1.1 Orbital elements assumptions

According to the SOW, simulation have been performed for the 3 test orbits which TLE were provided by EUMETSAT. The corresponding parameters for orbit propagation are summarized hereafter :

```
##################################################
METOPA TLE for orbit 1 and 2
1 29499U 06044A   07255.36322917  .00000000  00000+0 -14665-1 0 00016
2 29499  98.6961 313.7788 0001113  97.4911  28.4762 14.21512221   -10

Epoch :                                  2007 255.36322917
Inclination :                            98.6961
Right Ascension of Ascending Node :313.7788
Eccentricity :                           0.0001113
Argument of Perigee :                    97.4911
Mean Anomaly :                           28.4762
Mean Motion :                            14.21512221

###################################################
METOPA TLE for orbit3
1 29499U 06044A   08054.36531250  .00000000  00000+0 -17175-1 0 00015
2 29499  98.6681 115.0874 0001287  95.2239  21.2140 14.21526020   -12

Epoch :                                  2008 054.36531250
Inclination :                            98.6681
Right Ascension of Ascending Node :      115.0874
Eccentricity :                           0.0001287
Argument of Perigee :                    95.2239
Mean Anomaly :                           21.2140
Mean Motion :                            14.21526020

####################################################
```

The Semi-Major axis has been kept constant for all three orbits with a value of 7195605.347 meters.

1rst orbit of the SOW : Simulation range from 2007/09/12 at 08:43 to 10:23
2nd orbit of the SOW : Simulation range from 2007/09/12 at 10:23 to 12:05
3rd orbit of the SOW : Simulation range from 2008/02/23 at 08:46:02.784Z to 10:29

Note that exact end time of each orbit (as far as acquisition end is concerned) depends on assumed scan rate for VII and wheel period of 3MI so the end time limit is only indicative.

2.1.2 Definition of reference frames and observation geometries

In this report, definitions of angles and reference frame are consistent with the SDP toolkit conventions.

Figures 2.1 and 2.2 (page 21) illustrate respectively the Earth Centred Rotating (ECR), Earth Centred Inertial (ECI) reference frame which serve for computation of various vectors internally to the SDP toolkit and expression of spacecraft state vector. Figure 2.3 represents the Orbital reference frame in which the spacecraft attitude (roll, pitch and yaw) are provided.

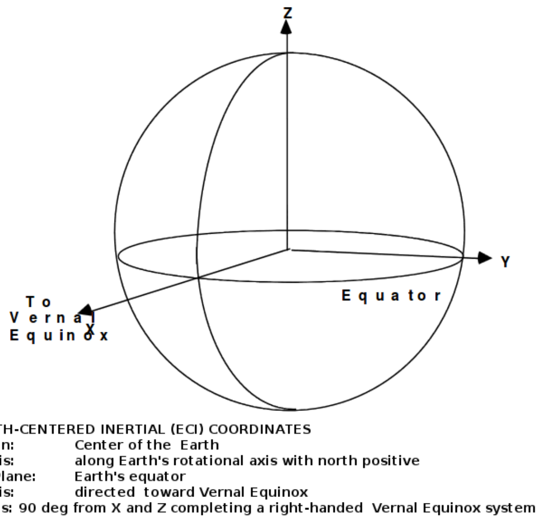

Figure 2.1: Earth Centred Inertial (ECI) Coordinates

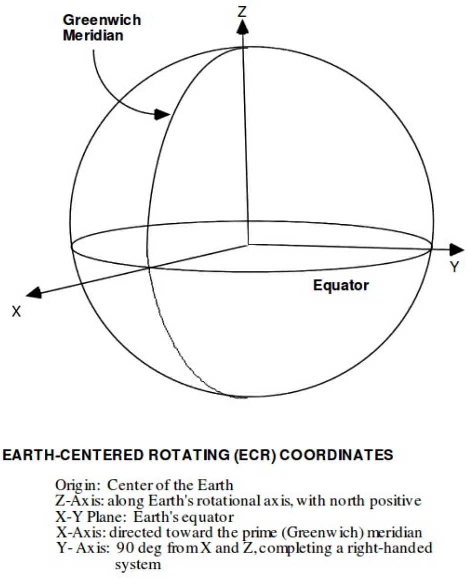

Figure 2.2: Earth Centred Rotating (ECR) Coordinates

The SDP Toolkit provides functions to operate coordinates change between the three different reference frames. This allows to handle easily the various direction vectors for the sun and the spacecraft from and to any of the coordinates and provides a robust framework for our simulation.

In this report, the observation (sensor viewing) angles and sun angles are defined as presented on figures 2.4 and 2.5.

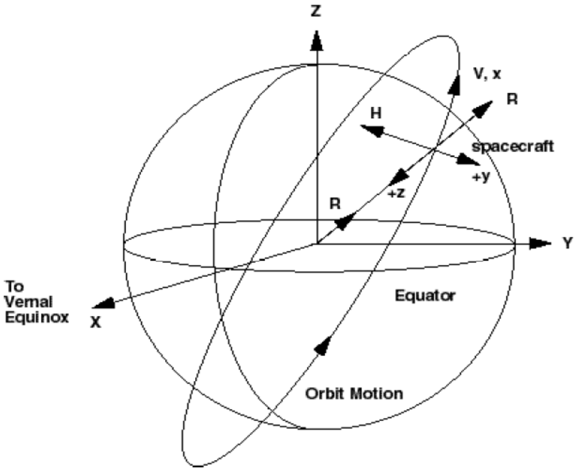

X, Y, Z are inertial coordinates. x, y, z are orbital coordinates, defined as follows:

Origin: Spacecraft Center of Mass
x-z plane: Spacecraft orbital plane

+y (pitch) - Axis: oriented normal to the orbit plane with positive sense opposite to that of the orbit's angular momentum vector H.

+z (yaw) - Axis: positively oriented earthward parallel to the satellite radius vector R from the spacecraft center of mass to the center of the Earth

+x (roll) - Axis: positively oriented in the direction of orbital flight completing an orthogonal triad with y and z.

Figure 2.3 Relationship between Earth-Centred Inertial (ECI) coordinates and Orbital Coordinates

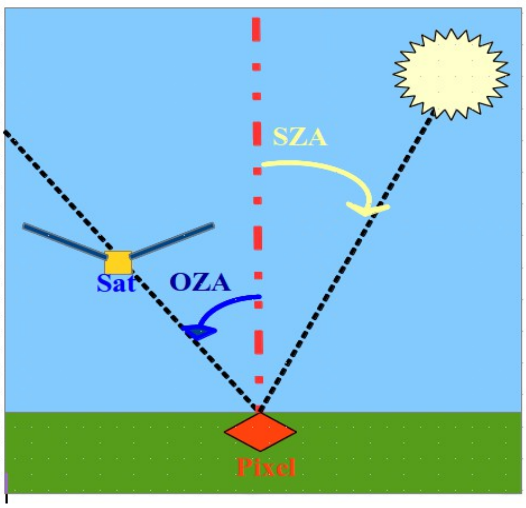

Figure 2.4: Definition of Observation Zenith Angle (OZA, sensor viewing zenith angle) and of Sun Zenith Angle (SZA). The angle is defined from the pixel, referring to the Earth vertical at the pixel point. 0° is the Earth vertical (pixel at the nadir).

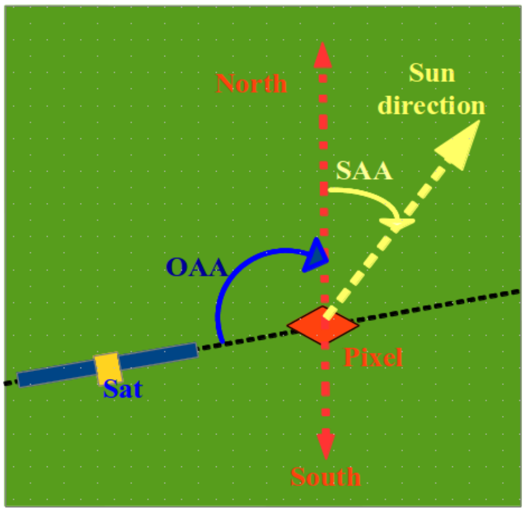

Figure 2.5: Definition of Observation Azimuth Angle (OAA, sensor viewing azimuth angle) and of Sun Azimuth Angle (SAA). The angle is defined from the pixel, referring to the North-South angle at the pixel. 0° is the North, positive direction is clockwise.

2.1.3 Simulation methodology and tools

The simulation are performed in three steps :

- Propagation of the platform orbit using TLE provided by EUMETSAT
- For each time stamp (either VII scan time or 3MI spectral channel acquisition time) :
  - determination of attitude parameters of the spacecraft reference frame with respect to the orbital reference frame following yaw-steering law provided by SOW (see example for sample orbit #1 on figure 2.6 below).
  - determination of look direction for individual instrument IFOV through simulation of scan geometries in the spacecraft reference frame and later in the orbital reference frame through application of attitude laws
  - computation of ground sampling and associated sun and view geometries on the ellipsoid assuming the WGS84 model
- Determination of ground samples altitude and correction of geolocation field using ACE2 dataset.

To perform step 1 and step 2, the tools and libraries provided by the Science Data Processing Toolkit distributed[2] by NASA. The full documentation is available online at the distribution site [Ref.3] and a technical report [Ref.4] provides the theoretical basis for the toolkit implementation.

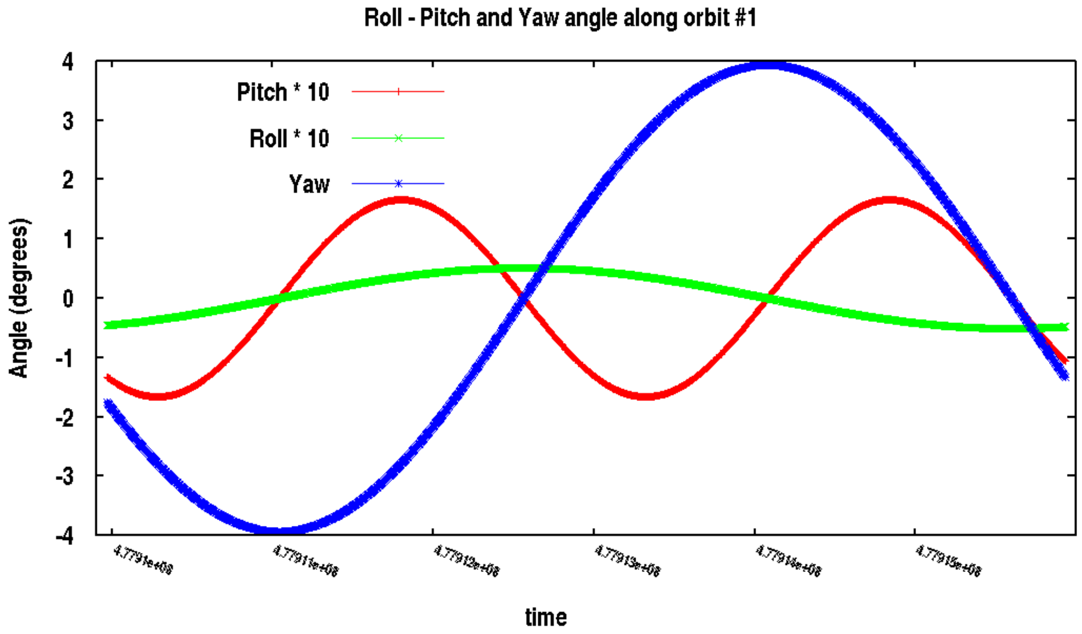

Figure 2.6 : Example of Roll, Pitch and Yaw angles computed along the first reference orbit as function of time (TAI in s). Note that roll and pitch angles have been multiplied by 10 for visualization purpose but that yaw angle has by far the largest amplitude.

2 http://newsroom.gsfc.nasa.gov/sdptoolkit/toolkit.html

For information, the main functions used for the simulation are :

- for computing of the intersection between a view vector referenced in the orbital and the reference ellipsoid :
  PGS_CSC_GetFOV_Pixel(spacecraftTag,NBPIX_SCAN, asciiUTC,offsets, EarthEllipsTag,accurFlag, pixelUnitvSC,offsetXYZ, latitude,longitude, pixelUnitvECR,slantRange, velocDoppl**);**

- for computing the sun position with respect to Earth centred inertial reference frame (ECI) :
  PGS_CBP_Earth_CB_Vector(NBPIX_SCAN, asciiUTC, offsets, cbId, SolarvECI**);**

- for computing the viewing and sun geometries at a point on the surface of the reference ellipsoid :
  PGS_CSC_ZenithAzimuth(pixelUnitvECR, latitude, longitude,altitude, vectorTag, zenithOnlyFlag, refractFlag, sensor/sun_zenith, sensor/sun_azimuth,refraction**);**
  Note that the same function is being used to compute the zenith and azimuth of a vector at a look point, sun and view geometries being computed by providing either the look vector (retrieved using **PGS_CSC_GetFOV_Pixel)** or the sun vector (retrieved using **PGS_CBP_Earth_CB_Vector)**.

- for determining sub-satellite point location, spacecraft altitude and projection of spacecraft velocity vector projected on the ground :
  PGS_CSC_SubSatPoint(spacecraftTag,nb_subsat_interval, asciiUTC,ssp_offsets, EarthEllipsTag,velFlag, ssp_latitude, ssp_longitude, sc_altitude, ssp_veloc**);**

Details of the above function call and parameters can be found in the documentation of the geolocation tools within the SDP Toolkit documentation which can be found at : http://newsroom.gsfc.nasa.gov/sdptoolkit/docs/UG_geo_location.pdf

The following documentation can be referred to for readers interested in exact implementation and usage information :

[Ref.1] HDF-EOS Interface Based on HDF5, Volume 1: Overview and Examples
http://newsroom.gsfc.nasa.gov/sdptoolkit/docs/HDF-EOS5_UG.pdf

[Ref.2] HDF-EOS Interface Based on HDF5, Volume 2: Function Reference Guide
http://newsroom.gsfc.nasa.gov/sdptoolkit/docs/HDF-EOS5_REF.pdf

[Ref.3] Release 7 SDP Toolkit Users Guide (5.2.18)
ftp://edhs1.gsfc.nasa.gov/edhs/sdptk/latest_release/UG_intro.pdf
ftp://edhs1.gsfc.nasa.gov/edhs/sdptk/latest_release/UG_proc_cntl.pdf
ftp://edhs1.gsfc.nasa.gov/edhs/sdptk/latest_release/UG_geo_location.pdf
ftp://edhs1.gsfc.nasa.gov/edhs/sdptk/latest_release/VDD_prod_descrp.pdf
ftp://edhs1.gsfc.nasa.gov/edhs/sdptk/latest_release/UG_appendices.pdf

[Ref.4] "Theoretical Basis of the SDP Toolkit Geolocation Package for the ECS", Project Technical Paper, Peter D. Noerdlinger and Larry Klein, May 1995. Doc ref : 445-TP-002-002
http://edhs1.gsfc.nasa.gov/waisdata/tks/pdf/tp4450202.pdf

2.1.4 Specifics of 3MI and VII scanning/observing geometries

For both sensors, the viewing geometries are computed by determining viewing vector of any given detector of the focal plane in the Spacecraft reference frame and then by determining the geocentric latitude and longitude of this line of sight intercept with the Earth ellipsoid (using WGS84 model). This provides the geocentric longitude and latitude of the “noDEM” data. The algorithm of DEM correction hereafter above described uses the noDEM data to compute the actual coordinates of the pixels.

2.1.4.1 Specifics to VII sampling :

The VII single detector elements are considered to consist of an array of 38 pixels for the 500 m channels. The view vectors are first computed at nadir view in the spacecraft reference frame and are then rotated around the scan axis at a period of 2.843 s and sampled at regular time interval to provide 3264 samples (500m channels) distributed symmetrically about the geocentric direction. The pixel number 1 (across track) is the furthest point from the nadir observed on the left side with respect to spacecraft moving direction. The pixels number 1632 and 1633 are the closest to the nadir trace (observation zenith angle OZA close to 0°), and, the pixel number 3264 is the furthest in the right direction. All the 3264 across track samples are measured at a different time, therefore, this time is stored in the hdf dataset TAI_Time.
Note that METImage also initially intended to acquire some spectral channels at 250 m resolution using 76 pixels detectors array. However those higher resolution channels have been discarded during study realisation so only 500 m sampling remain described in this final report. However the 250 m channels geolocation and observation geometries fields could be obtained through a simple interpolation to obtain 6528 samples across track.

The following values have been used for simulation of the METImage field of views and associated observation geometries. Note again that the 250 m observations have not been provided in the delivered dataset but are included in the simulator so could be easily produced if deemed necessary.

Resolution (at geodetic nadir)	500 m
Number of samples per scan along Track	38
Number of samples across Track	3264
Across-track total field of view (degrees)	110
Scan period (second)	2.843
Equivalent single pixel along track IFOV (radians)	0.000605292
Equivalent single pixel across-track IFOV (radians)	0.000588193

Table 2.1: Simulation parameters for the VII/METImage scanner

2.1.4.2 Specifics to 3MI sampling :

The simulation of 3MI viewing and sampling geometries are performed slightly differently than for VII because observation principle of the 3MI involves instantaneous acquisition of 2D frame. Therefore, the 3MI sampling geometries are computed assuming a 2D frame sampling performed at regular time interval instead of the almost continuous acquisition obtained from VII scanning as explained above. Given the 3MI requirements provided in the SOW (14 directions multi-viewing capability with 114° FOV for the VNIR channels) and the EPS-SG altitude, approximately 129 sequences need to be acquired for each spectral channel along the sun illuminated orbit portion. In addition all spectral channels shall be acquired within 7 seconds. These constraints have been used to distribute temporally the frame acquisitions and obtain their time stamps and match them with corresponding EPS-SG orbital parameters (spacecraft state vector and attitude). The current 3MI chronograph for acquisition time stamps is provided in Figure 2.7 (page 27).From these, the viewing geometries and other required parameters can be easily derived for all pixels of the 3MI FOV in a similar way to VII samples.

The individual VNIR and SWIR single field of view observing directions are determined assuming the following dimensions for the arrays and equivalent focal length computed to provide the require resolution of 4 km at nadir for both optical heads. For 3MI, all across-track pixels are observed at the same time, but different spectral channels are observed at different instant. Therefore, the time of observation is stored in the hdf files in the dataset TAI_Time.

The following values have been used for simulation of the 3MI VNIR and SWIR arrays field of views and associated observation geometries. Note again that SWIR array is shifted 85 pixels from the centre origin of the VNIR array to obtain coverage of the northern portion of the VNIR FOV by the SWIR FOV.

Optical head	VNIR	SWIR
X Dimension – Along Track	512	256
Y Dimension – Across Track	512	500
Detector Pixel size (meters)	26. 10-6	30. 10-6
Equivalent focal length (micrometer)	5.369 10-3	6.195 10-3
Wheel rotation (3MI) period (seconds)	5.5	5.5

Table 2.2: Simulation parameters for the 3MI optical heads

For 3MI, spectral acquisition are not simultaneous. Therefore spatial sampling is different for each spectral channel. For polarized channels however, it was assumed that the 3 polarisers are almost coincident in time and only the central polariser acquisition geometries are simulated.

In addition, the VNIR and SWIR channels are not acquired using the same assembly of optical head / focal planes and detector arrays have different sizes. So the viewing geometries and fields of view for VNIR and SWIR arrays will not be similar. In addition, a second SWIR acquisition is performed in addition to that synchronized with the VNIR one. This second SWIR acquisition will not be coincident either in time or space with any VNIR observations.

Simulation are performed under assumptions of a 5.5 seconds wheel rotation period and a 4 wheel turn acquisition sequence. The first wheel turn allows acquisition of both VNIR (VIS) and SWIR channels. The third wheel turn allows a second SWIR channels ensemble acquisition. The second and fourth wheel turn are free wheeling (no acquisition).

The acquisition sequence chronograph is detailed hereafter in figure 2.7 page 27 and results in a multi-angular sampling of at least 14 viewing direction being available per ground target consistent with the 3MI MRD.

VIS SLOTS	TIME STAMP (TS) VIS		SWIR SLOTS	TS Turn 1	TS Turn 2	TS Turn 3	TS Turn 4
shutter	0	0	shutter	0	5.5	11	16.5
754	0.25	0.25					
910	0.5	0.5	910SWIR	0.5	6	11.5	17
763	0.75						
865P3	1		1650P3				
865P2	1.25	1.25	1650P2	1.25	6.75	12.25	17.75
865P1	1.5		1650P1				
490P3	1.75						
490P2	2	2					
490P1	2.25						
670P3	2.5		2130P3				
670P2	2.75	2.75	2130P2	2.75	8.25	13.75	19.25
670P1	3		2130P1				
410P3	3.25						
410P2	3.5	3.5					
410P1	3.75						
555P3	4		1370P3				
555P2	4.25	4.25	1370P2	4.25	9.75	15.25	20.75
555P1	4.5		1370P1				
443P3	4.75						
443P2	5	5		5	10.5	16	21.5
443P1	5.25			5.25	10.75	16.25	21.75
-> back to shutter		5.5		5.5		16.5	

Figure 2.7: Chronograph giving time acquisition sequence for VNIR and SWIR channels. The table is based under assumption of 5.5 s wheel rotation period and assumes 4 turns per full sequence.

2.1.5 Approach for implementation of DEM correction

The DEM correction is made in a final step by iteratively looking at the intercept of each line of sight with the DEM surface: We first define the instant line of scan in the (Lon,Lat) plane (see figure 2.8, left). The tangent point of this plane with the Earth Ellipsoid is the point P_{Ell}. On this instant line of scan, we define two points for each pixel: The point $\mathbf{P}_{Ell}$ (corresponding to the pixel's projection without DEM, on the Earth's

Ellipsoid of altitude = 0), and, the point P_{Max} that is the pixel's projection for a ground altitude of altmax = 10 km.
In a second step, we read the altitude of the DEM on the segment [P_{Max} P_{Ell}]. This is shown in grey-blue on the right panel of figure 2.8. The algorithm of DEM correction compares the altitude of the observation (following the line in green on the second picture: the altitude of the line of sight for the observation zenith angle – OZA - of the pixel) to the altitude of the DEM. We starts from the point P_{Max} and move in the direction of P_{Ell}. The first point of intersection between the green line and the DEM line, is the point P_{DEM}, namely the centre of the pixel of the observation projected on the DEM. We read the coordinates (lon,lat) of P_{DEM}, these are the new coordinates after DEM correction of the pixel's centre.
The DEM correction leads always to a shift in direction of the nadir trace of the satellite, on the instantaneous line of scan, if the DEM has positive altitudes (what is mostly the case).
We can afterwards verify if this distance is well computed by comparing the distance of the shift due to the DEM correction: dist_corr to a theoretical distance named dist_theo. This theoretical distance is computed with the tangent method: For a pixel at an altitude alt_pix, the distance dist_theo between P_{DEM} and P_{ELL} is equal to the tangent of the observation zenith angle OZA times the altitude alt_pix of the corrected pixel:
dist_theo = tan(OZA)*alt_pix.
Figures 2.18d, 2.19d and 2.20d present the differences in meters between the real shift distance dist_corr of the algorithm of DEM correction and the theoretical distance dist_theo obtained with the tangent method. The difference between dist_theo and dist_corr is always below the value of 100 m except for some rare cases on mountains at the limit of the scanned zone (over the Turkey for example) where the difference can reach the value of 1km (less than 1 pixel for this part of the scan).
“dist_corr” is presented on figures 2.18c, 2.19c and 2.20c. Note, that the distance of the shift increases with the height of the mountains and with the value of the observation zenith angle OZA. For Europe (alt_dem < 5km) and for VII (OZA < 70°) => dist_theo < 30 km, that means that the curvature of the Earth can be neglected (dist_theo < (Earth radius)/200.
Figures 2.18a, 2.19a and 2.20a represent the altitude in m of the DEM taken directly from ACE2. The difference between the altitude of the pixels corrected by the algorithm of correction and the altitude taken directly from ACE-2 is presented on Figure 2.18b, 2.19b and 2.20b: alt_4MSDS – alt_ACE2 in m. One can see that the difference between the altitude in the 4MSDS data and the altitude of ACE2 is mostly smaller than 1 m and is never larger than 3 m.

The resolution of the DEM correction is tunable. For the data provided in this study, we chose a resolution of 20 points per km for the instantaneous line of observation, namely 2 points per ACE2-DEM pixel.
Figure 2.19 and Figure 2.20 (page 45/46) illustrate the effect of the DEM correction for VII in a mountain region (Piz Bernina in the Swiss Alps, 4000 m of altitude) at the West part of the scan, for an OZA (Observation Zenith Angle) of 50°. We visualize a shift between the non corrected pixels (red) and the DEM-corrected pixels (green) in direction of the satellite track (in direction of the East). Note, that the higher are the

mountains, the larger is the switch. Figures 2.41 and Figure 2.42 (page 62/63) show the same for 3MI.

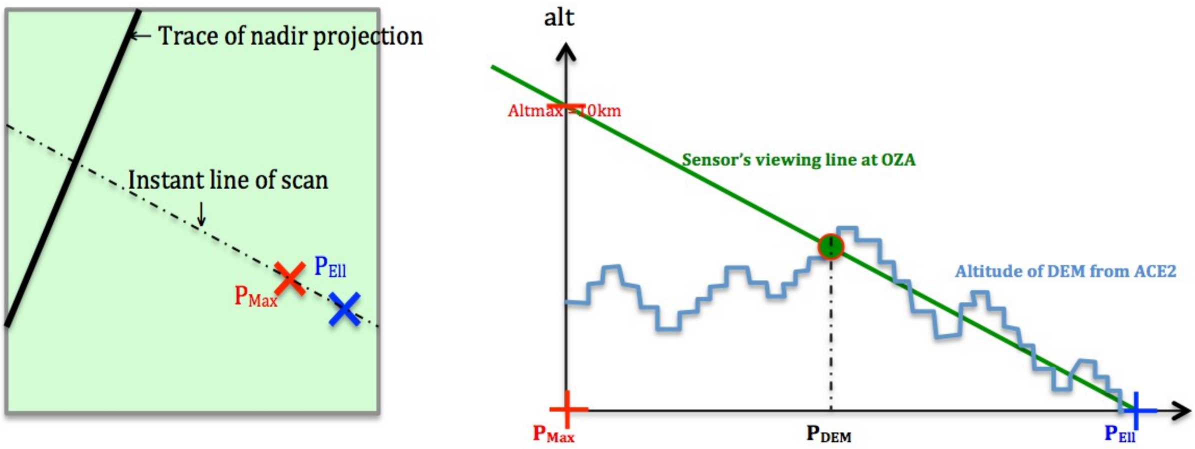

Figure 2.8 : Schematic of the line of sight along which the intersection with DEM surface is being searched.

2.1.6 Evaluation of simulation correctness

Several evaluation criteria have been used to guarantee fidelity of simulated orbits and scan geometries :

– simulated orbits have been checked against initial AVHRR (Spacecraft state vector and ground track position) and against other simulations performed online using Ixion software (http://climserv.ipsl.polytechnique.fr/ixion.html)

– for 3MI : fields of view orientation on the ground and growth with view angle have been evaluated by similarity with POLDER1/ADEOS1 data

– for VII : scan pattern (pixel growth with view angle, overlapping scans) have been checked for internal consistency and by similarity with MODIS/Terra scan patterns

– for VII : scan pattern on the ground (swath) has been compared to corresponding AVHRR swath (see Figures 2.43 to 2.48).

– for 3MI and VII : it has been checked that central pixels of all 2D scans (theoretical geodetic nadir looking IFOV) corresponded with view sensor zenith of 0.0 on the ground.

– Illustration of most of the simulated datasets (geolocation fields, observation geometries fields) have been inspected for anomalous behaviour (figures are provided in section 2.3 starting page 36).

Since AVHRR has a different scan pattern than VII, point to point matching of AVHRR and VII IFOV is not possible for evaluation of our simulation. However from the above analysis we concluded that our simulation approach and simulated data were valid within the requirements and the scope of the present study.

2.1.7 Simulation granularity and provided data files.

Due to (i) spatial resolution of VII (500 m) and (ii) multidirectional nature of 3MI observation with non simultaneous spectral acquisition, the generated data volume can not be kept within a single file. Therefore, VII and 3MI geolocation-observation geometries files have been produced for several granules constituting of the full orbit.

For VII, geolocation files are produced for each 284.3 seconds of continuous acquisition corresponding to 100 scans of VII acquisition.

For 3MI, geolocation files are produced for 14 consecutive acquisition sequences (granules) corresponding to 308 seconds (approximately 5 minutes).

Each of these 5 min (approximately) orbit portions simulated is called a granule hereafter.

***Note** : we would like to note here that potential synchronization of 3MI wheel speed might allow to produce temporally coincident VII and 3MI data granules. This would be achieved by fine tuning the 3MI wheel rotation period so that an integral number of 3MI sequence could be acquired during an integral number of VII scans. This might be difficult to achieve in practice but could help in referencing simultaneous 3MI and VII observations.*

The figures in the last part of this section (figures 2.49 to 2.55) illustrate computations of sun and viewing geometries for VII and 3MI observations simulated on 2007-09-12 starting at 08:43:03 UTC. Data have been extracted from the following simulated files :

EPS-SG_3MI_GEOLOC_2007-09-12T08:43:03_V01.00.he5
EPS-SG_VII_GEOLOC_2007-09-12T08:43:03_V01.00.he5
EPS-SG_3MI_GEOLOC_2007-09-12T08:43:03_DEM_V01.00.he5
EPS-SG_VII_GEOLOC_2007-09-12T08:43:03_DEM_V01.00.he5

The file format is using hdfeos5 standard which is fully compatible with hdf5 format and allows additional information on swath and internal organisation of datasets to be provided within the file using self documented standard.

Noticeable changes with respect to initial SOW for the dataset :

- for VII and relying on information provided by EUMETSAT, continuity of observations along track could not be obtained with a scan period of 3s. After discussion with EUMETSAT the scan period for VII has been changed to a value of 2.843 s which now provides a continuity of observation without any gap between two consecutive scanlines at nadir. This change has been approved by EUMETSAT.
- An attempt to adjust the SWIR array position in the focal plane has been made during the project by shifting the central position of the SWIR detector to cover the North of the VIS FOV. Following final recommendation by the 3MI SAG and EUMETSAT the simulated dataset has been finally produced with a SWIR array position centred on the VIS array central position as initially suggested in the SOW.

2.2 Description of the GEOLOCATION datasets in hdf files

All files provided for VII and 3MI simulated datasets are provided in hdf5 format augmented with hdfeos5 attributes. Data are stored in different encoding (8, 16 or 32 bits) which are internally documented in the files through specific attributes. Equation to transform file counts to physical values are also specified and provided as data attributes within the hdf5 files (equation, scale_factor, offset).

2.2.1 Instrument METImage (VII).

2.2.1.1 Naming convention for the hdf files.

VII geolocation files follow the following naming convention :

EPS-SG_VII_GEOLOC_AAAA-MM-DD**T**HH-mm-ss**_V**p.p**.he5**

with AAAA-MM-DDTHH-mm-ss, the instant of the beginning of the segment, namely: AAAA= the number of the year (4 digits) / MM = the number of the month (2 digits) / DD = the number of the day (2 digits) / HH = the number of the hour (2 digits) / mm = the number of the minute (2digits) / p.p = the dataset revision number.
Example: ***EPS-SG_VII_GEOLOC_2007-09-12T08-43-03_V1.4.he5*** *is the hdf file for VII, for the orbit's segment of the 12th of September 2007, starting at 8H43mn03sec (UTC), first version of processing.*

2.2.1.2 Datasets folders

Ground_Track

The folder /Ground_Track in the hdf files contains information about the satellite position: Satellite altitude (SC_Altitude), Satellite Attitude (SC_Attitude) given as roll, pitch and yaw Euler angles, satellite nadir projection on the Earth's ellipsoid (SSP_Longitude, SSP_Latitude), the time associated to the satellite position (SSP_TAI_TIME), projection of the satellite speed vector (N, E, Doppler velocity) on the Earth's ellipsoid (SSP_Velocity_NE_components).

Dataset name	Description and units	Dimension
SC_Altitude	Altitude of the satellite in m	1-D (2Tseg) vector Tseg = time of the segment in s
SC_Attitude	Attitude of the platform provided as roll, pitch and yaw angles expressed in Orbital reference frame.	2-D (2Tseg x3) vector
SSP_Latitude	Geodetic Latitude of the satellite in degrees (positive North)	1-D (2Tseg) vector
SSP_Longitude	Geodetic Longitude of the satellite in degrees (positive East)	1-D (2Tseg) vector
SSP_TAI_Time	International Atomic Time in s (since the 1st January 1993 0:00 UTC)	1-D (2Tseg) vector
SSP_Velocity_NE_components	Vector speed in m/s (East,North, Doppler) of the trajectory of the projection of the satellite on the Earth's Ellipsoid	2-D (2Tseg x 3) vector

Table 2.3 : List and description of orbit track descriptor datasets. These SDS (in /Ground_Track) are in a float format and do not need a scale factor.

HDFEOS

HDFEOS contains the coordinates (lon, lat, time) of the projected pixels (folder: Geolocation Fields) and the external information (day night flag, observation and solar position in folder, DEM altitude and corrected DEM latitude and longitude : Data Fields). These datasets can be found in the folder /HDFEOS/SWATH/VII_SWATH_Type_L1B/

Dataset name	Description and units	Dimension
Latitude	Latitude of the pixel in degrees (non DEM corrected)	2-D (3800x3264)[(1)] array
Longitude	Longitude of the pixel in degrees (non DEM corrected)	2-D (3800x3264)[(1)] array
TAI_Time	International Atomic Time in s of the pixel observation (since the 1st January 1993 0:00 UTC)	2-D (3800x3264)[(1)] array

Table 2.4: List and description of geolocation fields and descriptor datasets

Dataset name	Description and units	Dimension
DEM Height [(1)]	Altitude of the pixel in m, from the DEM ACE2 dataset	2-D (3800x3264)[(1)] vector
Day_Night_Flag	Flag (0 = Day, 1 = Night) describing the day/night situation of the pixel at the observation time (no unit)	2-D (3800x3264)[(1)] vector
Latitude_DEM_corrected	Latitude corrected for DEM elevation	2-D (3800x3264)[(1)] vector
Longitude_DEM_corrected	Longitude corrected for DEM elevation	2-D (3800x3264)[(1)] vector
Scattering_Angle	Scattering Angle in degrees	2-D (3800x3264)[(1)] vector
Sensor_Azimuth	Observation azimuth angle of the pixel by the sensor (in degrees)	2-D (3800x3264)[(1)] vector
Sensor_Zenith	Observation zenith angle of the pixel by the sensor (in degrees)	2-D (3800x3264)[(1)] vector
Solar_Azimuth	Solar azimuth angle in the pixel at the observation time (in degrees)	2-D (3800x3264)[(1)] vector
Solar_Zenith	Solar zenith angle in the pixel at the observation time (in degrees)	2-D (3800x3264)[(1)] vector

Table 2.5: List and description of associated data fields datasets

(1) 3800= 38*100; 38 = number of along-track pixels of a sequence, 100 is the number of sequences in a 5 mn (284 s) segment. 3264 is the number of across-track pixels.

HDFEOS INFORMATION

This folder contains the dataset StructMetadata.0 containing metadata relative to the processing of the hdf files.

2.2.2 INSTRUMENT 3MI

2.2.2.1 Naming convention for the hdf file

The files' name convention is similar to VII's one :
EPS-SG_3MI_GEOLOC_AAAA-MM-DDTHH-mm-ss**_V**p.p**.he5**
with AAAA-MM-DDTHH-mm-ss, the instant of the beginning of the segment, namely: AAAA= the number of the year (4 digits) / MM = the number of the month (2 digits) / DD = the number of the day (2 digits) / HH = the number of the hour (2 digits) / mm = the number of the minute (2digits) / p.p = dataset revision number.
Example: ***EPS-SG_3MI_GEOLOC_2007-09-12T08-43-03_V1.4.he5*** *is the hdf file for 3MI, for the orbit's segment of the 12th of September 2007, starting at 8H43mn (UTC), first version of processing and without DEM correction.*

2.2.2.2 Dataset folders

Ground_Track

The folder /Ground_Track in the hdf files contains information about the satellite position: Satellite altitude (SC_Altitude), Satellite Attitude (SC_Attitude) given as roll, pitch and yaw Euler angles, satellite nadir projection on the Earth's ellipsoid (SSP_Longitude, SSP_Latitude), the time associated to the satellite position (SSP_TAI_TIME), projection of the satellite speed vector (N, E, Doppler velocity) on the Earth's ellipsoid (SSP_Velocity_NE_components).

Dataset name	Description and units	Dimension
SC_Altitude	Altitude of the satellite in m	1-D (2Tseg) vector Tseg = time of the segment in s
SC_Attitude	Attitude of the platform provided as roll, pitch and yaw angles expressed in Orbital reference frame.	2-D (2Tseg x3) vector
SSP_Latitude	Geodetic Latitude of the satellite in degrees (positive North)	1-D (2Tseg) vector
SSP_Longitude	Geodetic Longitude of the satellite in degrees (positive East)	1-D (2Tseg) vector
SSP_TAI_Time	International Atomic Time in s (since the 1st January 1993 0:00 UTC)	1-D (2Tseg) vector
SSP_Velocity_NE_components	Vector speed in m/s (East,North, Doppler) of the trajectory of the projection of the satellite on the Earth's Ellipsoid	2-D (2Tseg x 3) vector

Table 2.6: List and description of orbit track descriptor datasets

These SDS (in /Ground_Track) are in a double format and do not need to be scaled.

HDFEOS

HDFEOS contains the coordinates (longitude, latitude, time) of the projected pixels (folder: Geolocation Fields) and the external information (DEM Height, day night flag, DEM corrected Latitude and Longitude, observation and solar position in folder: Data Fields). These datasets can be found in the folders :
/HDFEOS/SWATH/3MI_VIS_SWATH_Type_L1B (for the visible channels) and in
/HDFEOS/SWATH/3MI_SWIR_SWATH_Type_L1B (for the shortwave infrared channels).

Dataset name	Description and units	Dimension
Latitude	Latitude of the pixel in degrees (non DEM corrected)	4-D (14x9x512x512)[(1)] vector
Longitude	Longitude of the pixel in degrees (non DEM corrected)	4-D (14x9x512x512)[(1)] vector
TAI_Time	International Atomic Time in s of the pixel observation (since the 1st January 1993 0:00 UTC)	4-D (14x9x512x512)[(1)] vector

Table 2.7: List and description of geolocation fields and descriptor datasets for the VNIR channels

[(1)] 14 = number of granules of a sequence in a 5 min (308 s) segment; 9 = number of channels for 3MI-VIS; 512 = along-track pixels of a granule, 512 is the number of across-track pixels.

Dataset name	Description and units	Dimension
Latitude	Latitude of the pixel in degrees (non DEM corrected)	4-D (28x4x256x500)[(1)] vector
Longitude	Longitude of the pixel in degrees (non DEM corrected)	4-D (28x4x256x500)[(1)] vector
TAI_Time	International Atomic Time in s of the pixel observation (since the 1st January 1993 0:00 UTC)	4-D (28x4x256x500)[(1)] vector

Table 2.8: List and description of geolocation fields and descriptor datasets for the SWIR channels

[(1)] 28 = number of SWIR acquisition for a given channel in a 5 min (308 s) segment; 4 = number of channels for 3MI-SWIR; 256 = along-track pixels of a granule, 500 is the number of across-track pixels.

Dataset name	Description and units	Dimension
DEM Height	Altitude of the pixel in m, from the DEM ACE2 dataset	4-D (14x9x512x512)[(1)] vector
Day_Night_Flag	Flag (0 = Day, 1 = Night) describing the day/night situation of the pixel at the observation time (no unit)	4-D (14x9x512x512)[(1)] vector
Latitude_DEM_corrected	Latitude corrected for DEM elevation	
Longitude_DEM_corrected	Longitude corrected for DEM elevation	
Scattering_Angle	Scattering Angle in degrees	2-D (14x9x512x512)[(1)] vector
Sensor_Azimuth	Observation azimuth angle of the pixel by the sensor (in degrees)	4-D (14x9x512x512)[(1)] vector
Sensor_Zenith	Observation zenith angle of the pixel by the sensor (in degrees)	4-D (14x9x512x512)[(1)] vector
Solar_Azimuth	Solar azimuth angle in the pixel at the observation time (in degrees)	4-D (14x9x512x512)[(1)] vector
Solar_Zenith	Solar zenith angle in the pixel at the observation time (in degrees)	4-D (14x9x512x512)[(1)] vector

Table 2.9: List and description of ancillary parameters datasets for VNIR channels

[(1)] 14 = number of acquisition for a given spectral channel in a 5 mn (308 s) segment; 9 = number of channels for 3MI-VIS; 512 = along-track pixels of a granule, 512 is the number of across-track pixels.

Dataset name	Description and units	Dimension
DEM Height	Altitude of the pixel in m, from the DEM ACE2 dataset	4-D (28x4x256x500) [(1)] vector
Day_Night_Flag	Flag (0 = Day, 1 = Night) describing the day/night situation of the pixel at the observation time (no unit)	4-D (28x4x256x500) [(1)] vector
Latitude_DEM_corrected	Latitude corrected for DEM elevation	4-D (28x4x256x500) [(1)] vector
Longitude_DEM_corrected	Longitude corrected for DEM elevation	4-D (28x4x256x500) [(1)] vector
Scattering_Angle	Scattering Angle in degrees	2-D (28x4x256x500) [(1)] vector
Sensor_Azimuth	Observation azimuth angle of the pixel by the sensor (in degrees)	4-D (28x4x256x500) [(1)] vector
Sensor_Zenith	Observation zenith angle of the pixel by the sensor (in degrees)	4-D (28x4x256x500) [(1)] vector
Solar_Azimuth	Solar azimuth angle in the pixel at the observation time (in degrees)	4-D (28x4x256x500) [(1)] vector
Solar_Zenith	Solar zenith angle in the pixel at the observation time (in degrees)	4-D (28x4x256x500) [(1)] vector

Table 2.10: List and description of ancillary parameters datasets for SWIR channels

[(1)] 28 = total number of SWIR acquisition in a 5 mn (308 s) segment; 4 = number of channels for 3MI-SWIR; 256 = along-track pixels of array

HDFEOS INFORMATION

This folder contains the dataset StructMetadata.0 containing metadata relative to the processing of the hdf files.

2.3 Illustration of simulated datasets

In Table 2.11, we link the number of the figures corresponding to the datasets of the hdf files.

SC_Attitude	See example Figure 2.6 page 23
SSP_Latitude	On every figure (blue, red or black line at the middle of the scanned area)
SSP_Longitude	On every figure (blue, red or black line at the middle of the scanned area)
SSP_TAI_Time	Not represented
SSP_Velocity_NE_components	Not represented
Altitude	For VII: Figures 2.17, 2.18; for 3MI- Figures 2.37, 2.38, 2.39, and, 2.40
Latitude, longitude	Figures 2.9, 2.10, 2.11, 2.12 for VII, 2.21, 2.22, 2.23, 2.24, 2.25, 2.26 for 3MI
TAI_Time	Not represented
Day_Night_Flag	Not represented
Solar_Azimuth (SAA)	For VII: Figure 2.14, for 3MI-VIS: Figure 2.28, for 3MI-SWIR: Figure 2.30
Solar_Zenith (SZA)	For VII: Figure 2.13, for 3MI-VIS: Figure 2.27, for 3MI-SWIR: Figure 2.29
Sensor_Azimuth (OAA)	For VII: Figure 2.16, for 3MI-VIS: Figure 2.32, for 3MI-SWIR: Figure 2.35
Sensor_Zenith (OZA)	For VII: Figure 2.15, for 3MI-VIS and 3MI-SWIR : Figures 2.32, 2.35

Table2.11: References to figures illustrating datasets available in hdf files.

2.3.1 Figures for METImage (VII)

2.3.1.1 METImage - Sampling geometries

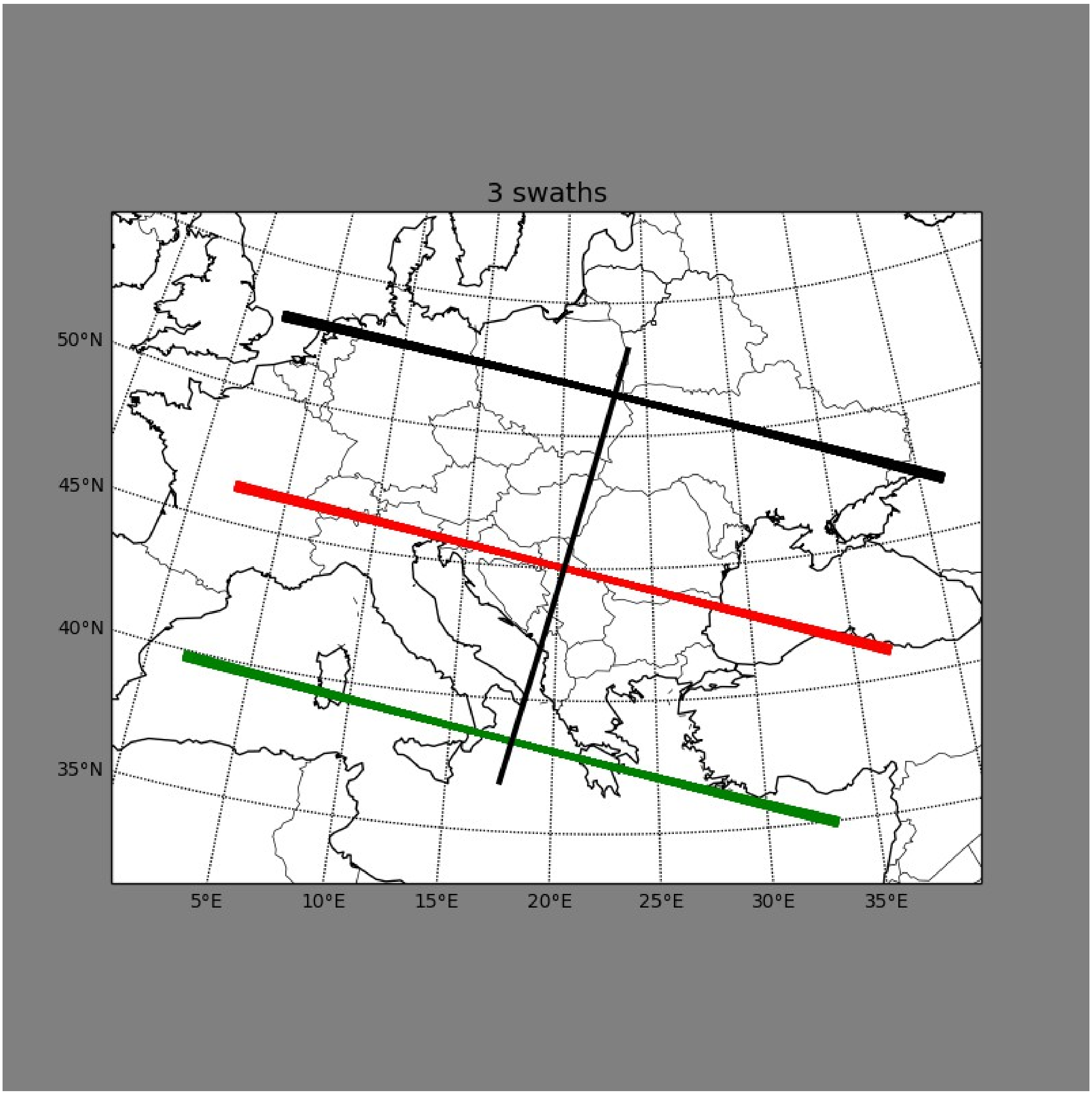

Figure 2.9: Illustration of ground samples observed for 3 scans (non consecutive in time) corresponding to scan 1, 50 and 100 of the 5 minutes sample granule. Bow-tie feature of the individual scan is clearly observed with scan footprint on Earth increasing with view angle.

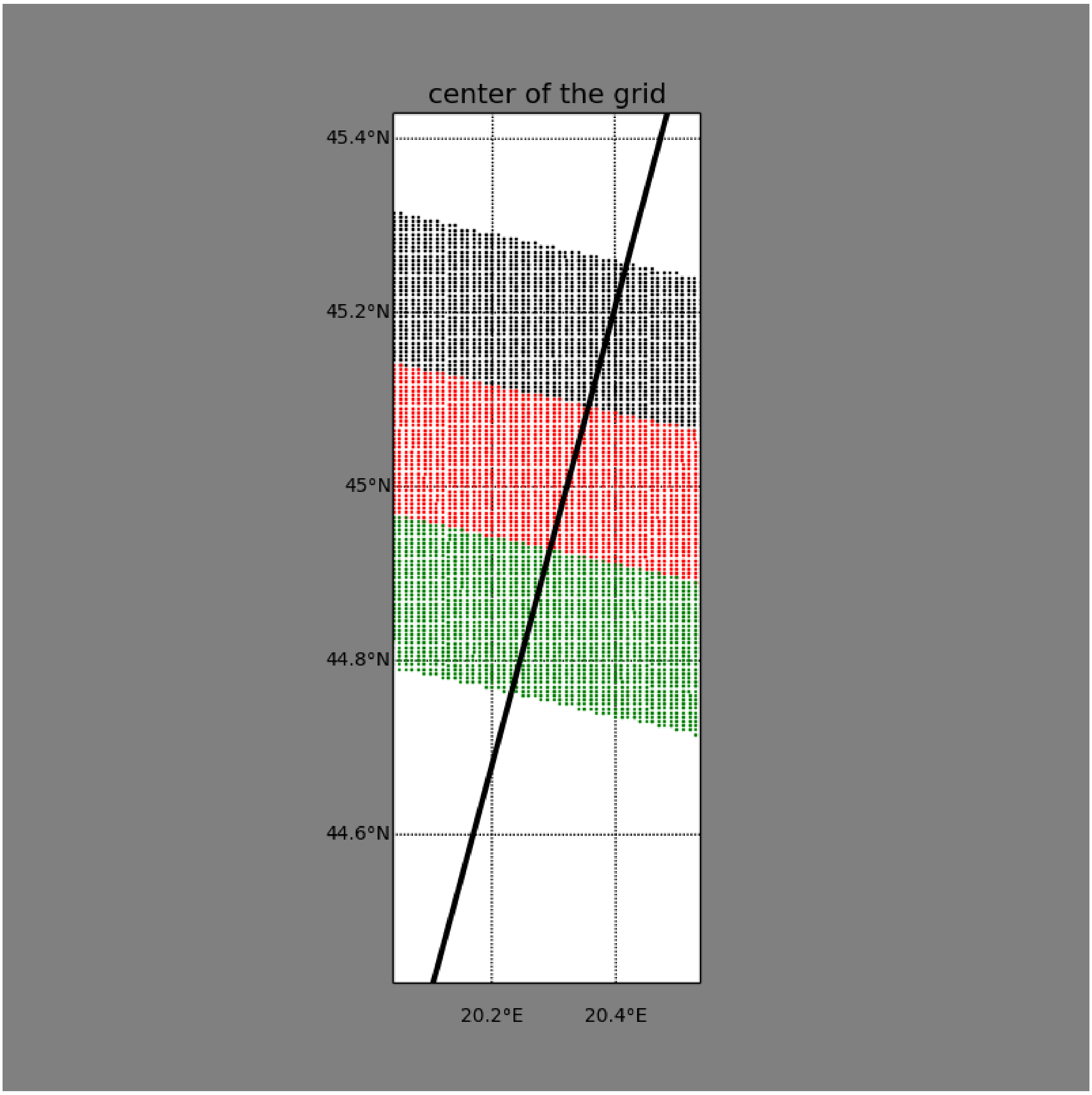

Figure 2.10: Central position of individual samples from 3 consecutive scans observed at nadir. With the new simulation parameters (2.843s scan period, 500 m ground pixel and provided TLE) continuity of observation is obtained at nadir along track.

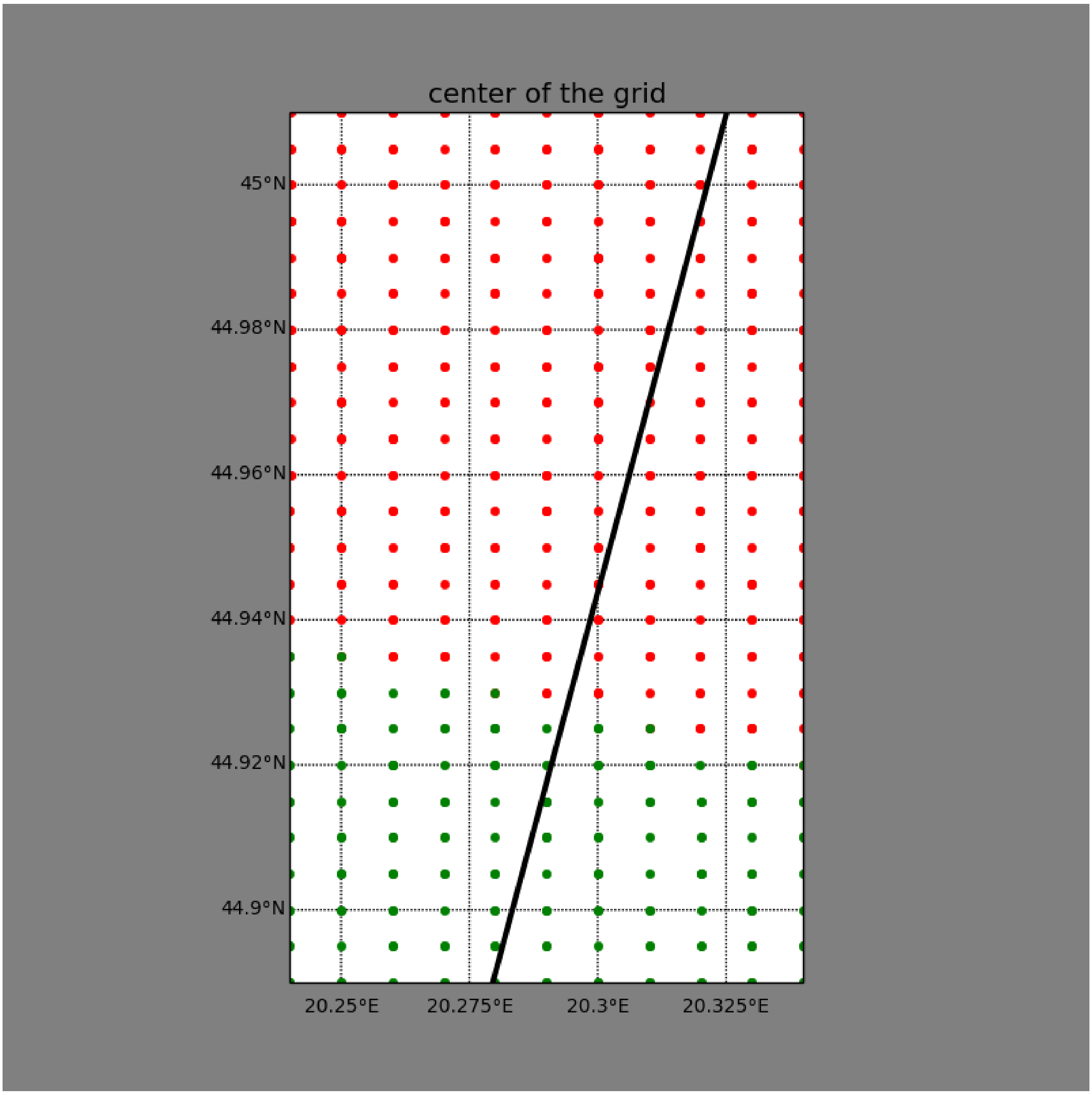

Figure 2.11: Zoom on the central position of individual samples from 2 consecutive scans observed at nadir. With the new simulation parameters (2.843s scan period, 500 m ground pixel and provided TLE) continuity of observation is obtained at nadir along track.

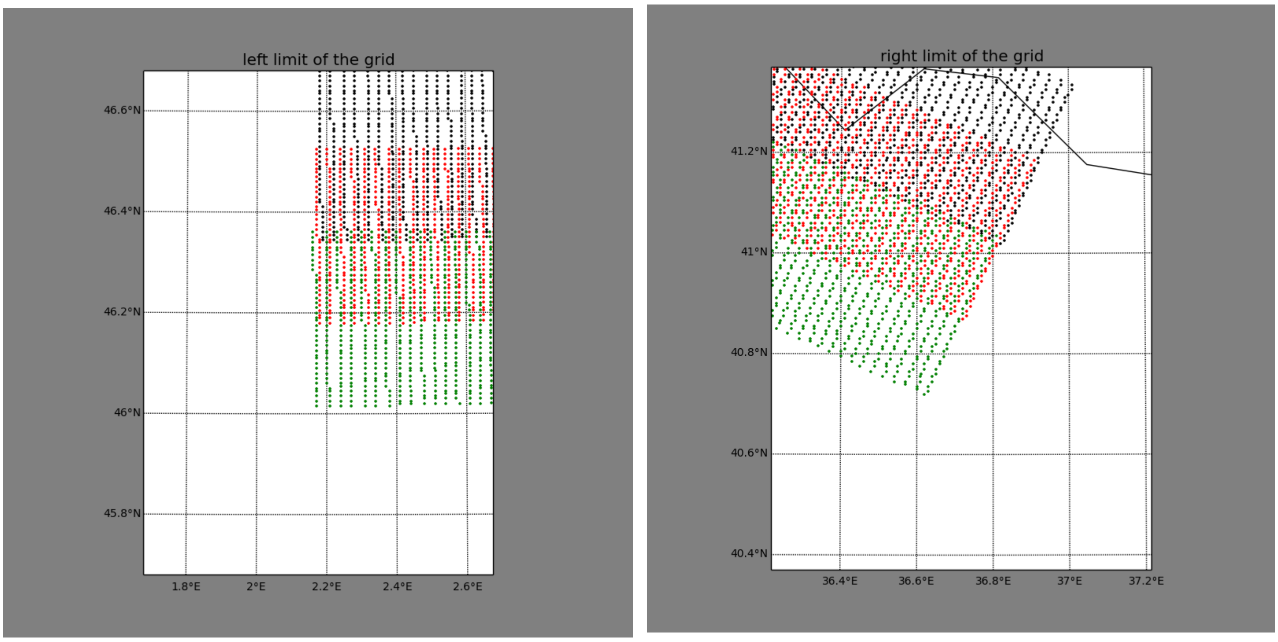

Figure 2.12: Overlapping scans on the West side (left) and East side (right) of swath.

2.3.2 METImage Sun Geometries

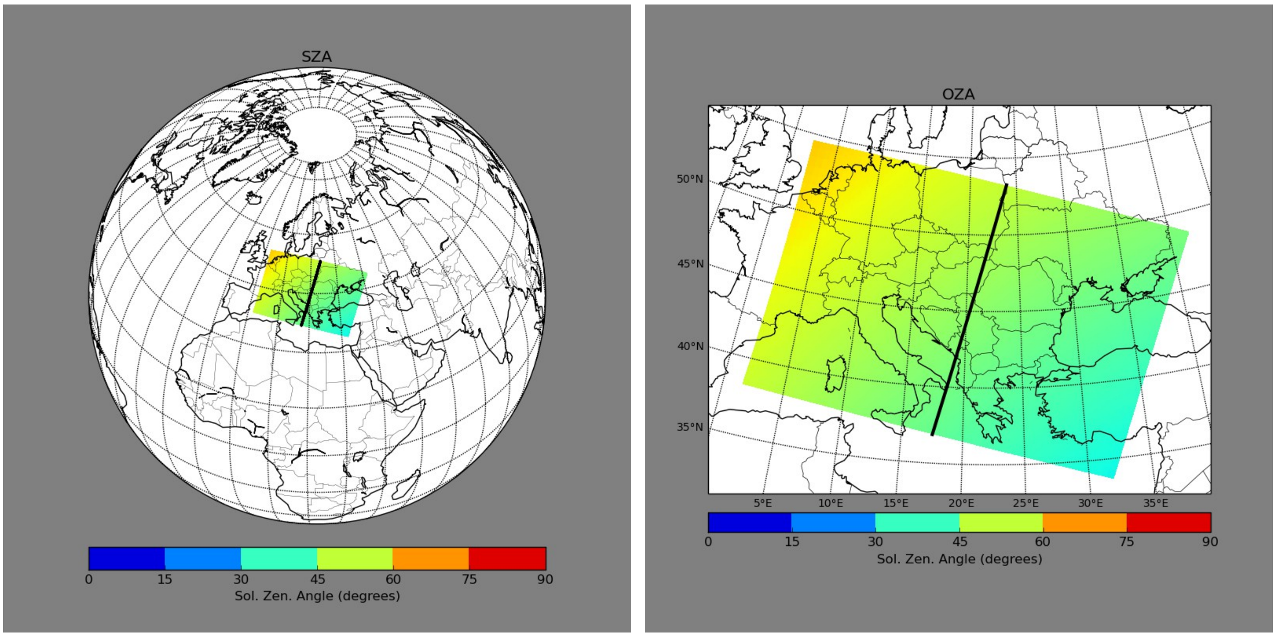

Figure 2.13: Sun Zenith Angle (SZA) for METImage sample observation

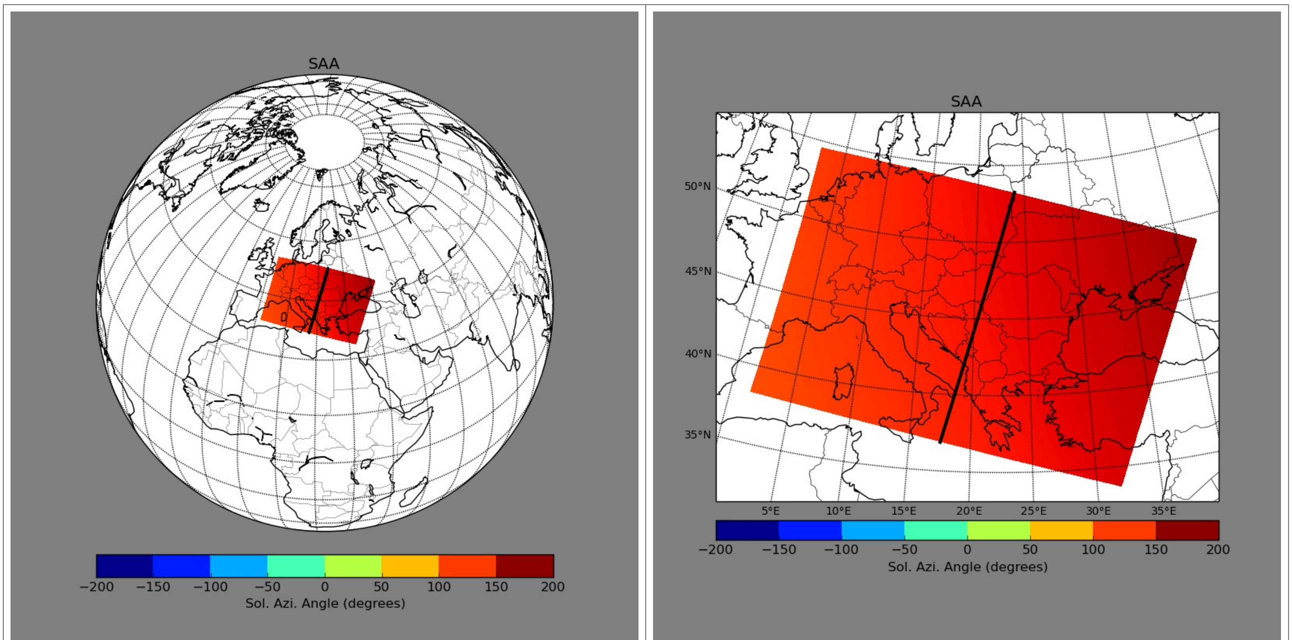

Figure 2.14: Sun Azimuth Angle (SAA) for METImage sample observation

2.3.3 METImage Sensor Geometries

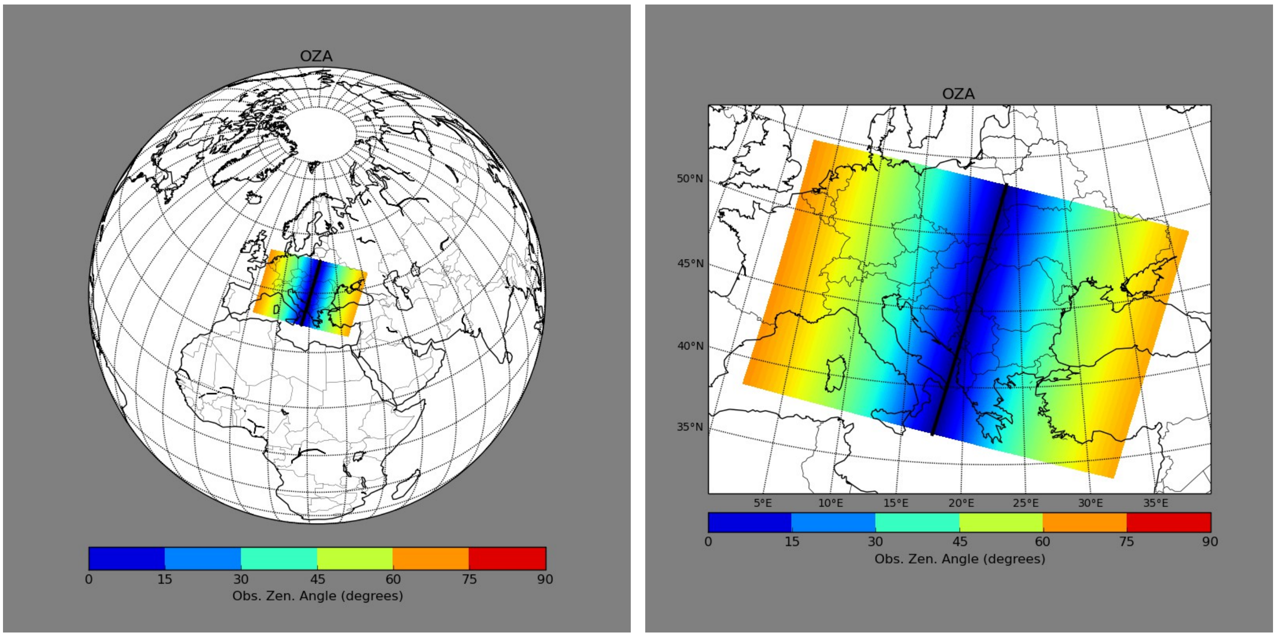

Figure 2.15: Observation (sensor viewing) Zenith Angle - OZA

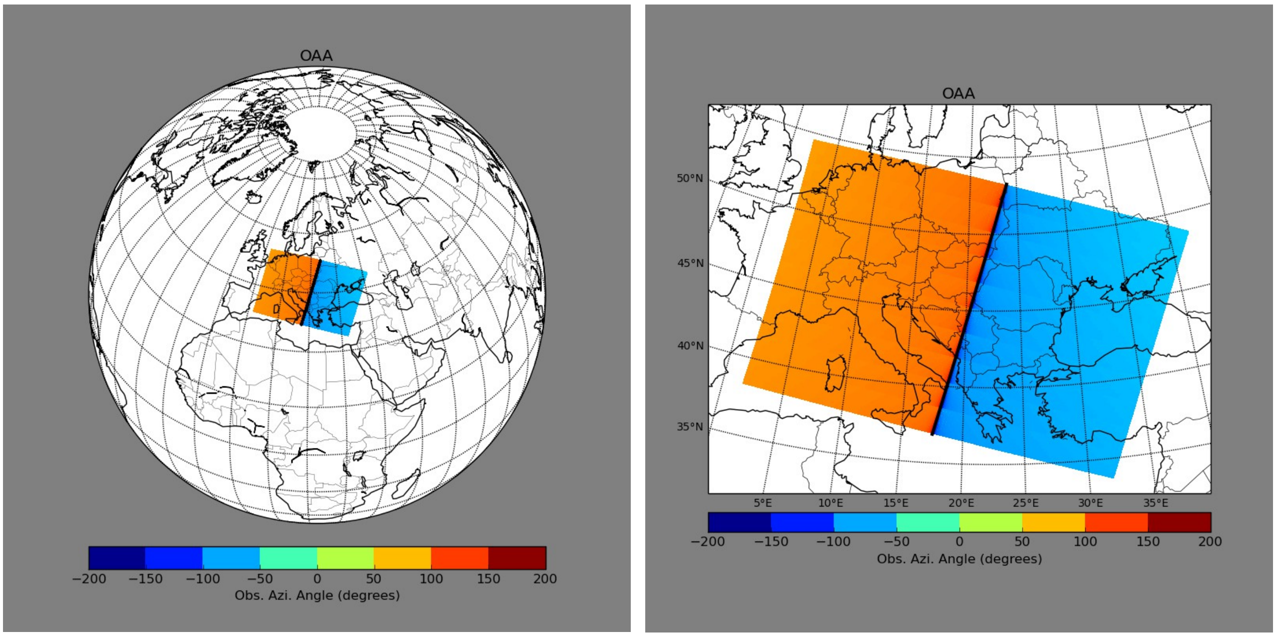

Figure 2.16: Observation (sensor viewing) Azimuth Angle - OAA

2.3.3.1 DEM correction for METImage:

ACE2 DEM over the scanned areas

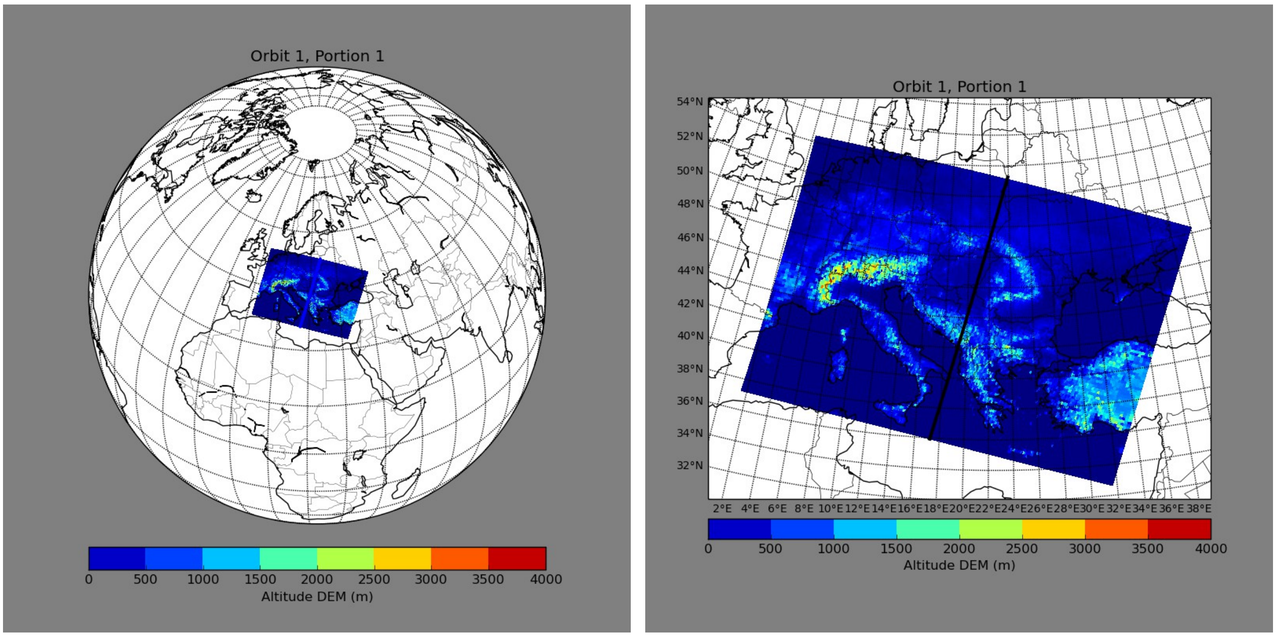

Figure 2.17: ACE2 DEM for the area scanned by METImage

Effects of the DEM-correction algorithm

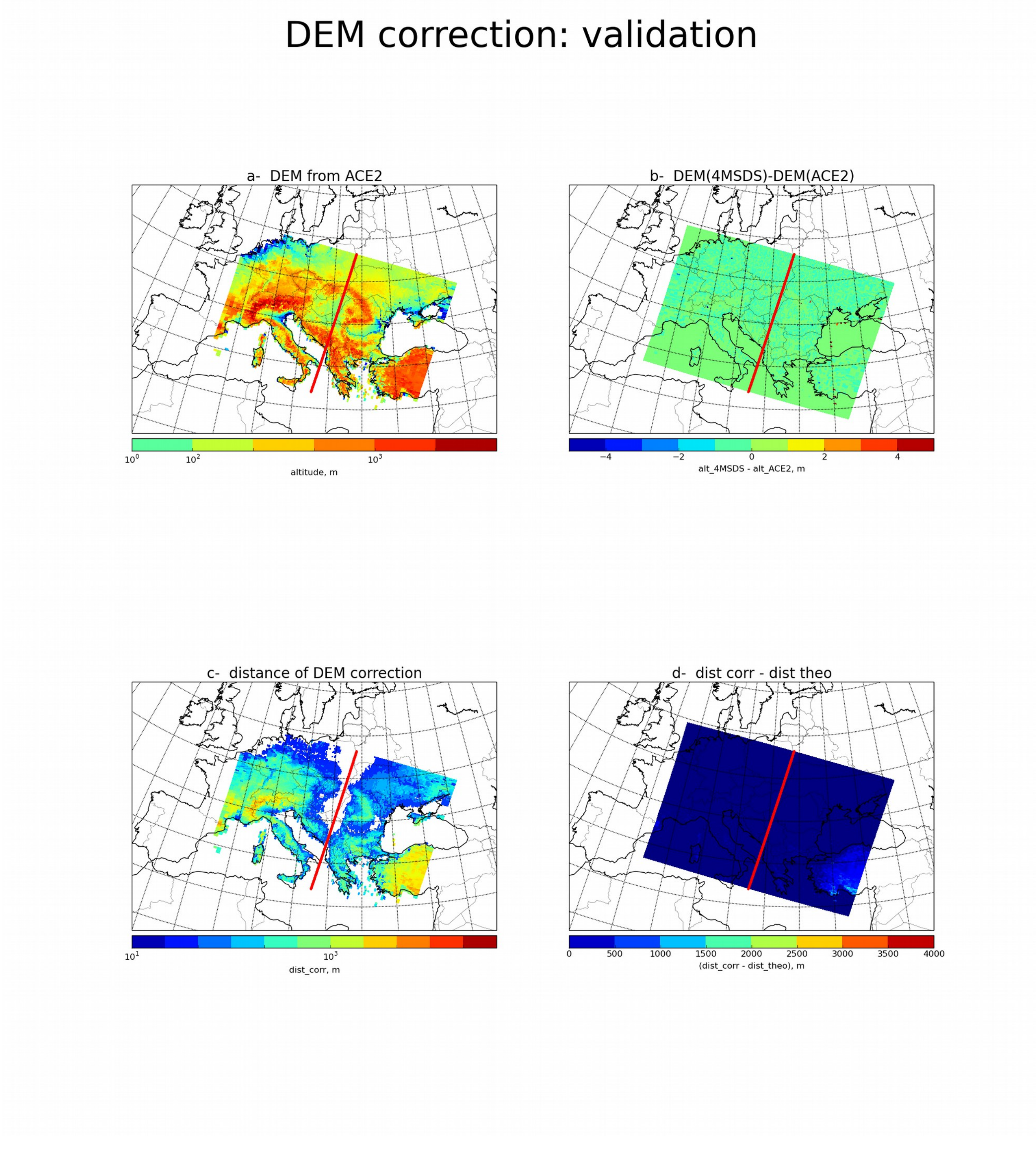

Figure 2.18: DEM correction: a) Altitude for the ACE-2 DEM in m, b) difference for each pixel between the altitude of the pixels of VII in 4MSDS project and the altitude delivered by ACE2, in m. c) Effect of the DEM correction: shift in m in direction of the track d) Difference in m between the shifted distance of the algorithm of DEM correction (dist_corr) and the theoretical distance of shift computed with the tangent method presented in Section 2.1.5. (dist_theo)

We zoom on the mountain chain of the Piz Bernina (Bordery Swiss-Italy, in the Alps, between the Lichtenstein and Milan), on the West side of the nadir track of the satellite, and we compare the centres of the pixels with and without DEM correction.

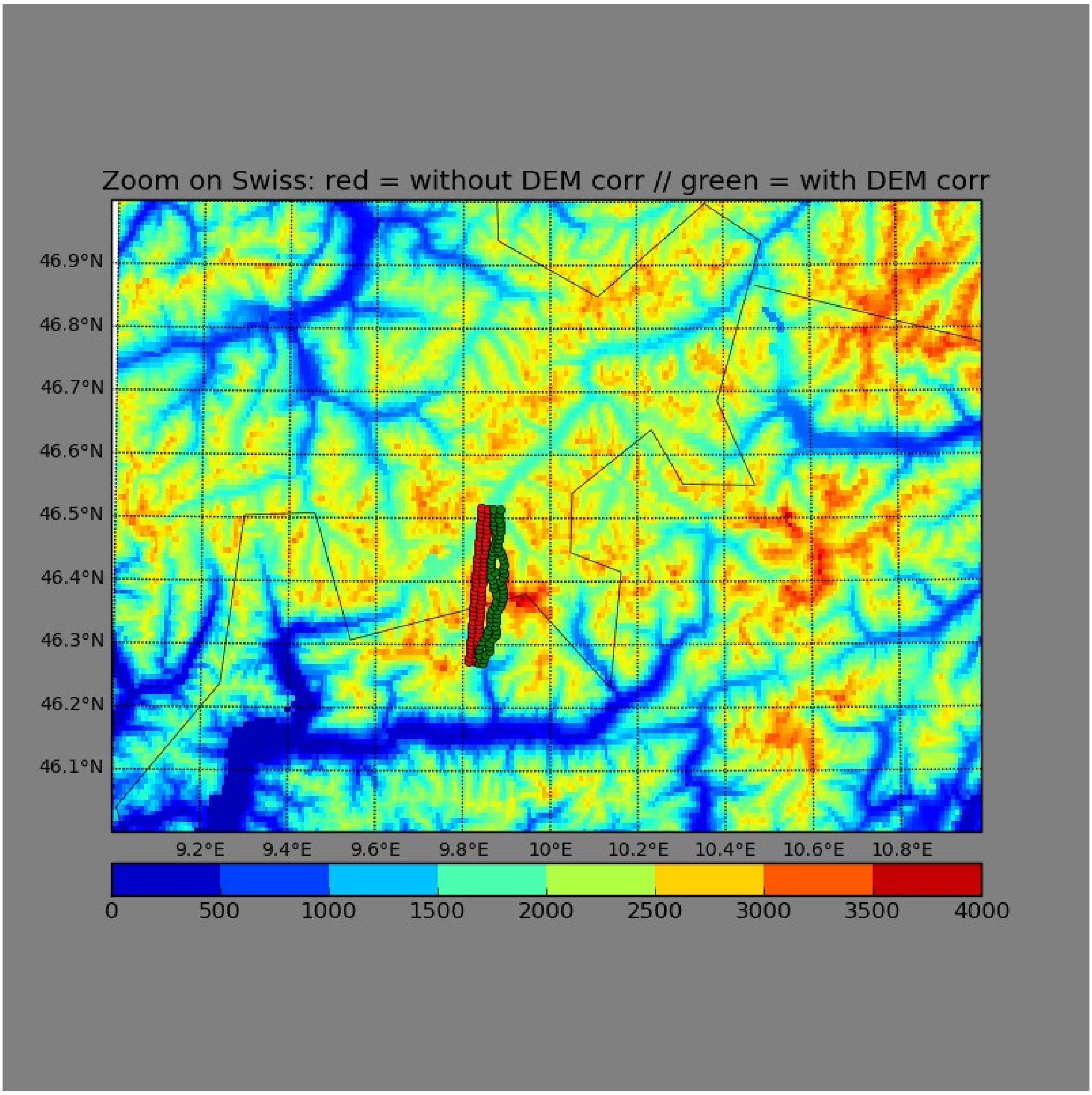

Figure 2.19: DEM correction (green) compared to pixels projected on the Earth Ellipsoid (red). The shift due to the DEM correction is in direction of the nadir track (East of the pixels). The higher are the mountains, the larger is the shift. The zoom is done on the mountain chain Piz Bernina (Bordery of Swiss and Italy, in the Alps, between Milan and the Lichtenstein).

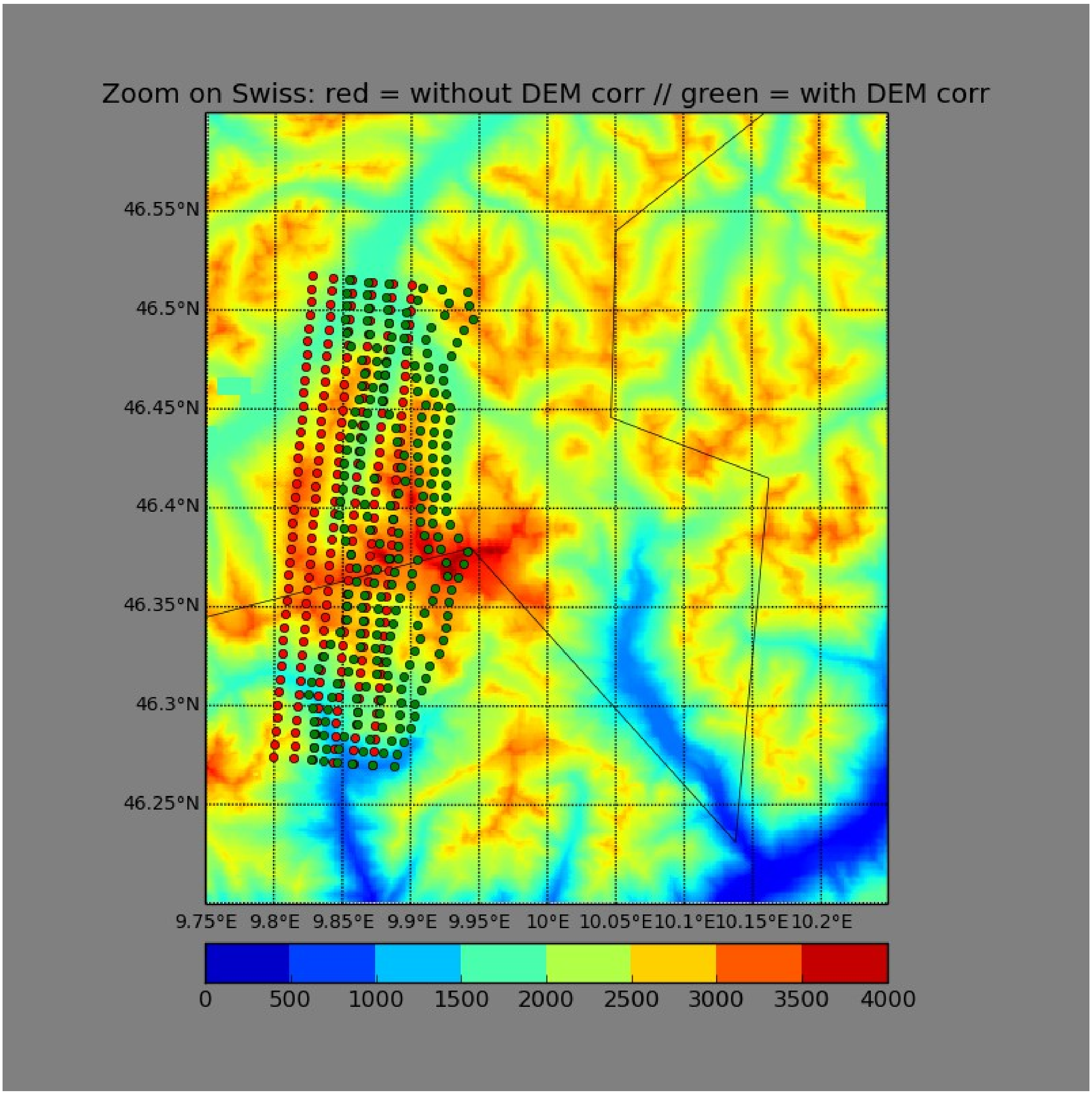

Figure 2.20: Same as Figure 2.19, with a larger zoom on the area. 5 series of pixels instead of 2 are shown.

2.3.4 Figures for 3MI

2.3.4.1 3MI Sampling geometries

We remind here that because of the different optical heads and focal plane assembly the viewing geometries and fields of view for VNIR and SWIR arrays will not be similar. In addition, a second SWIR acquisition is performed in addition to that synchronized with the VNIR one. This second SWIR acquisition will not be coincident either in time or space with any VNIR observations.

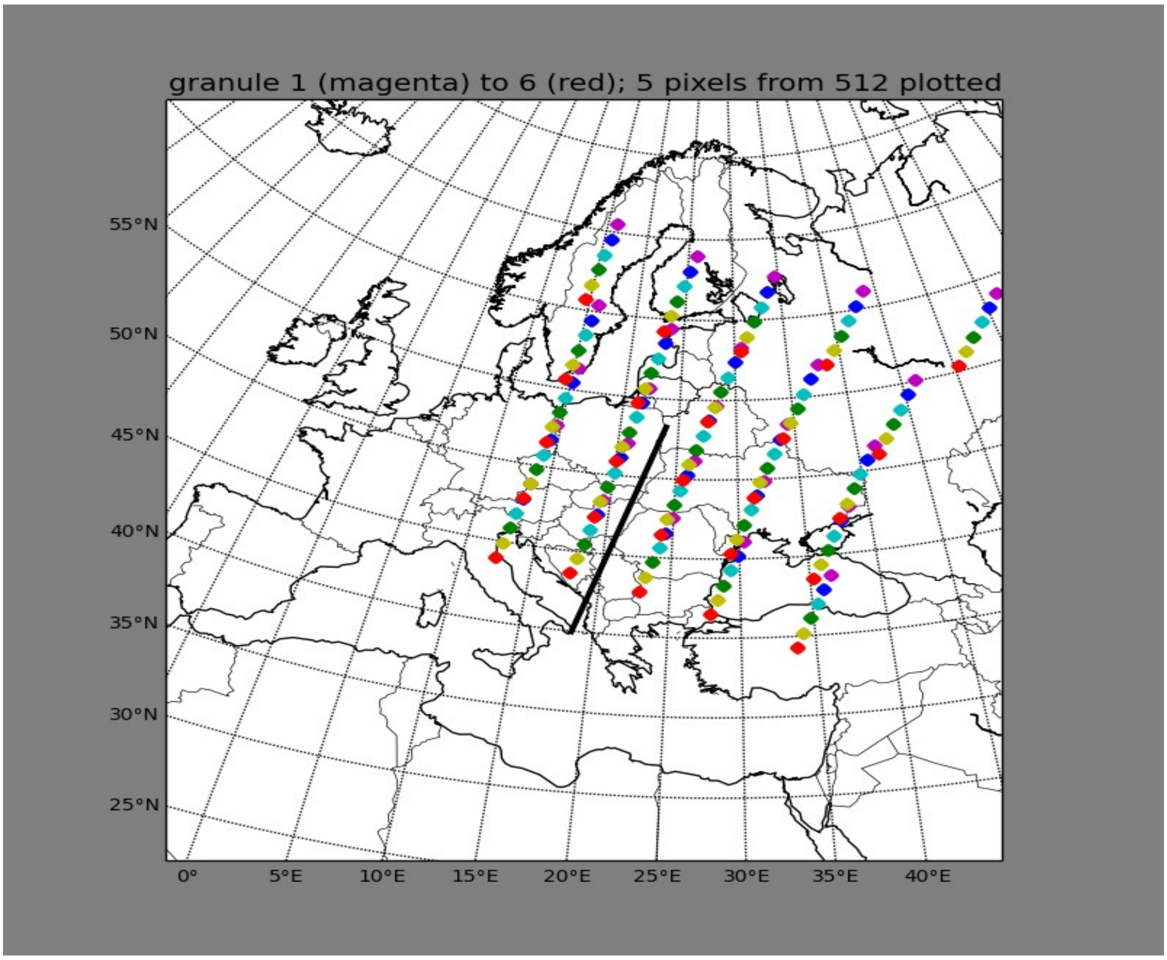
granule 1 (magenta) to 6 (red); 5 pixels from 512 plotted
55°N
50°N
45°N
40°N
35°N
30°N
25°N
0°
5°E
10°E
15°E
20°E
25°E
30°E
35°E
40°E

Figure 2.21 : *Position of ground samples for channel 1 (754 nm VIS) and for 6 consecutive sequences (different colours). Single frame ground samples have been sampled to show only 5 pixels cross-track and 5 pixels along-track for a given time stamps (i.e.: only 1% of the across/along pixels are shown). Note, that with current specification of 5.5 s wheel speed rotation period, about 14 viewing directions would be available for a given ground target- For 3MI-VIS channels*

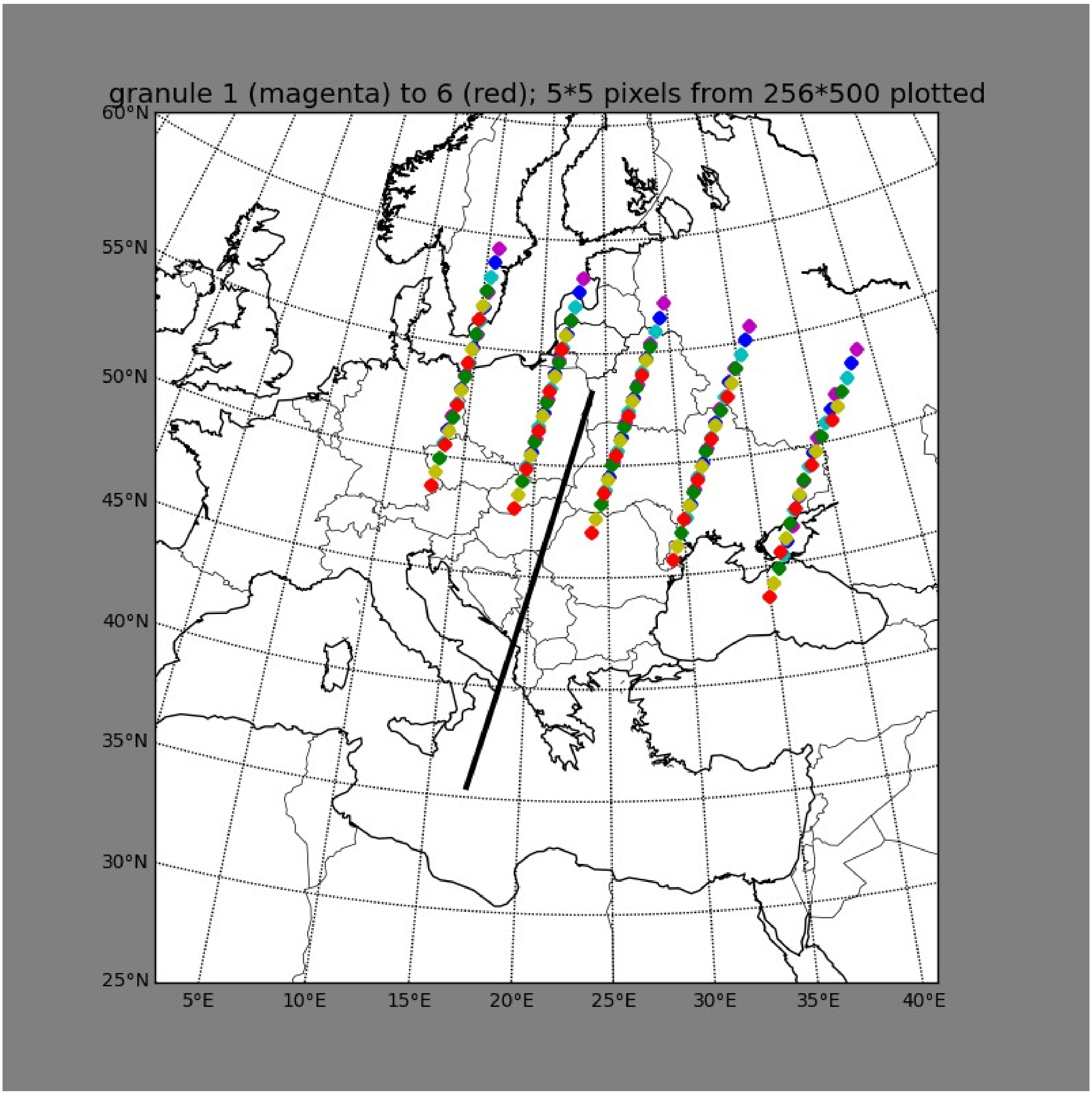

*Figure 2.22: Position of ground samples for channel 1 (910 nm SWIR) and for 6 consecutive sequences (different colours). Single frame ground samples have been sampled to show only 5 pixels cross-track and 5 pixels along-track for a given time stamps (i.e. : only 1%/2% of the across/along pixels are shown). Note, that with current specification of 5.5 s wheel speed rotation period, about 14 viewing directions would be available for a given ground target- **For 3MI-SWIR channels***

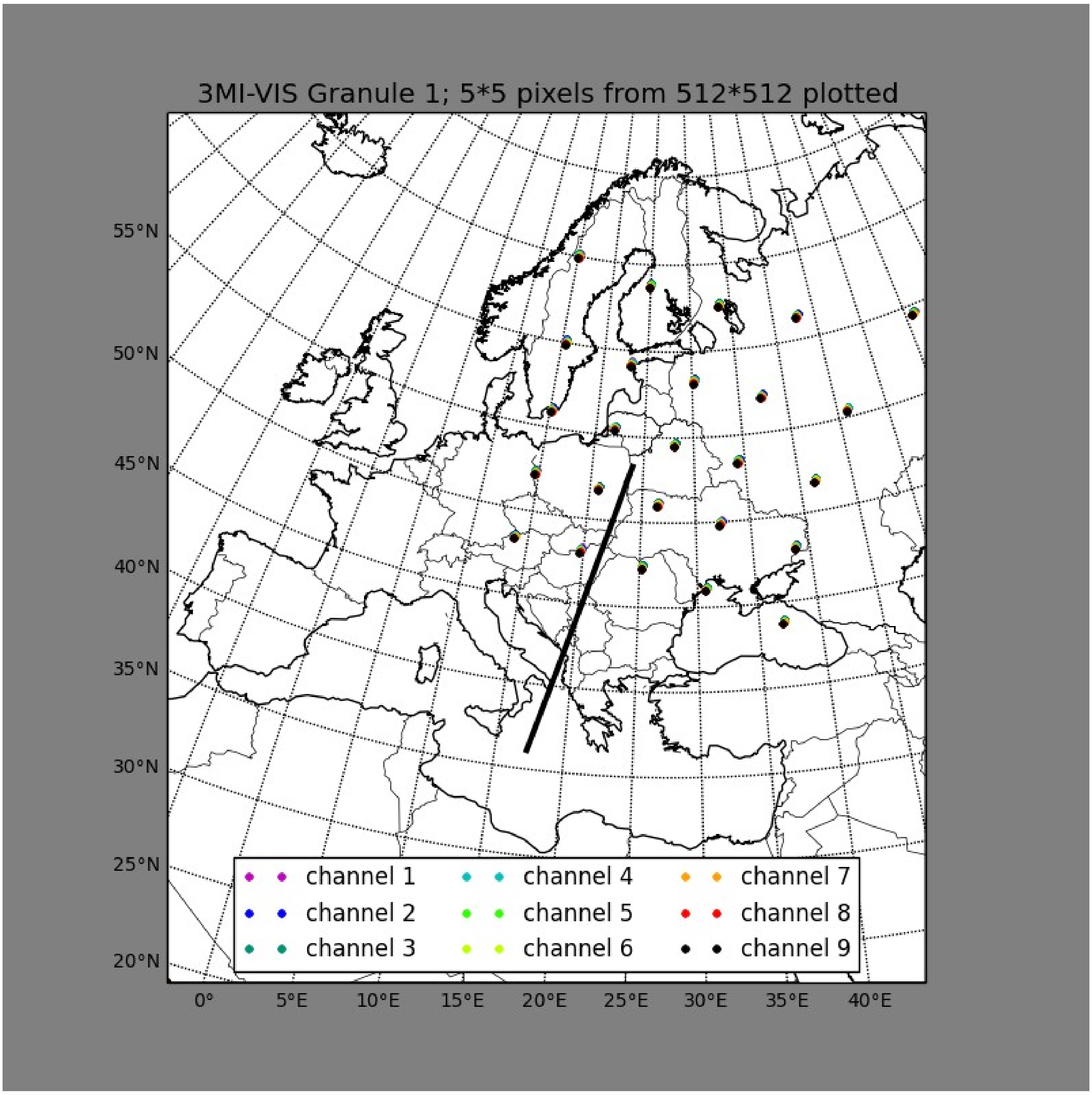

Figure 2.23: Position of ground samples for all 9 channels of VIS (different colours) for a single sequence. Single frame ground samples have been sampled to show only 5 pixels cross-track and 5 pixels along-track for a given time stamps (i.e. : only 1% of the across/along pixels are

*shown). - **For 3MI-VIS channels***

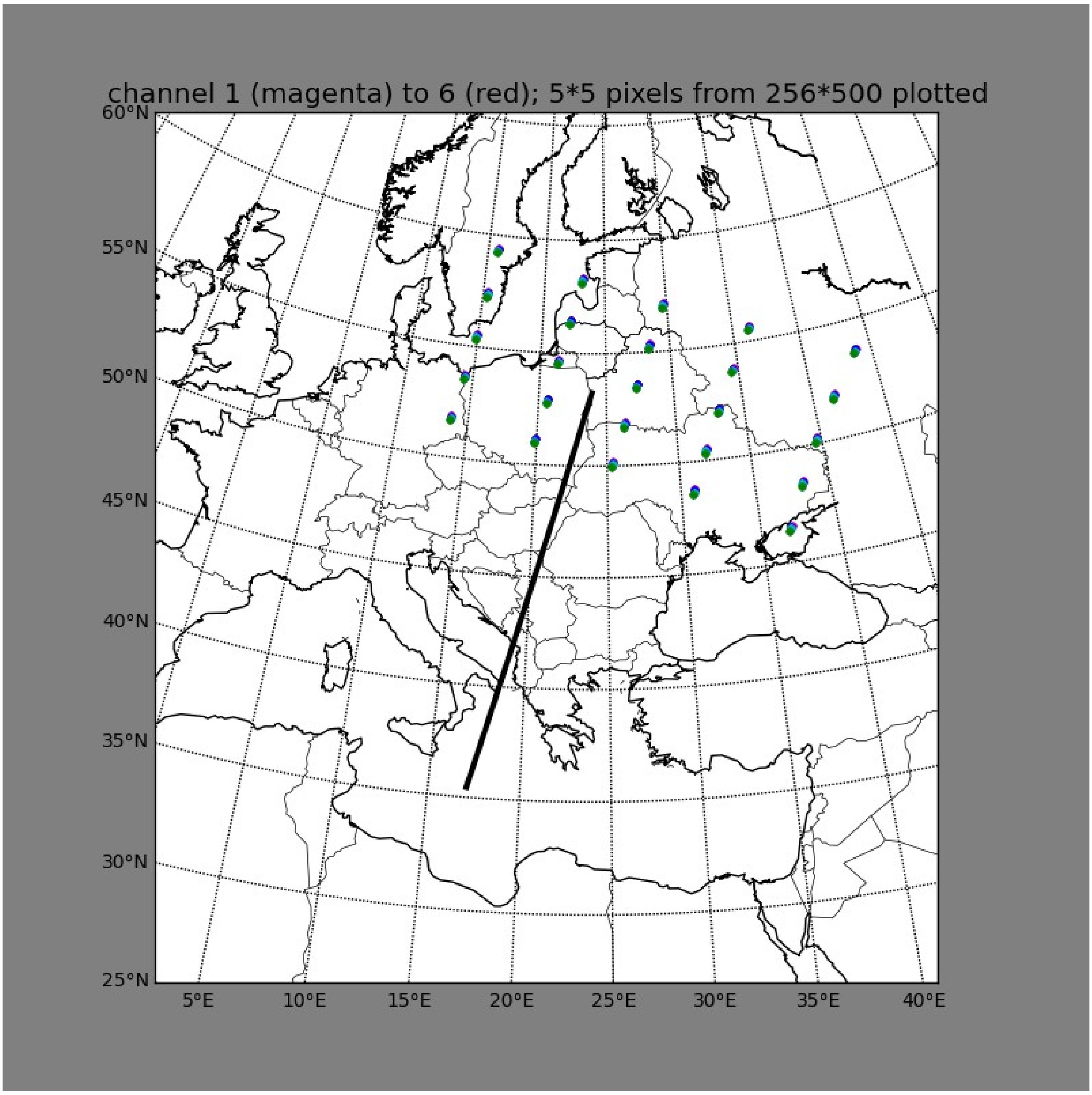

*Figure 2.24: Position of ground samples for channel 1 to 4 of SWIR (different colours) for a single sequence. Single frame ground samples have been sampled to show only 5 pixels cross-track and 5 pixels along-track for a given time stamps (i.e. : only 1%/2% of the across/along pixels are shown). - **For 3MI-SWIR channels***

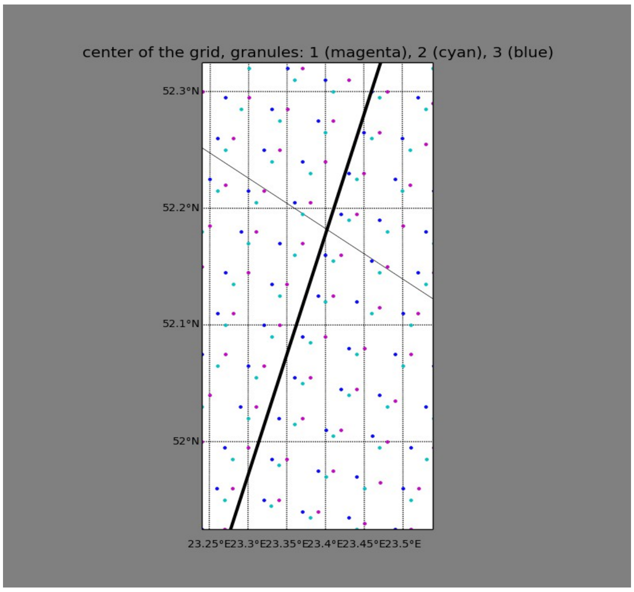

*Figure 2.25: Same as Figure 14 for 3 consecutive sequences (granules) only and zoomed around the sub-satellite ground track.- **For VIS-1 channel**.*

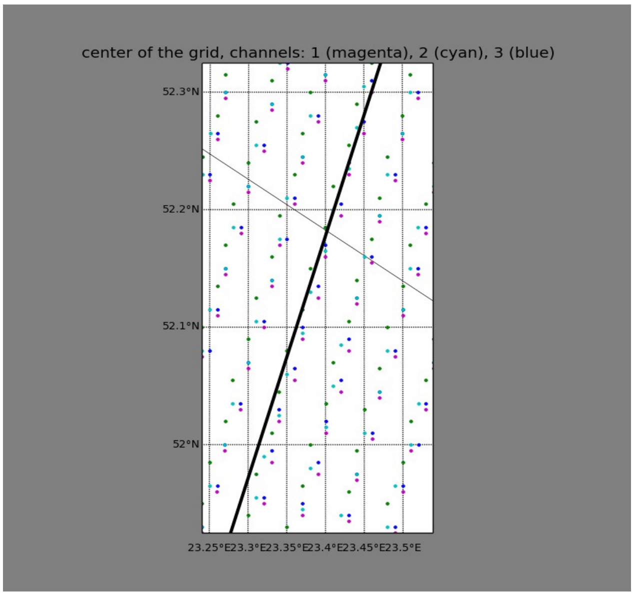

*Figure 2.26: Same as Figure 15 for 3 consecutive channels only and zoomed around the sub-satellite ground track.- **For VIS channels**.*

2.3.4.2 3MI Sun Geometries

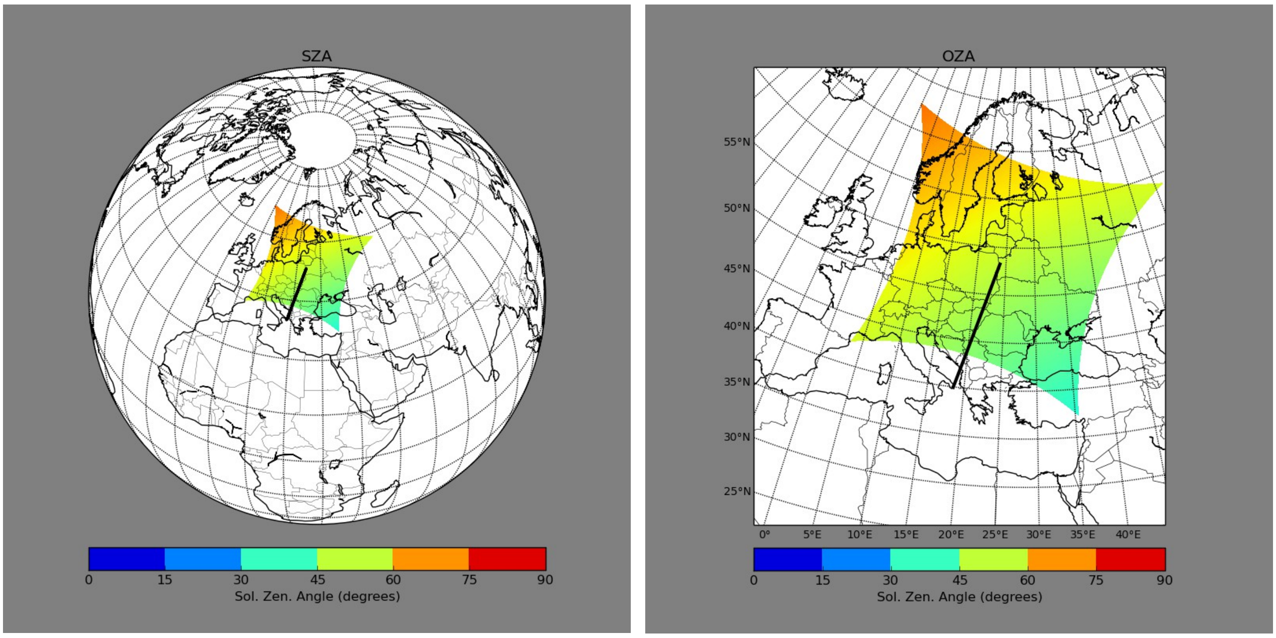

Figure 2.27 : Sun Zenith Angle (SZA) for 3MI spectral VNIR (VIS) channel 1

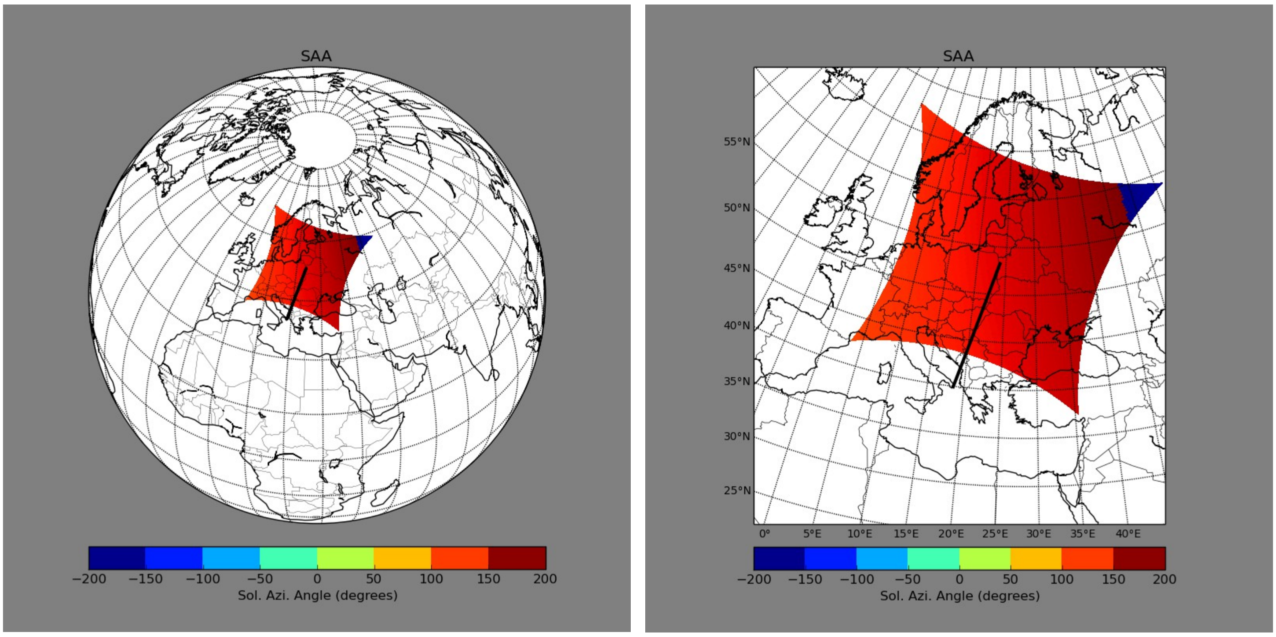

Figure 2.28: Sun Azimuth Angle (SAA) for 3MI spectral VNIR (VIS) channel 1

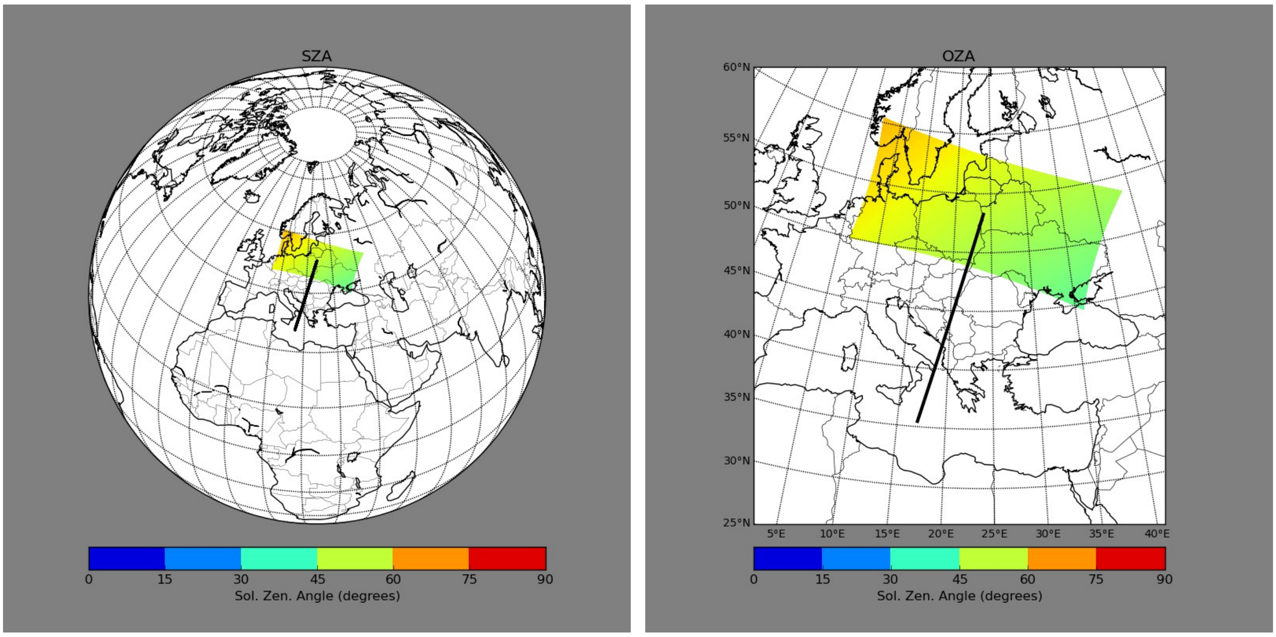

Figure 2.29 : Sun Zenith Angle (SZA) for 3MI spectral SWIR channel 1

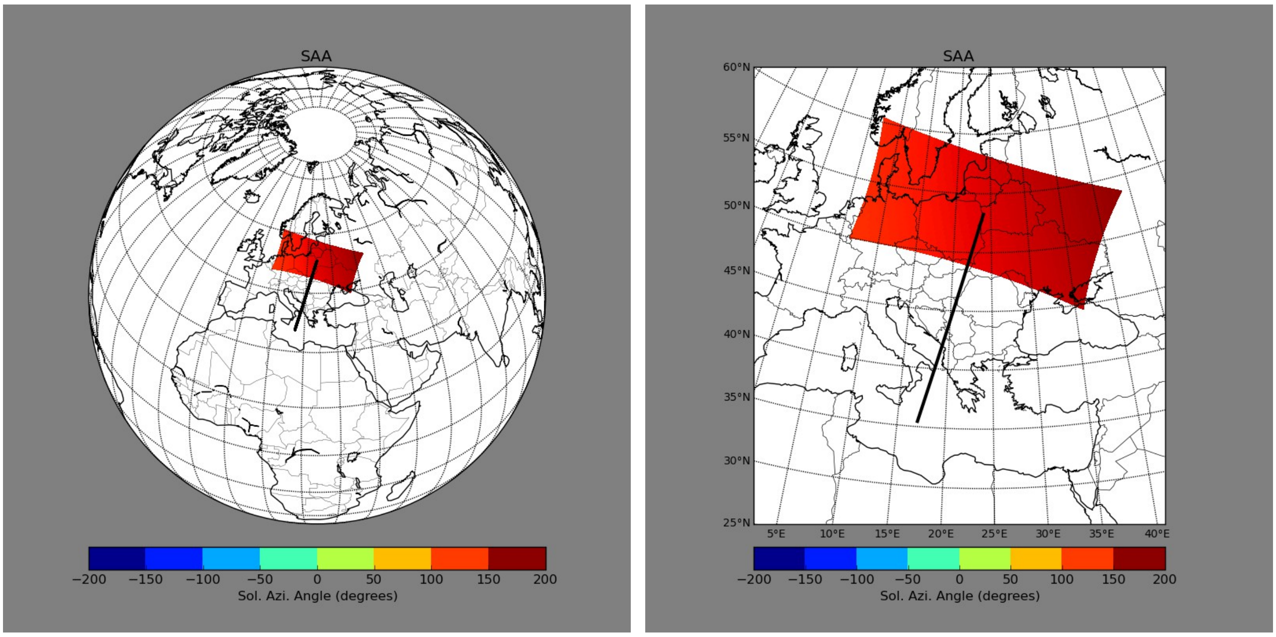

Figure 2.30 : Sun Azimuth Angle (SAA) for 3MI spectral SWIR channel 1

2.3.4.3 3MI Sensor Geometries

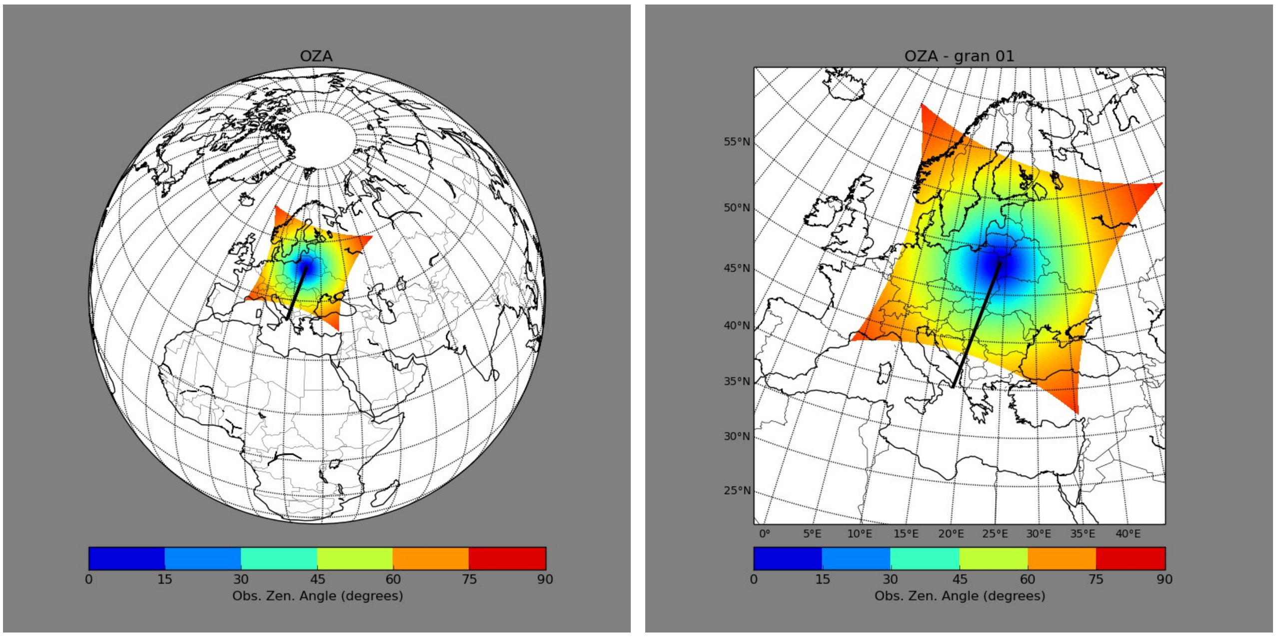

Figure 2.31: Observation (sensor viewing) Zenith Angle - OZA for 3MI spectral VNIR channel 1

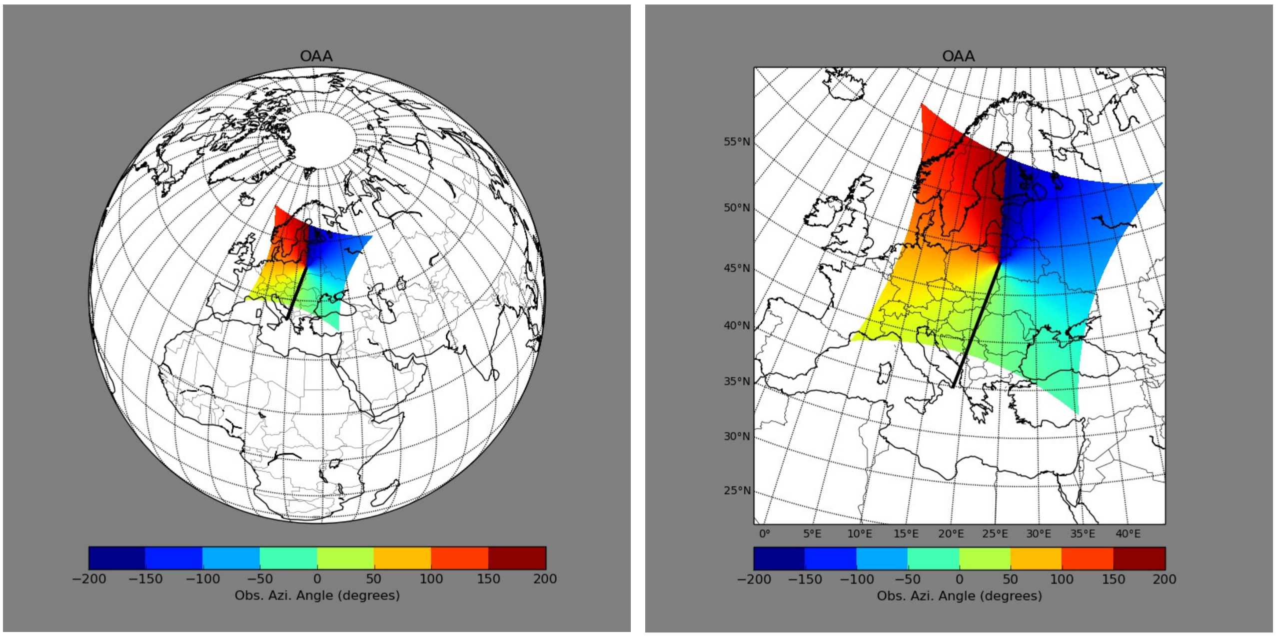

Figure 2.32 : Observation (sensor) Azimuth Angle – OAA for 3MI spectral VNIR channel 1

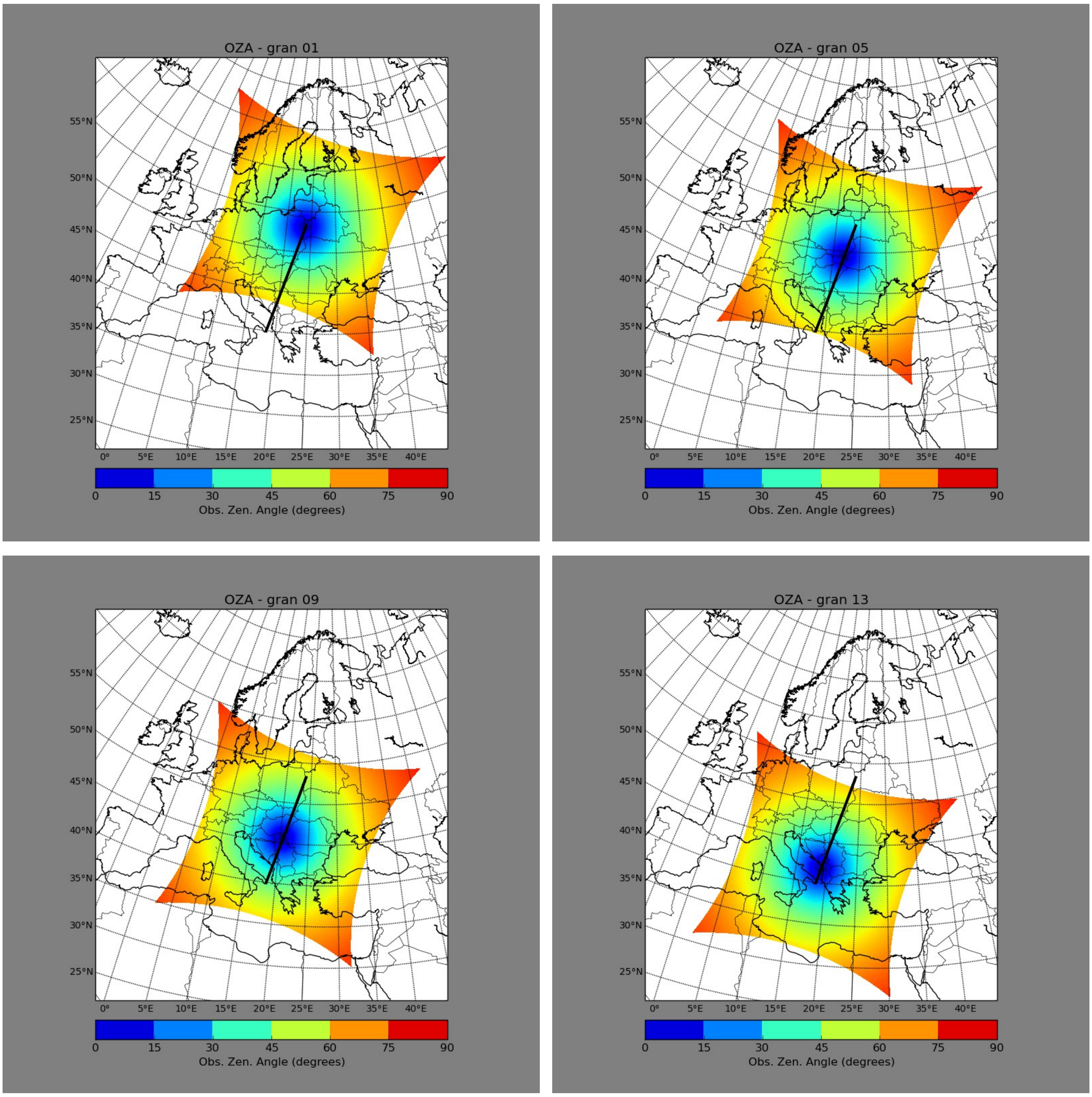

Figure 2.33 : Evolution of the observed scene - granule 1 (upper left), 5 (upper right), 9 (lower left) and 13 (lower right) - for the OZA of 3MI-VIS-1

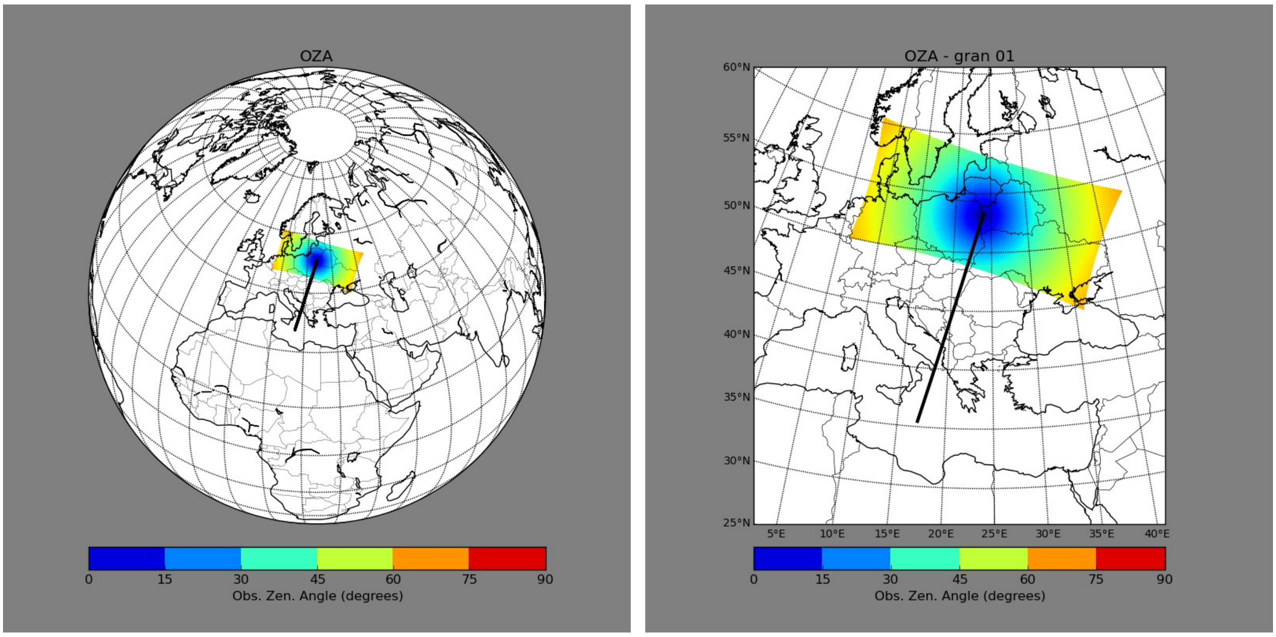

Figure 2.34 : Observation (sensor viewing) Zenith Angle -OZA for 3MI spectral SWIR channel 1

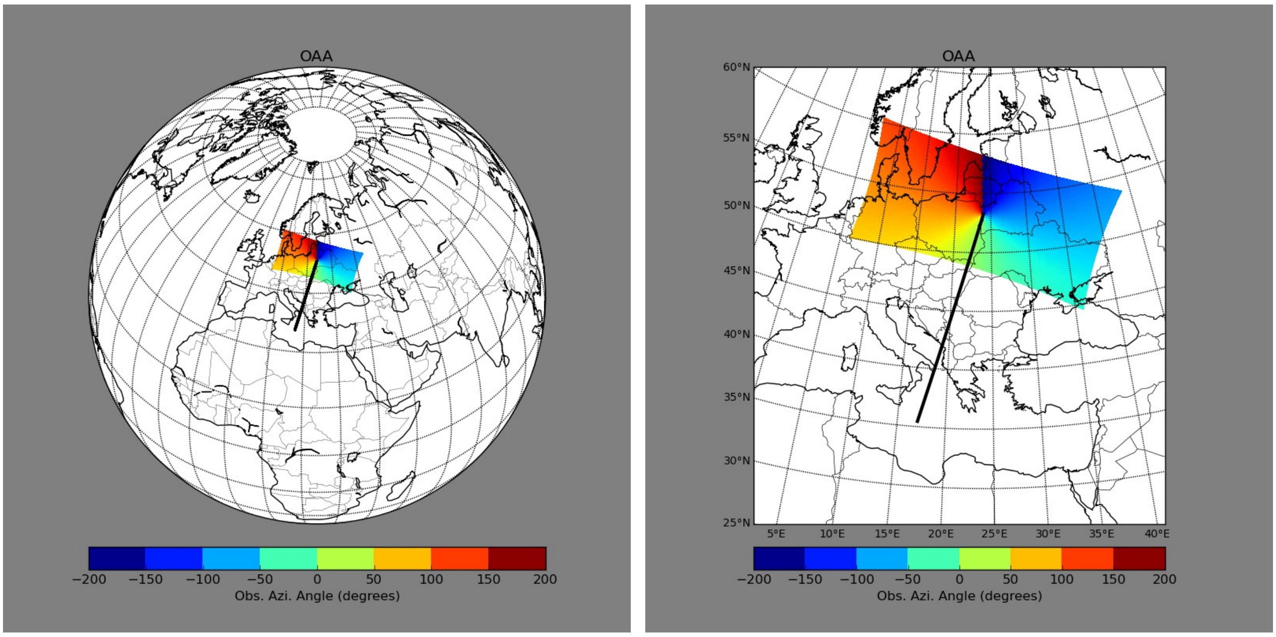

Figure 2.35 : Observation (sensor viewing) Azimuth Angle – OAA for 3MI spectral SWIR channel 1

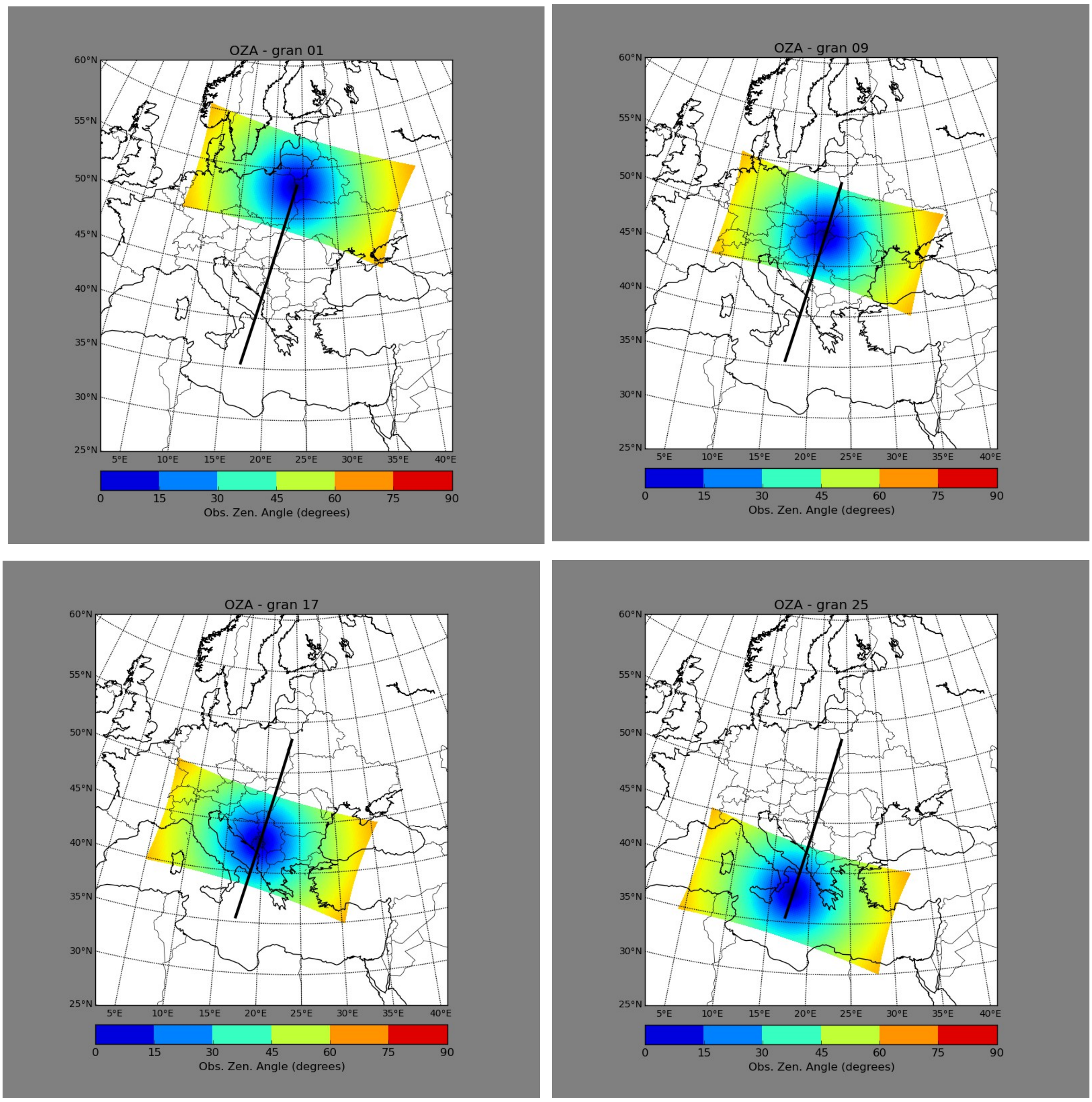

Figure 2.36 : Evolution of the observed scene - granule 1 (upper left), 9 (upper right), 17 (lower left) and 25 (lower right) - for the OZA of 3MI-SWIR-1

2.3.4.1 DEM corrections:

ACE2 DEM over the scanned areas

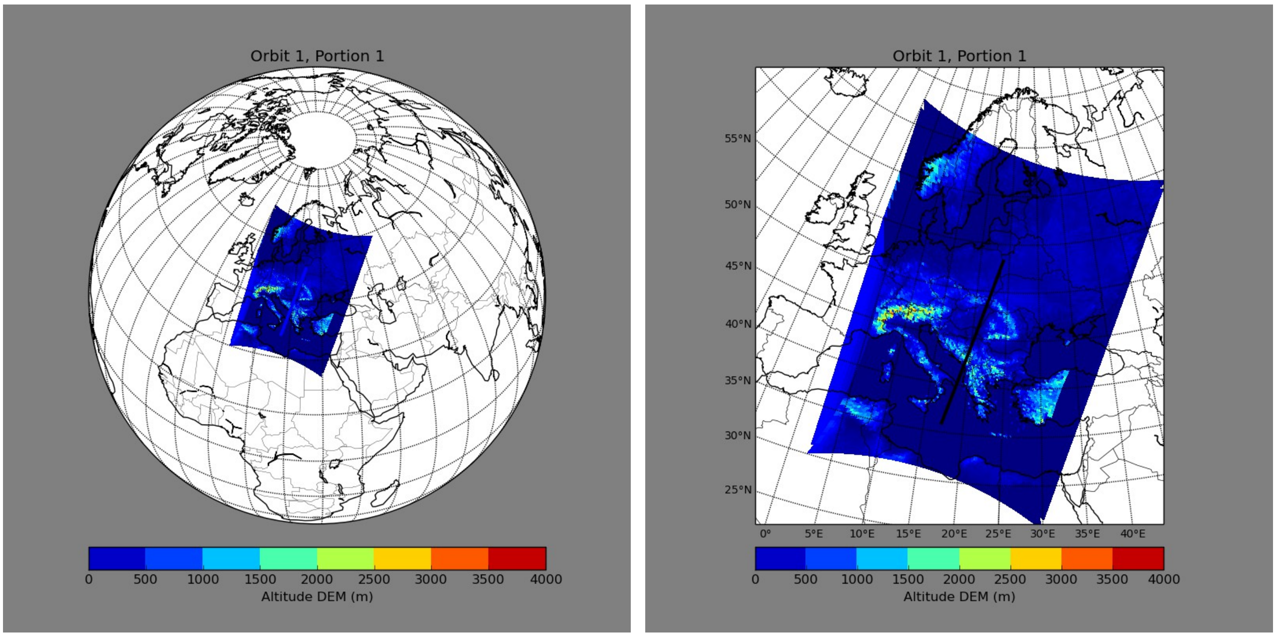

Figure 2.37: ACE2 DEM for the area scanned by 3MI-VIS

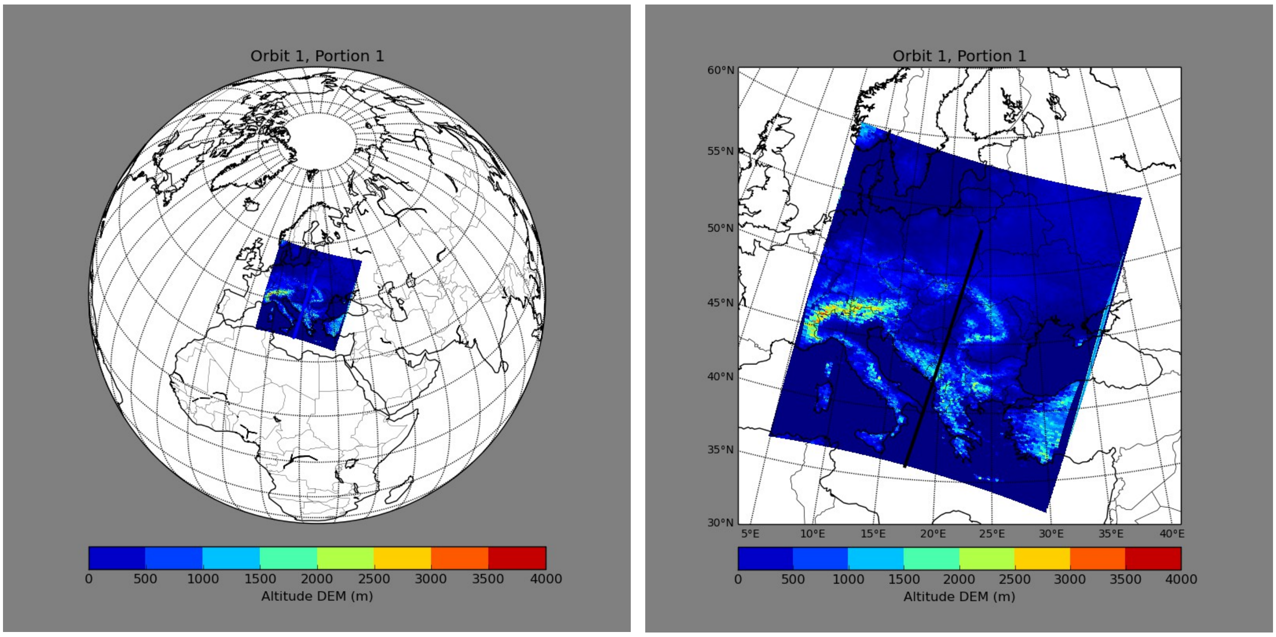

Figure 2.38: ACE2 DEM for the area scanned by 3MI-SWIR

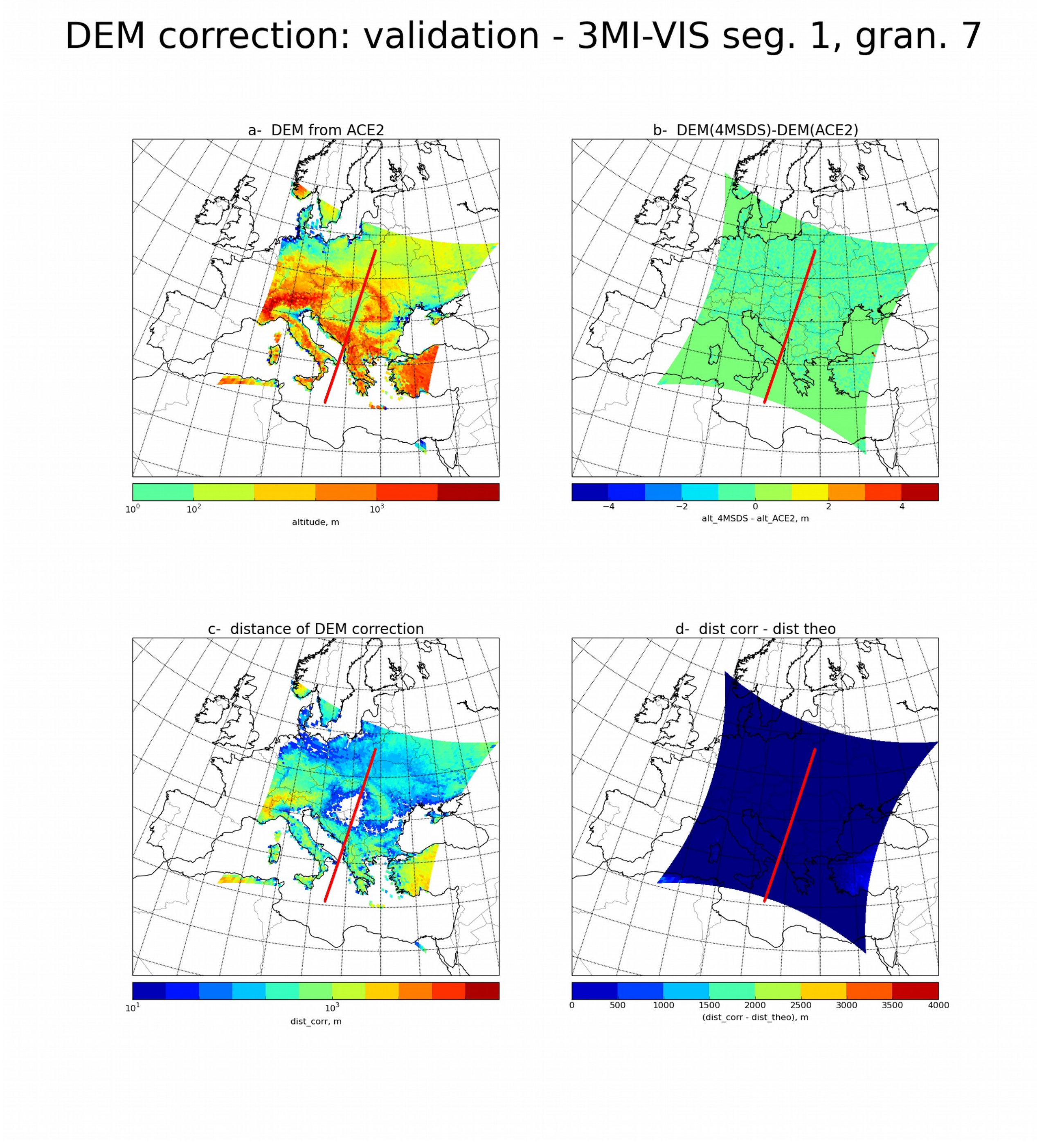

Figure 2.39: DEM correction: a) Altitude for the ACE-2 DEM in m, b) difference for each pixel between the altitude of the pixels of 3MI-VIS in 4MSDS project and the altitude delivered by ACE2, in m. c) Effect of the DEM correction: shift in m in direction of the track d) Difference in m between the shifted distance of the algorithm of DEM correction (dist_corr) and the theoretical distance of shift computed with the tangent method presented in Section 2.1.5. (dist_theo)

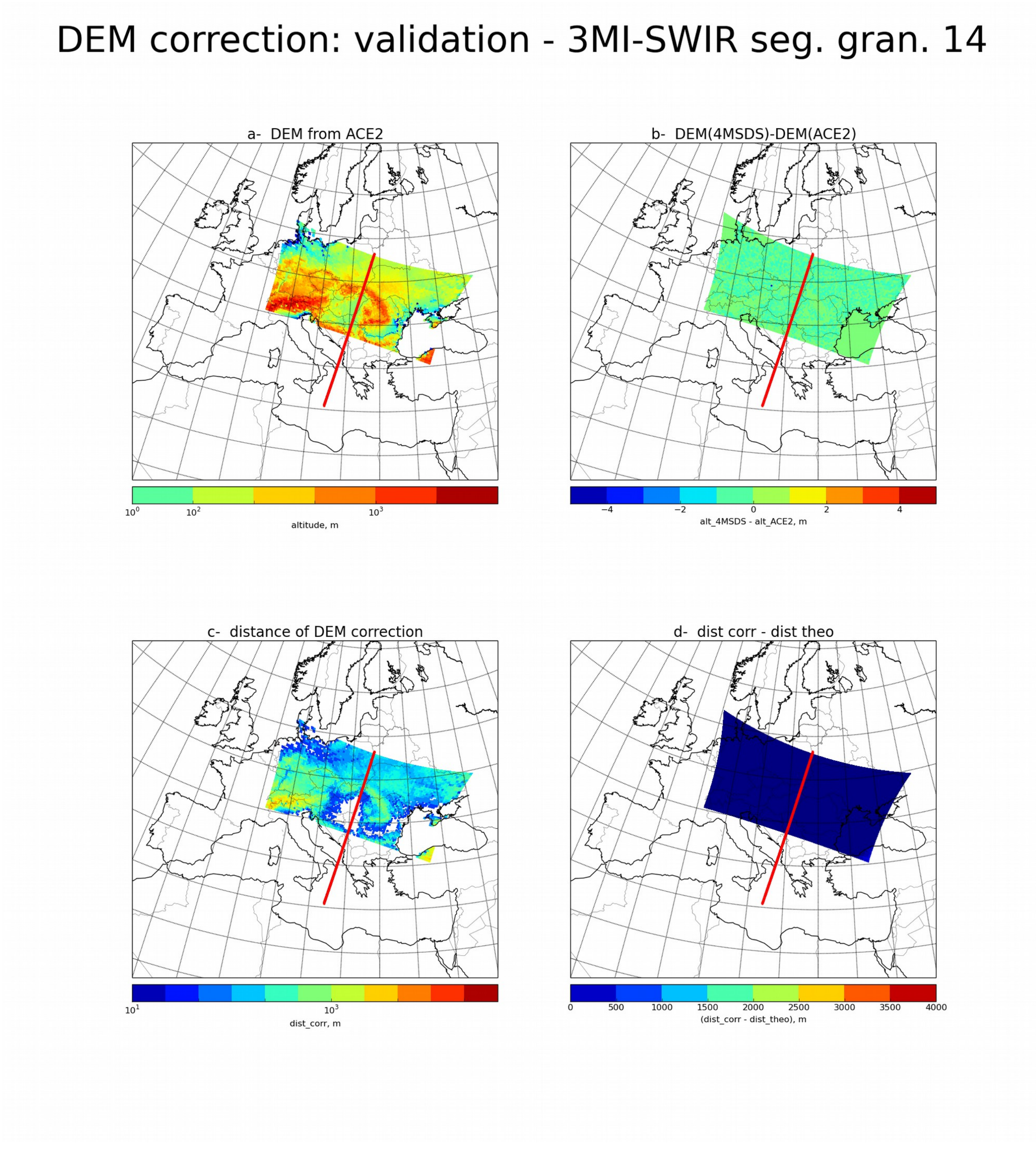

Figure 2.40: DEM correction: a) Altitude for the ACE-2 DEM in m, b) difference for each pixel between the altitude of the pixels of 3MI-SWIR in 4MSDS project and the altitude delivered by ACE2, in m. c) Effect of the DEM correction: shift in m in direction of the track d) Difference in m between the shifted distance of the algorithm of DEM correction (dist_corr) and the theoretical distance of shift computed with the tangent method presented in Section 2.1.5. (dist_theo)

Effects of the DEM-correction algorithm

We zoom on the mountain chain of the Piz Bernina (Bordery Swiss-Italy in the Alps, between Milan and the Lichtenstein), West of the nadir track of the satellite, and we compare the centres of the pixels with and without DEM correction, for the 3MI-VIS-2 channel.

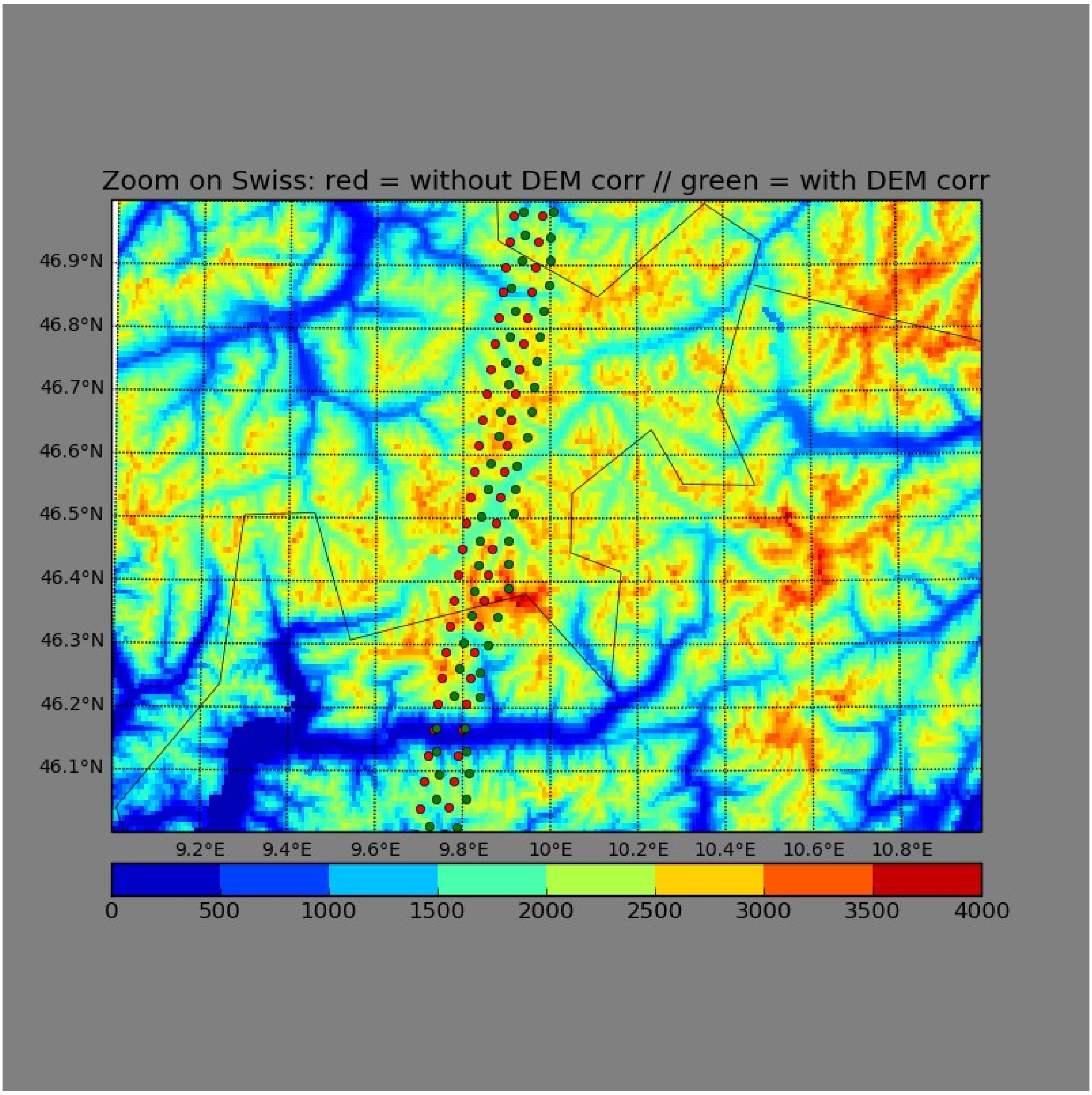

Figure 2.41: DEM correction (green) compared to pixels projected on the Earth Ellipsoid (red). The shift due to the DEM correction is in direction of the nadir track (East of the pixels). The higher are the mountains, the larger is the shift. The zoom is done on the mountain chain Piz Bernina (Bordery of Swiss and Italy, in the Alps, between Milan and the Lichtenstein) – ***3MI-VIS-2 channel***

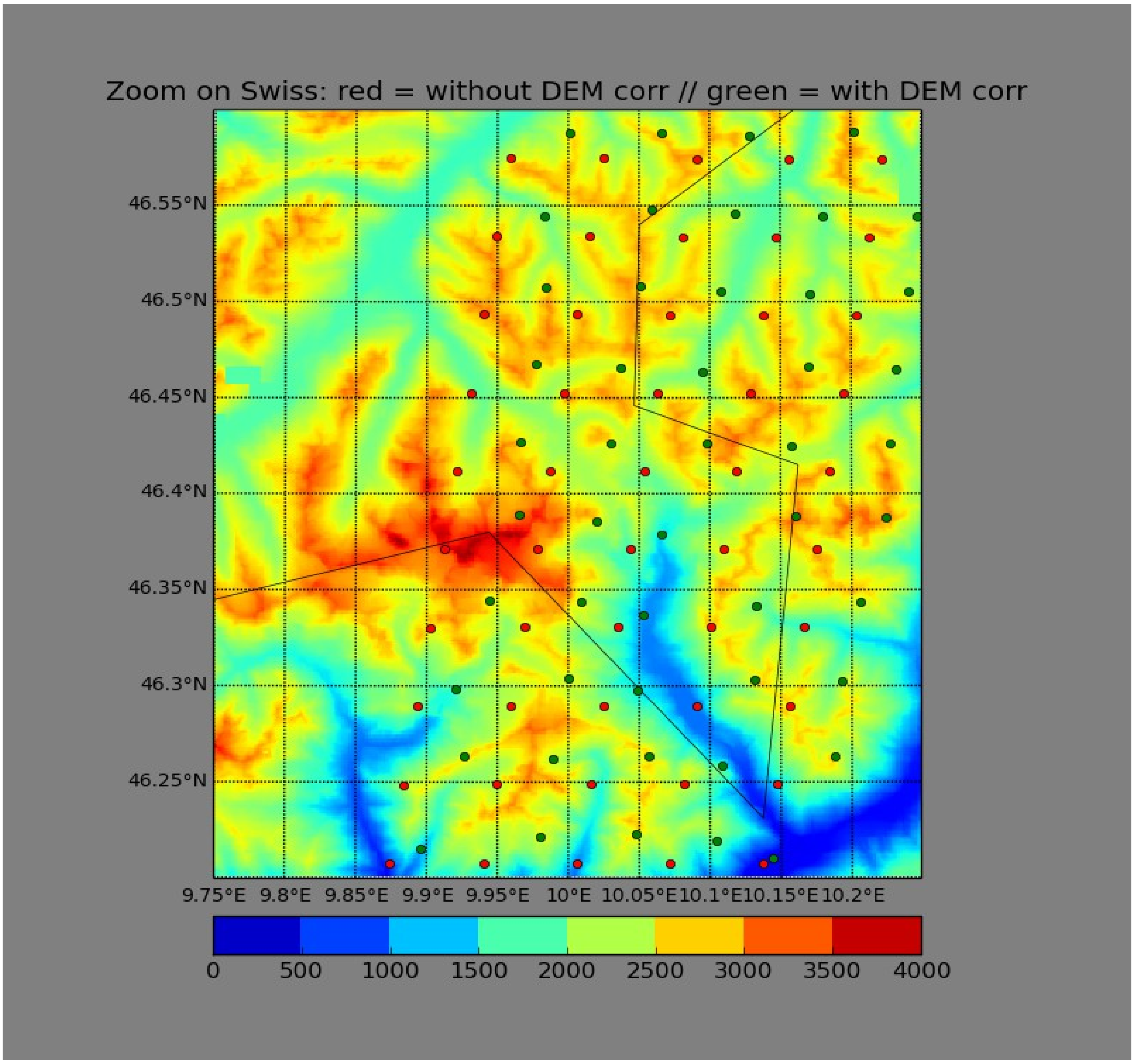

*Figure 2.42: Same as Figure 2.41, with a larger zoom on the area. 5 series of pixels instead of 2 are shown. - **For 3MI-VIS-2 channel**.*

2.3.5 Illustration for complete orbits and comparison with AVHRR.

2.3.5.1 Comparison between AVHRR and METImage.

The METImage has similar characteristics to AVHRR in terms of scanning geometry and field of view.
For the 4MSDS project, we simulated the channels of VII for 3 orbits corresponding to the current satellite MetOp carrying AVHRR (orbit 1 = 12 September 2007, 08:43:03; orbit 2 = 12 September 2007, 10:22:33; orbit 3 = 23 February 2008, 8:46:02).
Therefore, we can control if the scanned area simulated for VII indeed matches the area scanned by AVHRR. Figures 2.43 to 2.48 illustrate that there is indeed a full match between the assumed AVHRR swath and the simulated VII swath resulting from our simulation.
To ease comparison, we illustrate the comparison by plotting the AVHRR sub-sampled geolocation grid on top of our simulated VII swath.

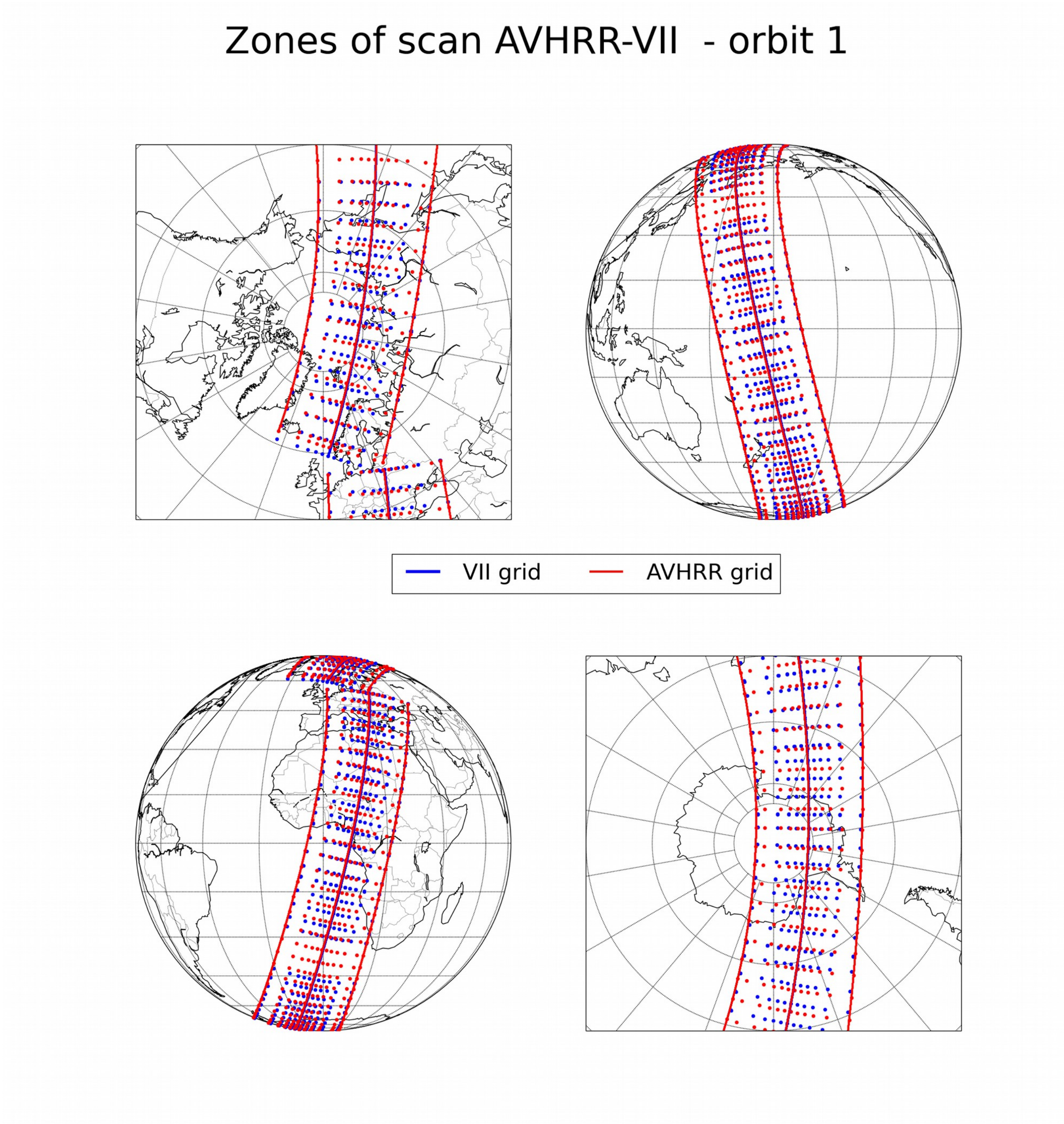

Figure 2.43: For the orbit 1, match between the scanned areas (simplified grid) of METImage (VII in blue) and AVHRR (in red). The satellite trace and the band scanned match perfectl, and the pixel lines of the two instruments are parallels.

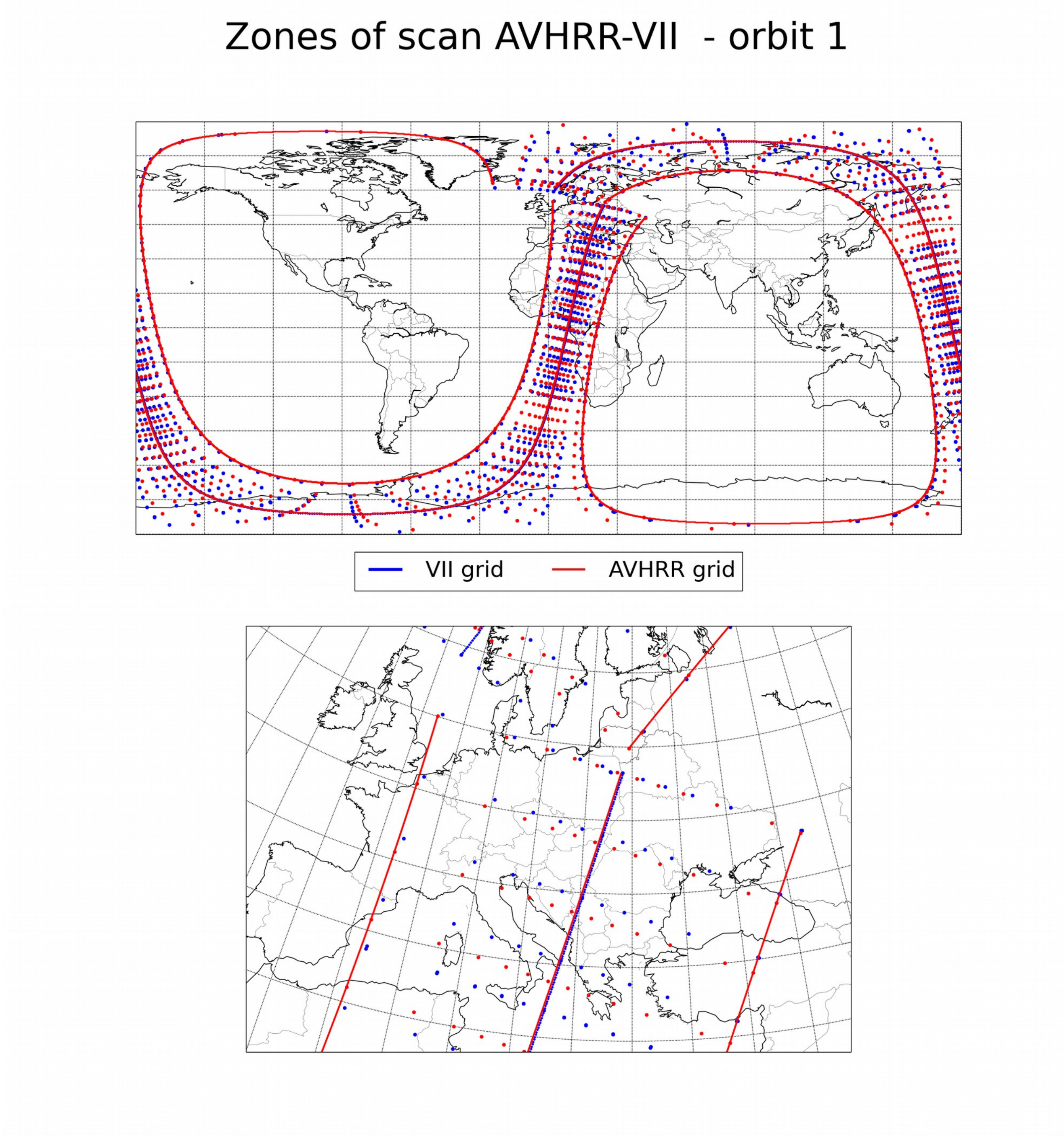

Figure 2.44: For the orbit 1, match between the scanned areas (simplified grid) of METImage (VII in blue) and AVHRR (in red). Same as Figure 2.43, but with an other geometric projection.

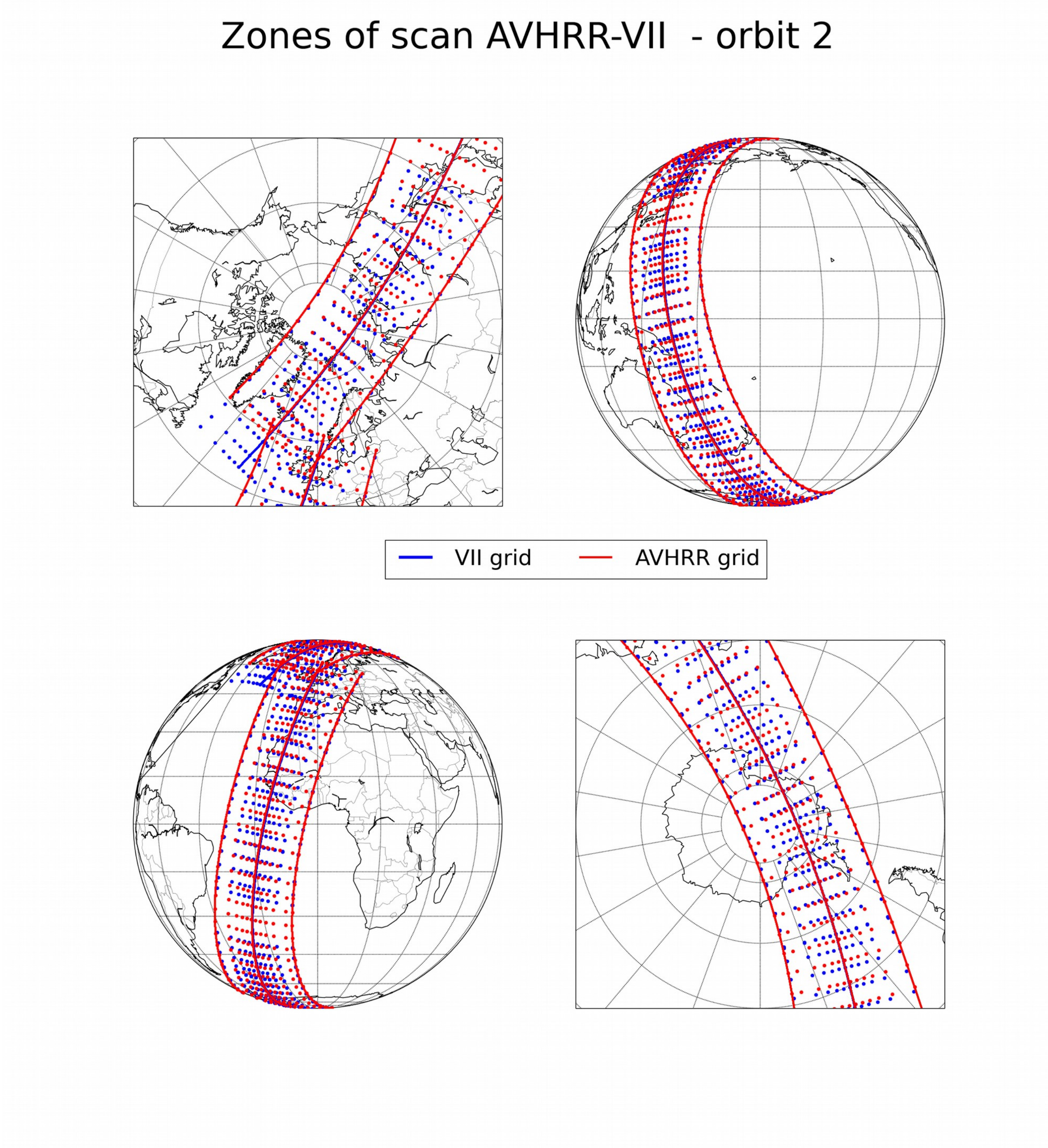

Figure 2.45: For the orbit 2, match between the scanned areas (simplified grid) of METImage (VII in blue) and AVHRR (in red). The satellite trace and the band scanned match perfectly, and the pixel lines of the two instruments are parallels.

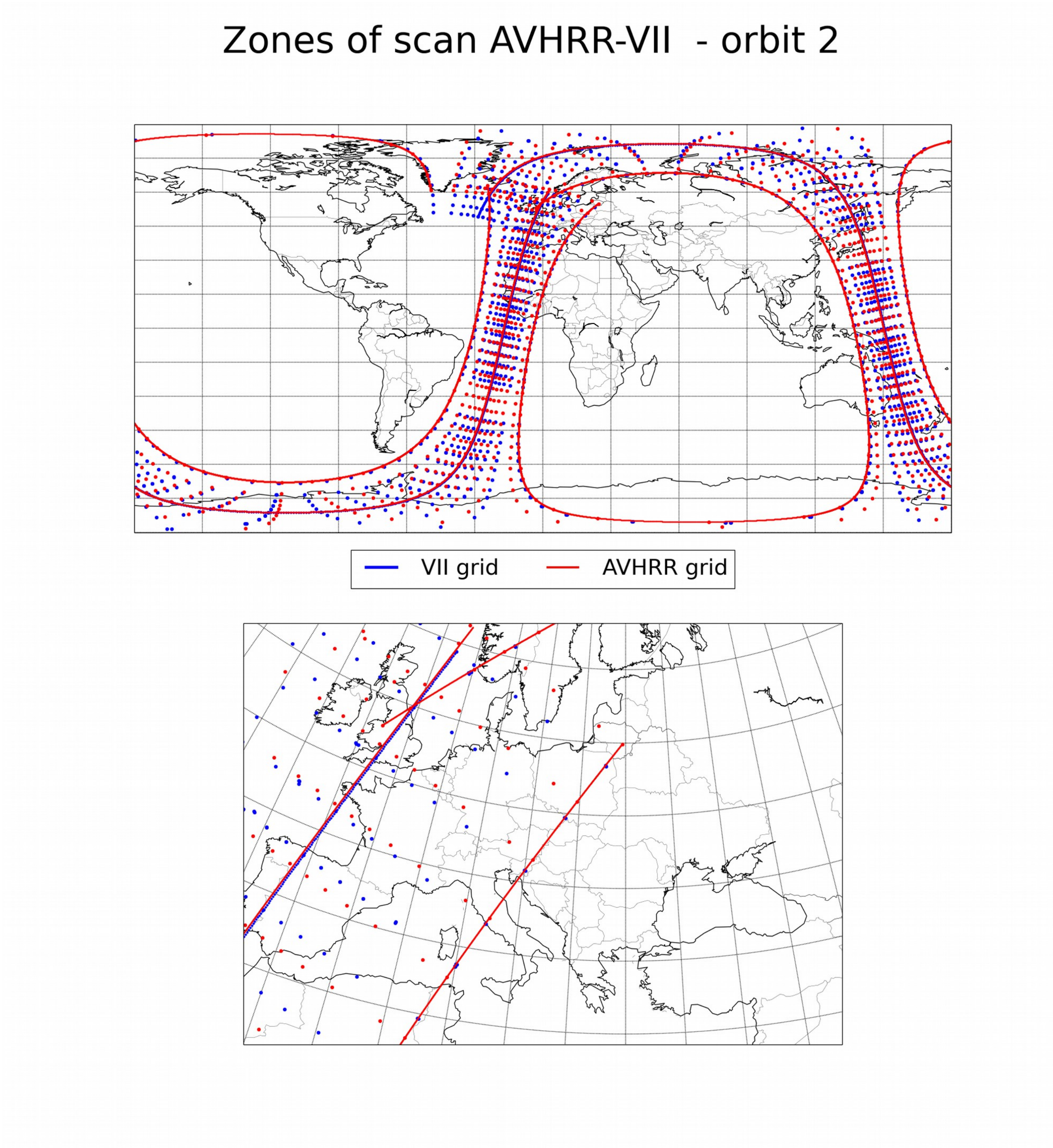

Figure 2.46: For the orbit 2, match between the scanned areas (simplified grid) of METImage (VII in blue) and AVHRR (in red). Same as Figure 2.45, but with an other geometric projection.

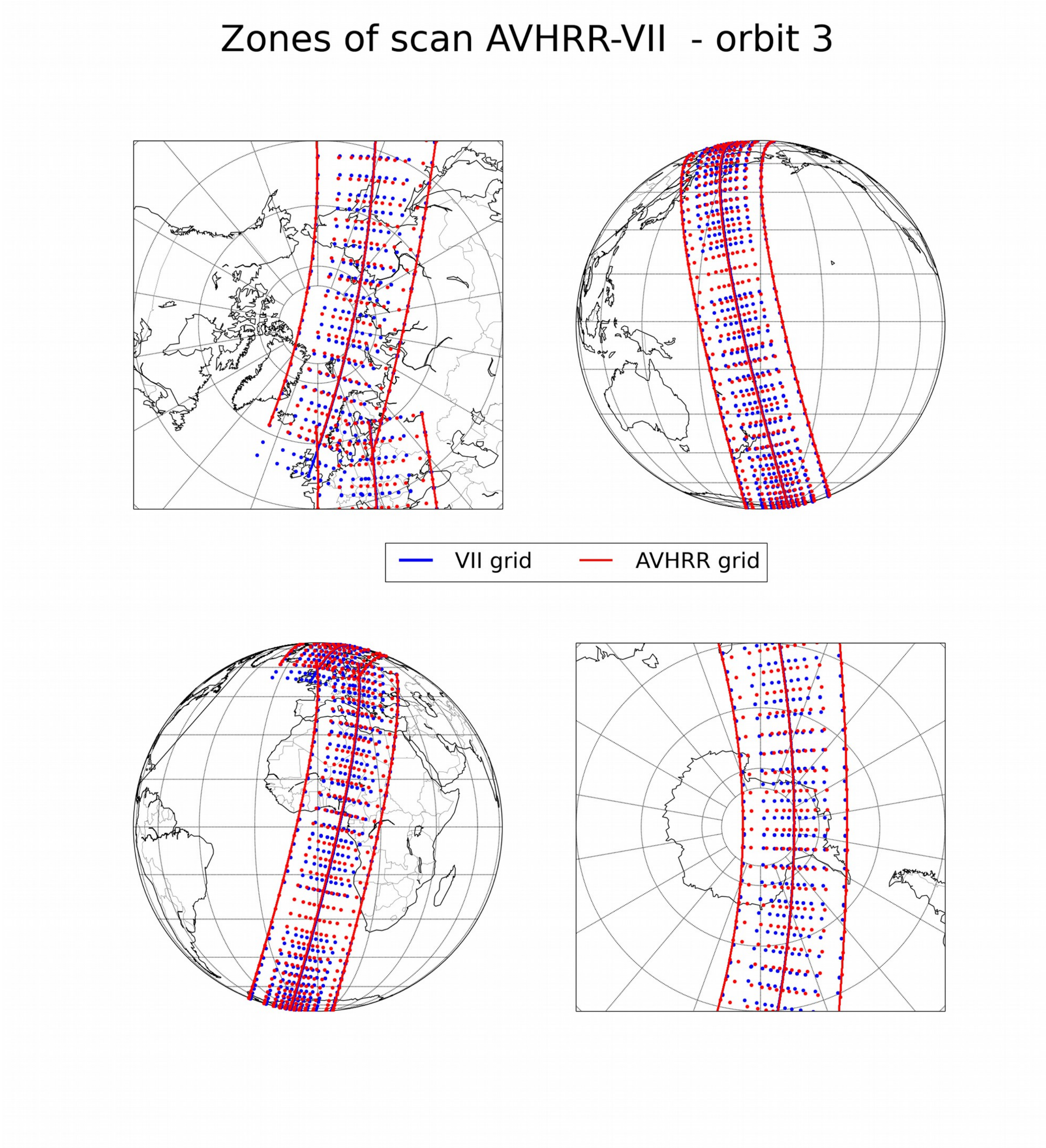

Figure 2.47: For the orbit 3, match between the scanned areas (simplified grid) of METImage (VII in blue) and AVHRR (in red). The satellite track and the band scanned match perfectly.

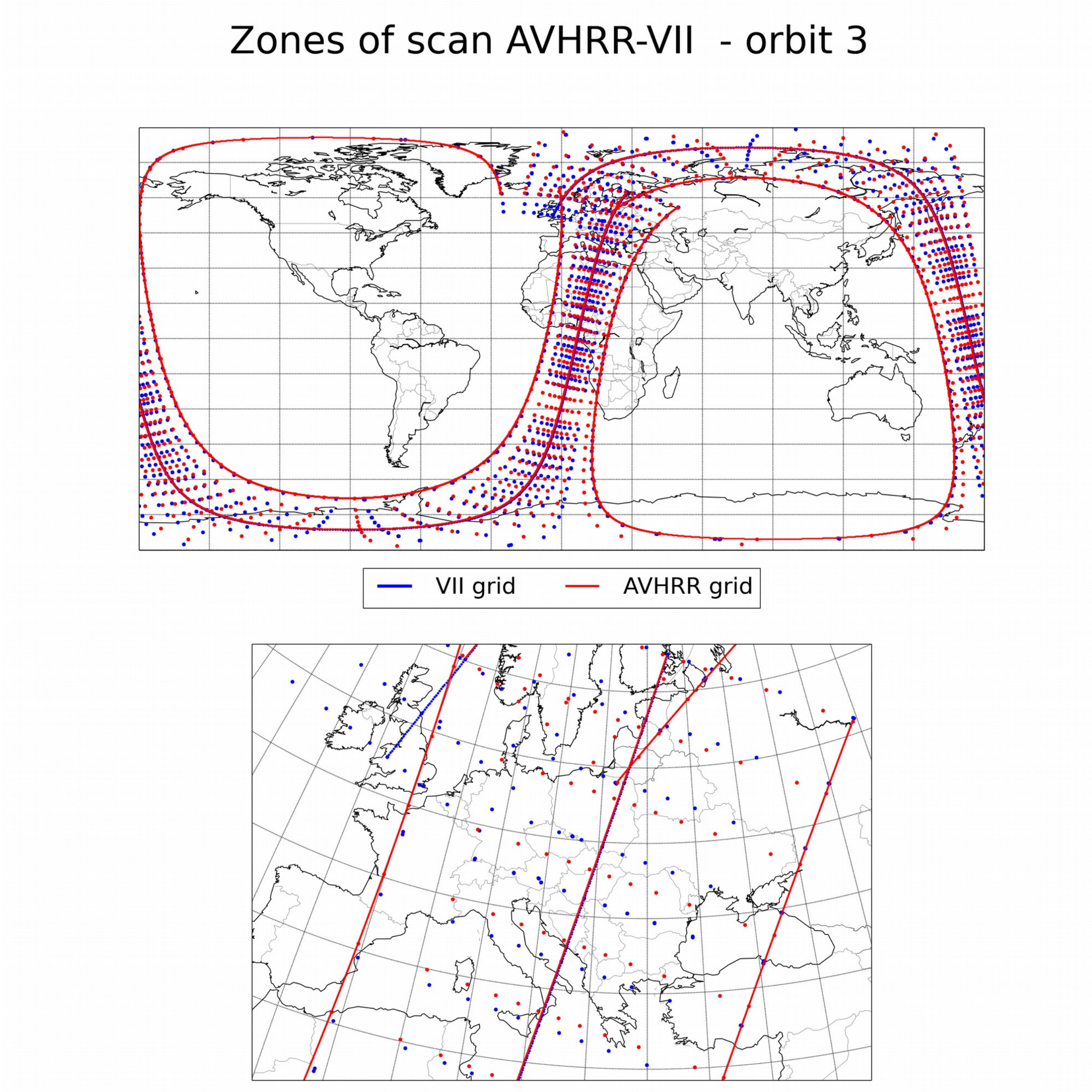

Figure 2.48: For the orbit 3, match between the scanned areas (simplified grid) of METImage (VII in blue) and AVHRR (in red). Same as Figure 2.47, but with an other geometric projection.

2.3.5.2 Solar angles along the orbits for METImage

In this part we illustrate the evolution of the solar zenith angle (SZA) and the solar azimuth angle (SAA) along the orbits for the area scanned by METImage.

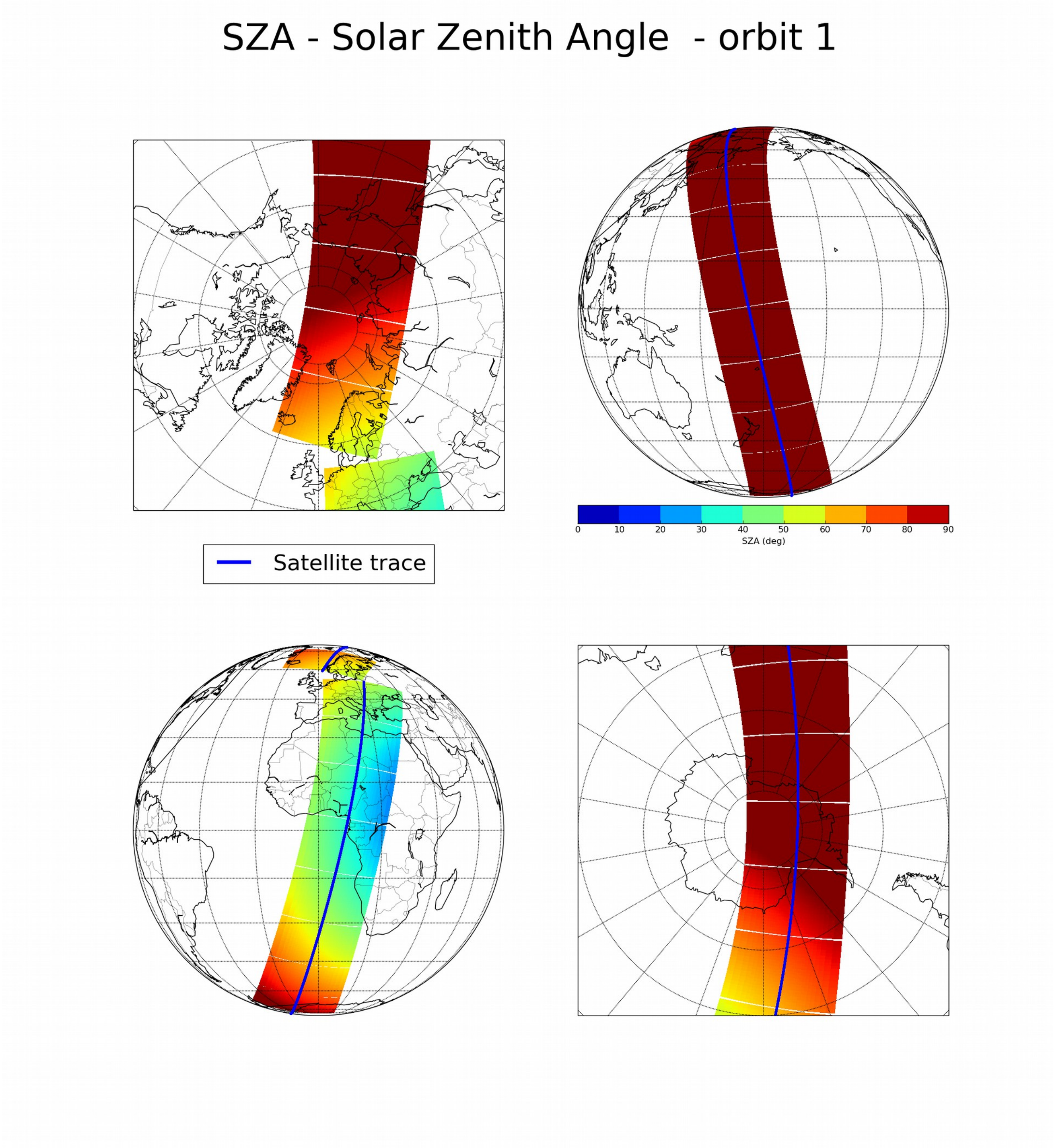

Figure 2.49: Solar Zenith Angle (SZA), along orbit 1.

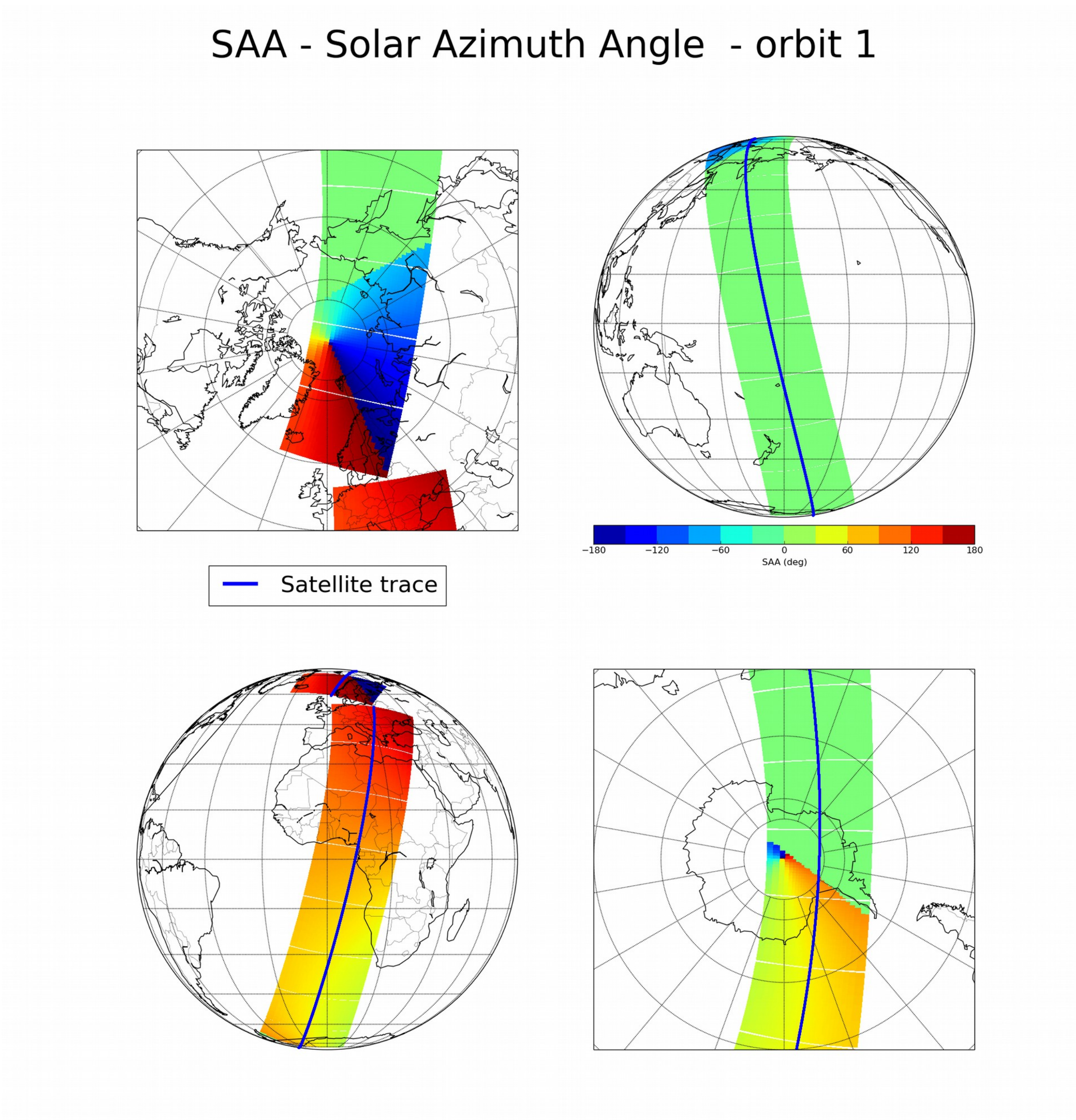

Figure 2.50: Solar Azimuth Angle (SAA), along orbit 1. The green areas are the areas of night flag (SAA forced to 0). The convention is clock-wise = positive, 0° corresponds to the North direction. The rapid switches blue to red in a given geographic area correspond to a variation from +179 to -179 (= +179 to +181), it is a periodicity effect of the chosen colour-scale, not a brutal change in the direction of the sun.

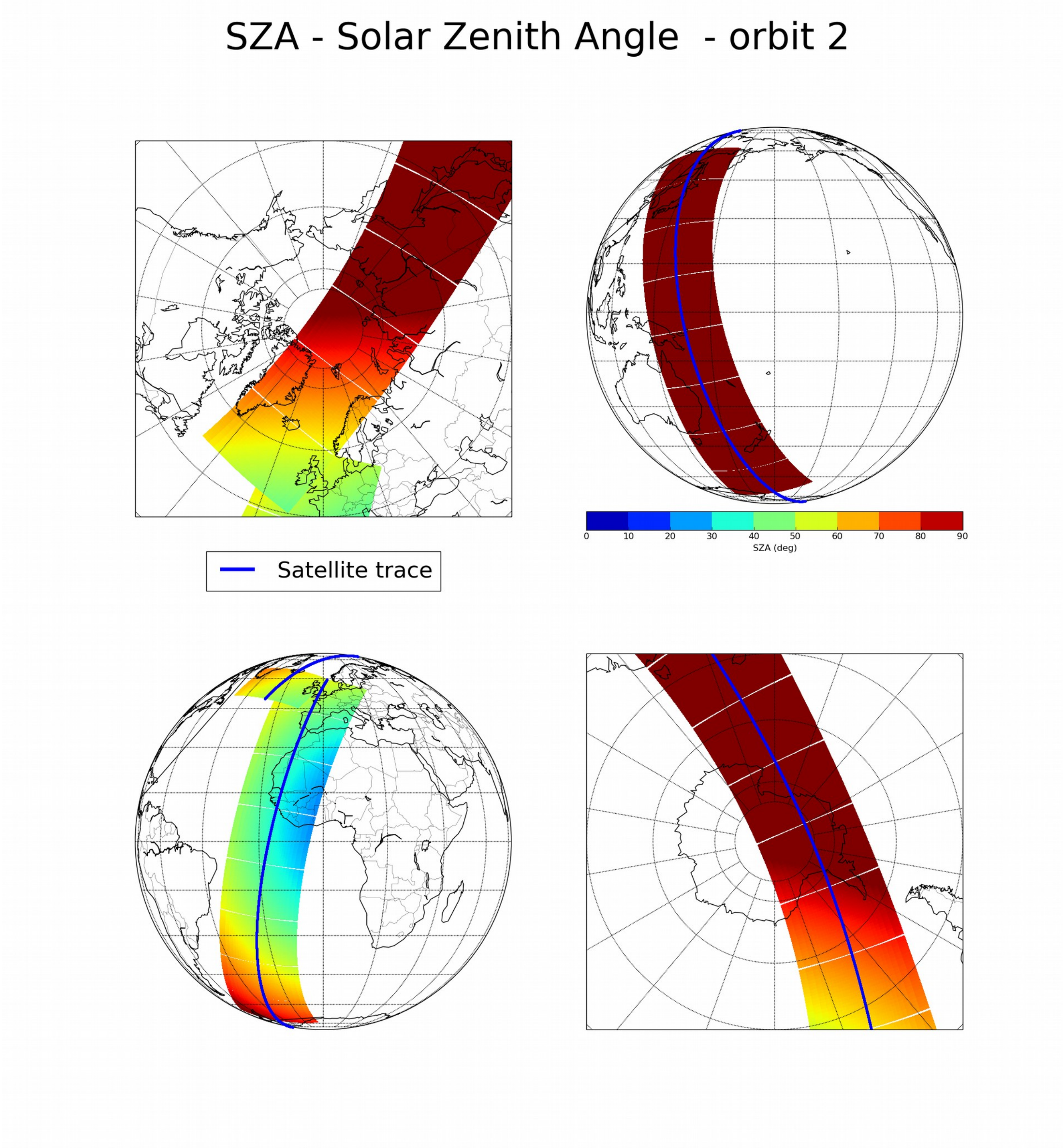

Figure 2.51: Solar Zenith Angle (SZA), along orbit 2.

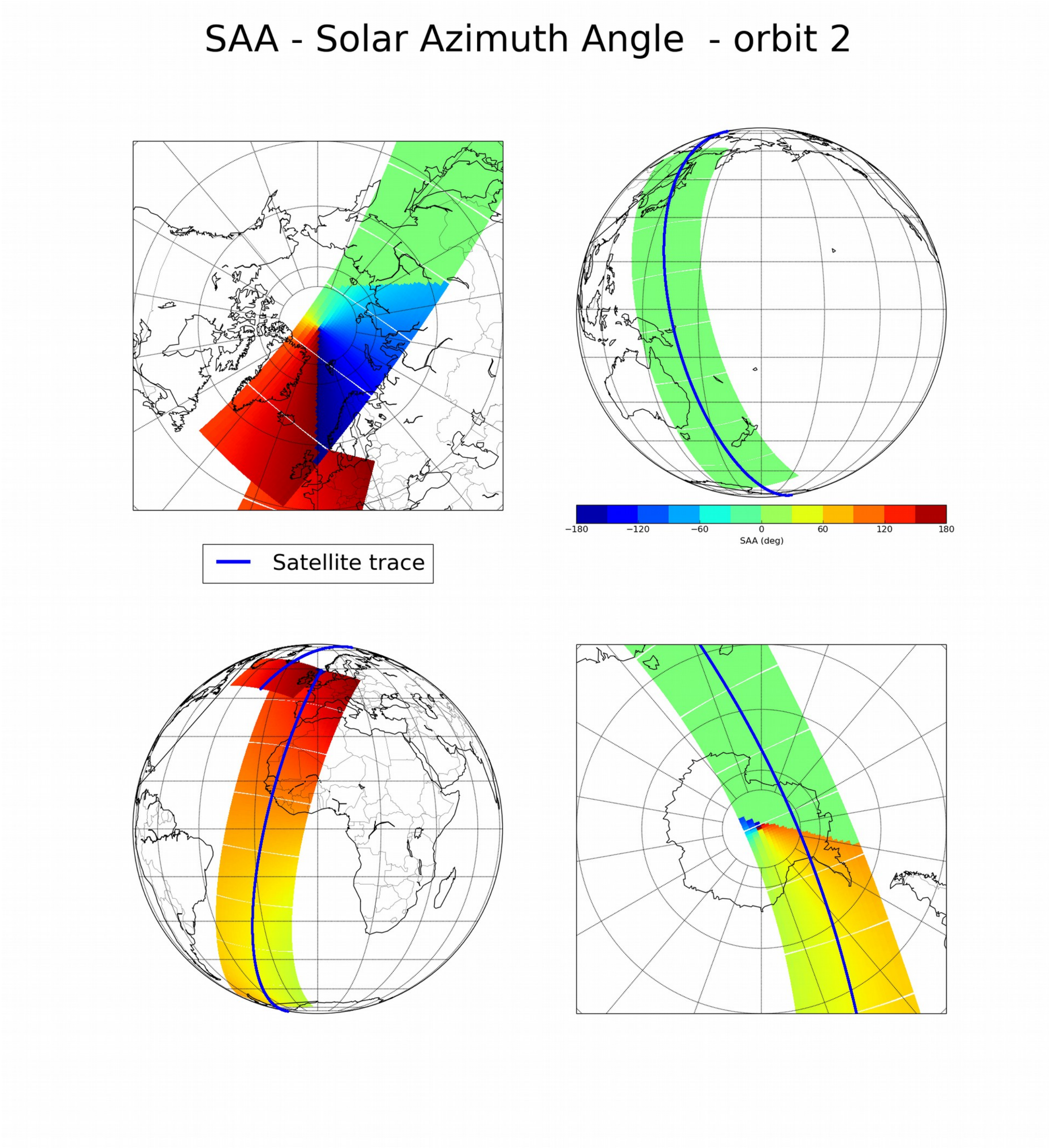

Figure 2.52: Solar Azimuth Angle (SAA), along orbit 2. The green areas are the areas of night flag (SAA forced to 0). The convention is clock-wise = positive, 0° corresponds to the North direction. The rapid switches "blue to red" in a given geographic area correspond to a variation from +179 to -179 (= +179 to +181), it is a periodicity effect of the chosen colour scale, not a brutal change in the direction of the sun.

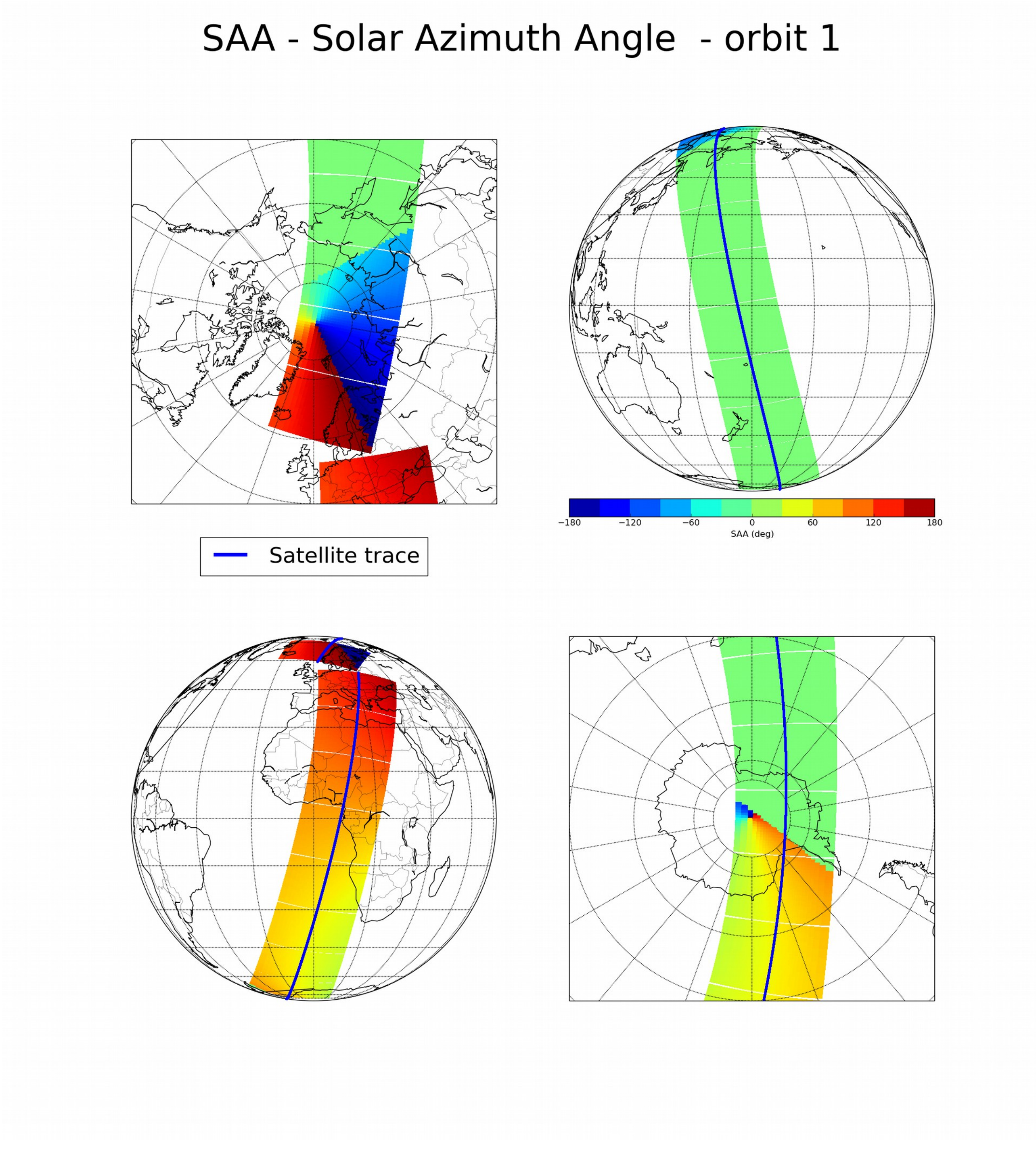

Figure 2.53: Solar Azimuth Angle (SAA), along orbit 1. The green areas are the areas of night flag (SAA forced to 0). The convention is clock-wise = positive, 0° corresponds to the North direction. The rapid switches "blue to red" in a given geographic area correspond to a variation from +179 to -179 (= +179 to +181), it is a periodicity effect of the chosen colour scale not a brutal change in the direction of the sun.

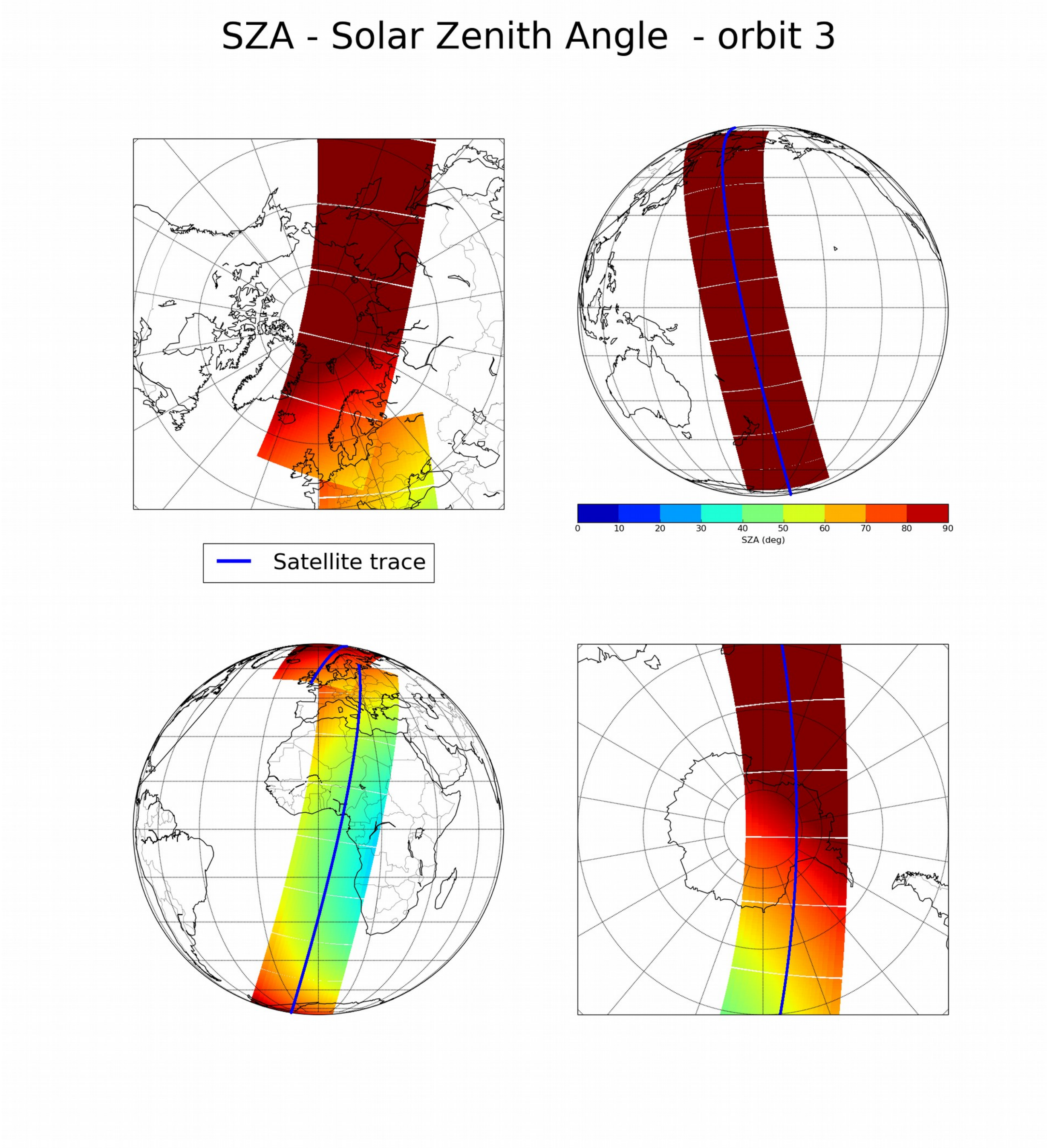

Figure 2.54: Solar Zenith Angle (SZA), along orbit 3.

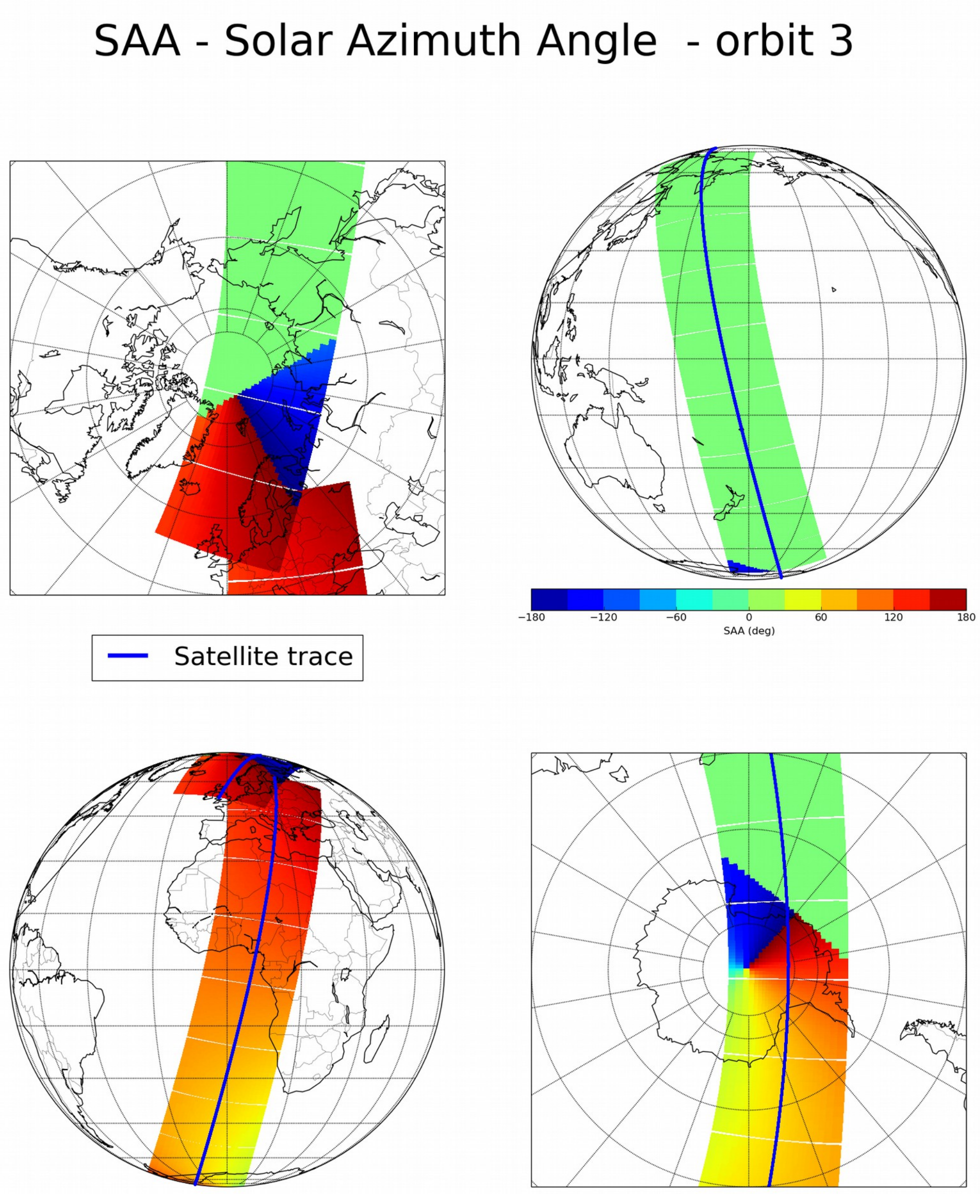

Figure 2.55: Solar Azimuth Angle (SAA), along orbit 3. The green areas are the areas of night flag (SAA forced to 0). The convention is clock-wise = positive, 0° corresponds to the North direction. The rapid switches "blue to red" in a given geographic area correspond to a variation from +179 to -179 (= +179 to +181), it is a periodicity effect of the chosen colour-scale, not a brutal change in the direction of the sun.

3 Simulation of 3MI and METImage (VII) channels with MOMO and ARTDECO

As proposed in the technical management proposal, the 4MSDS (METImage/3MI Synthetic Dataset Simulator) project intends to simulate all the radiances measured by the future instruments METImage (also named VII: Visible and Infrared Imager) and 3MI (Multi-Viewing, Multi-Channel, Multi-Polarization Imager). For this purpose the ISS (Institute for Space Sciences) of the FUB (Freie Universität Berlin), initially proposed a simulation method to perform simulations for the VII instrument, and the LOA (Laboratoire d'Optique Atmosphérique) of the Université de Lille-1 has been responsible for the simulations for the 3MI instrument.

In this section we describe the two simulators setup for VII and 3MI.

- In Section 3.1, we present the general architecture of a simulator and discuss the different methods of simulations used in the 4MSDS project: direct simulation for 3MI and LUT (Look-up-Table) method for METImage.
- In Section 3.2, we describe the inputs of the simulator, their units, the origin, and, the format of the data. We also explain the format of the outputs (results of the study) and give some computation time indications for the final simulations of the 3 orbits.
- In Section 3.3, we discuss the 1-D radiative transfer simulations, namely the approximation that have to be made to achieve realistic computation time while achieving reasonable accuracy (gas transmission, k-distribution, approximation for the computation of the scattering, Fourier terms, angles/fluxes that are computed). We evaluate the gain in computation time that these approximations induce and the loss of precision that they cost. We show also some validation of the radiative transfer tools and some cross comparisons between the radiative transfer code of the LOA (ARTDECO: Atmospheric Radiative Transfer Database for Earth Climate Observation) and the one of the FUB (MOMO: Matrix-Operator Model).
- In section 3.4, we present the conditions and the results of a first, restricted and simple preliminary simulation and discuss the first results.

3.1 Methods of simulation: direct simulation and LUT (Look up Tables), radiative transfer codes

The principle of a simulator is shown on Figure 3.1. The simulator takes information from a database containing general properties of the instrument (e.g. the response function of the instrument's channel, spectral channels), and the properties of the atmosphere and ground constituents (e.g. the single scattering and the phase function of the aerosols and clouds). The simulator needs also to know the pixel state, namely to have a precise definition of the pixel position, ground properties, atmospheric properties (ancillary data, clouds and aerosols masks, optical depths and vertical distributions) and specific viewing geometries for that particular pixel . From these sources of information, the simulator can, using a radiative transfer code, simulate the radiance coming from the pixel to the instrument and store it in the results data.

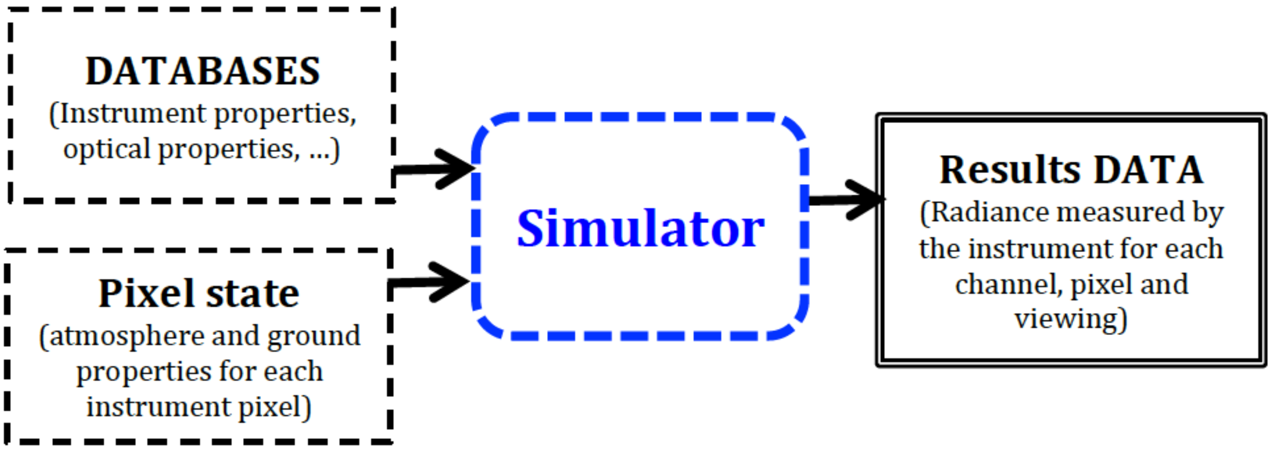

Figure 3.1: *Basic schematics of a simulator for a spaceborne instrument: The simulator needs information from databases and about the properties of the simulated pixels, and provides the results data. This results data contain the radiances that would be measured by the instrument for each pixel.*

In the 4MSDS project, we initially adopted two different methods of simulation to respond to the different needs of each instruments:

- The direct simulation method for the 3MI dataset at LOA. In this case, the simulator solves the 1-D RTE (Radiative Transfer Equation) “on the fly” for each pixel. This method is presented in Subsection 3.1.1.

- The LUT (Look-up-Table) method for the simulations of METImage at the FUB. In this case, the simulations are done in two steps: First the creation of the LUT, for some representative situations, then the interpolation of the radiances measured by the instrument for each pixels, from the values of the LUT. The LUT method is presented in Subsection 3.1.2.

In Subsection 3.1.3, we briefly present the 2 radiative transfer codes used in the project: ARTDECO (Atmospheric Radiative Transfer Database for Earth Climate Observation) for the LOA and MOMO (Matrix Operator Model) for the FUB.

3.1.1 Direct method: The LOA simulator for 3MI

The LOA simulator for 3MI follows a direct method. We note that it can also generate METImage dataset for cross-validation purpose between the two simulators (FUB and LOA). The LOA simulator consists of a Python wrapper around the ARTDECO radiative transfer tool that is written in Fortran (described in Subsection 3.1.3.1). The principle is presented on Figure 3.2. It can be separated into 4 steps:

- Step 1: for any pixel to be computed, the simulator (blue box on Figure 3.1) retrieves the scene state (i.e. the ancillary data : cloud mask, meteorology, ground properties etc, from WP3), the scene geometry (solar and viewing zenith and azimuthal angles from WP1) and libraries of pre-computed data such as the cloud and aerosols optical properties or gas absorption coefficients. All these informations are stored and read from pre-established HDF files. This step is performed using a Python-based software only.
- Step 2: the simulator processes all informations about the scene to prepare the effective optical properties of atmospheric layers and ground that is the input for the RTE solver. This step is operated by both Python and ARTDECO. It can include operations such as interpolation of the ancillary data (e.g. wavelength interpolation of MODIS ground albedo product). Any assumption on the scene definition (e.g. selection of gas to be accounted for absorption) or threshold (e.g. no computation for solar zenith angles > 80.0 degrees) are applied.
- Step 3, the RTE is solved. It is operated by ARTDECO and is the most time consuming part of the process. The ratio accuracy/ computational demand is easily adjustable. We discuss that point in Section 3.3. ARTDECO includes several RTE solver. We choose an adding and doubling solver that allows to account for polarization and ground bidirectional reflectance. We describe further the RTE solving in Subsection 3.1.3.1.
- Step 4, the simulator stores the result in a file (HDF5 format). That step is performed by Python-based software only. .

The simulator is accelerated through parallel computation managed with the Sun Grid engine queuing system. The simulator is then ready for use on clusters of computer. In this section we present preliminary results obtained during simulator setup by running the simulator on LOA720 server (cluster of 8 computer of 16 CPUs each) in Subsection 3.4.1 .

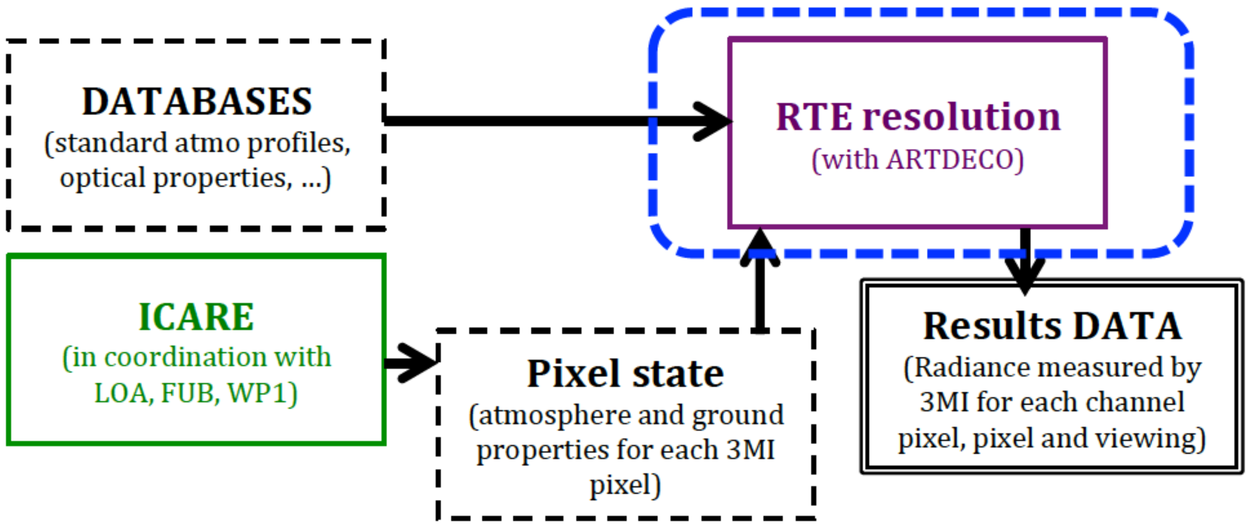

Figure 3.2: *Schematics of the simulator of the LOA, using the direct method for the instrument 3MI. The 1-D radiative transfer code used to solve the RTE (Radiation Transfer Equation) is ARTDECO of the LOA. The simulator contains only the module that actually solves the RTE.*

3.1.2 LUT (Look up Table) method: The FUB simulator for METImage

Simulations for the METimage dataset were intended to provide radiances consistent with the large base of heritage simulations for MERIS (Medium Resolution Imaging Spectrometer on board of ESA's satellite ENVISAT) and MODIS (Moderate Resolution Imaging Spectroradiometer on board of NASA's satellites Aqua and Terra) like instruments. For the simulation of these radiances, the ISS group of the FUB made the choice to use a LUT (Look-up-Table) method. The reason of this choice was to reduce computational time without loss of accuracy. The 1-D radiative transfer code MOMO (Matrix Operator Model, see description in Subsection 3.1.3.2) is using a very precise matrix-operator method and computes the radiances for a large set of angles. For a given pixel, only one solar direction and one viewing direction are of interest for the project and are output in the final results data (Results DATA box on Figure Figure 3.1). It would be a waste of time for MOMO to only keep less than 0.004 % of the data computed in the results. And because of the high standard of precision that the matrix-operator method requires, FUB initially estimated that the computation time for a single pixel and for the 20 channels would be 4500 seconds/CPU with the direct method.

In contrast, with an adequately defined Look-up-Table, and thanks to a fast interpolator (see Figure 3.3), we estimate (see time estimation in Section 3.2) that we can build the Look-up-Table in 500 to 2000 days/CPU and interpolate an orbit in 2000 to 6000 hours/CPU.

The principle of the Look-up-Table method is presented on Figure 3.3. It is more complicated than the principle of the direct simulations method (Figure 3.2).

The simulator (blue box of Figure 3.1) contains 2 tables (IPLT and LUT, see Figure 3.3) and two modules (RTE resolution – purple box on Figure 3.3 - and the interpolator - red box).

The process is done in two steps.

First the building of the LUT (Look-up-Table) after having defined the IPLT (Input Parameters and Limits Table). Then, an n-dimensional interpolation from the n-dimensional LUT to each pixel.

In the first step, the LUT has to be built. The LUT is a n-dimensional table containing the results of 1-D radiative transfer simulations for n parameters (e.g. cloud profiles, cloud optical depths, ground albedo), for a large set of solar angles and viewing angles of METImage.

The n parameters and the p values ("Limits") of each parameter for which there is a MOMO simulation are defined for each channel of METImage in the IPLT (Input Parameters and Limits Tables). For example for the channel 5 of METImage (Cloud Top Height, 763 nm) channel, we will make varying n = 6 parameters (ground albedo, 2m Temperature, water vapour column, cloud top height, cloud type, aerosol optical depth). And for the parameter Cloud top Height, we will make a computation for p = 6 different cloud top height, these are the p limits of the parameter "Cloud Top Height" for which we make a radiative transfer simulations. For other cloud top heights of the 4MSDS project, there will be an interpolation between 2 of these limits.

The definition of the parameters and of the limits of the IPLT is currently done throw many fine tests at the FUB, an annex of the WP2 report containing the graphs of these tests will be deliver to the EUMETSAT before the full processing of the LUT. This document will bcontain s an estimation of the errors due to the interpolations between the limits of the IPLT.

Note, that each channel of METImage will have a different IPLT, because the errors due to the interpolations between two limits of a parameter are different for different channels.

The second step is much easier: With an interpolator developed at the FUB, we take the pixel information provided by ICARE (see box "Pixel State" on Figure 3.3 - see also information about the ICARE input parameters in Section 3.2), and we interpolate from the n-dimensional LUT, the radiance observed by METImage for the concerned pixel and for each channel. These radiances are written in the output data with the results (box "Results DATA" on Figure 3.3).

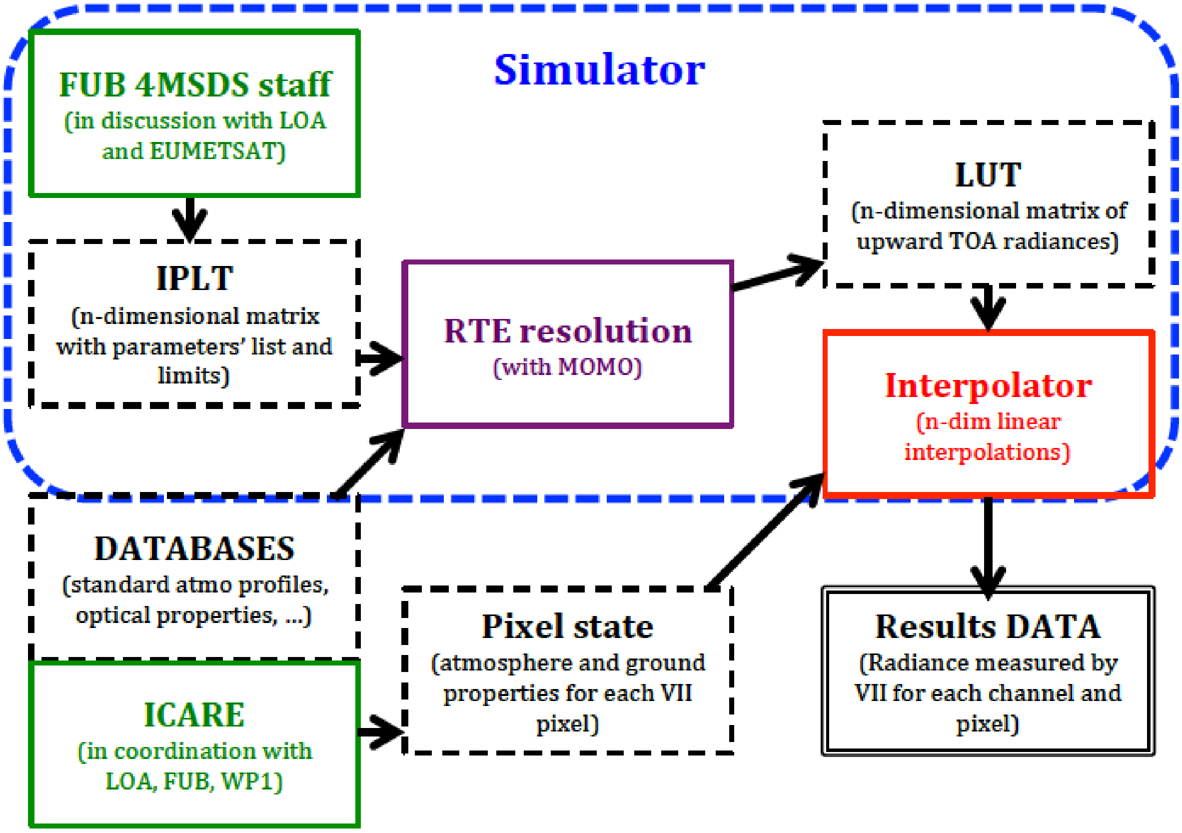

Figure 3.3: *Schematics of the simulator of the FUB, using the LUT (Look-up-Table) method for the instrument METImage (VII). The radiative transfer code used to solve the RTE (Radiative Transfer Equation) is MOMO of the FUB. The simulator is complex: First a table named IPLT (Input Parameters and Limits Table) is built. This table defines the parameters that are simulated and witch values ("limits") are simulated and which values between the limits can be interpolated. The choices of the limits of the IPLT are fixed after a lot of tests. For each combination of parameters limits of the IPLT, a 1-D radiative transfer simulation is done with the RTE resolution module using MOMO. The results of these simulation is a n-dimensional (n are the number of parameters simulated) matrix named LUT (Look-up-Table). From this LUT, the interpolator can compute (using the pixel informations) with a n-dimensional interpolation, the radiance observed by the satellite for each observed pixel. These radiances are the results of the simulation.*

3.1.3 Radiative Transfer Codes: ARTDECO and MOMO

The LOA and FUB simulators make use of two different radiative transfer tools. In this section, we describe the ARTDECO (Atmospheric Radiative Transfer Database for Earth Climate Observation) tool used at LOA and the MOMO (Matrix Opertor Model) tool used by the FUB.

3.1.3.1 ARTDECO by LOA

ARTDECO (Atmospheric Radiative Transfer Database for Earth and Climate Observation) is a numerical tool that gathers models and data for the 1D simulation of Earth atmosphere radiances and radiative fluxes as observed with passive sensors (hyper-spectral excluded) in the UV to thermal IR range. It is developed and maintained at the Laboratoire d'Optique Atmosphérique and is funded by the TOSCA program of the French space agency (CNES). The code is fully written in Fortran. In ARTDECO, users can either access a library for the scene definition (atmosphere profile, surface, aerosol and cloud description, ISRF, etc) or use their own description through input files. The vertical distribution of aerosols and clouds can be arbitrarily and specified as an input. Then, the user can choose among available models (several methods for the truncation of the phase matrix, several RTE solver) to compute radiative quantities corresponding to the scene. Technical parameters (e.g. number of computational angle) for these models are also accessible through input files. The accuracy / computing time ratio can then be easily adjusted. ARTDECO is thus a flexible tool. This tools was validated against other like GAME (Dubuisson, P.; Giraud, V.; Chomette, O.; Chepfer, H. & Pelon, J. Fast radiative transfer modeling for infrared imaging radiometry jqsrt, 2005, 95, 201-220, Dubuisson, P.; Dessailly, D.; Vesperini, M. & Frouin, R. Water vapor retrieval over ocean using near-infrared radiometry Journal of Geophysical Research (Atmospheres), 2004, 109, 19106) , the CNES OS code (Lenoble, J.; Herman, M.; Deuzé, J. L.; Lafrance, B.; Santer, R. & Tanré, D. A successive order of scattering code for solving the vector equation of transfer in the earth's atmosphere with aerosols jqsrt, 2007, 107, 479-507) or regarding the Kokanovsky (Kokhanovsky, A. A.; Budak, V. P.; Cornet, C.; Duan, M.; Emde, C.; Katsev, I. L.; Klyukov, D. A.; Korkin, S. V.; C-Labonnote, L. & Mayer, B. Benchmark results in vector atmospheric radiative transfer Journal of Quantitative Spectroscopy and Radiative Transfer, Elsevier, 2010, 111, 1931-1946) benchmarks.

Among the different RTE solvers available in ARTDECO, we use DOAD that is an adding-doubling code based on the method described in de Haan, J. F.; Bosma, P. B. & Hovenier, J. W. The adding method for multiple scattering calculations of polarized light A&A, 1987, 183, 371-391. DOAD is used for the retrieval of "Radiation budget and Cloud" products of PARASOL/POLDER at LOA. It meets all the requirements for the simulation of 3MI data. It handles polarization and accounts for the surface / atmosphere interaction through the definition of bidirectional reflectance.

We use the Delta-M method (The Delta-M Method: Rapid Yet Accurate Radiative Flux Calculations for Strongly Asymmetric Phase Functions. Journal of Atmospheric Sciences, 1977, 34, 1408-1422) for the truncation of the phase matrix. After the RTE solving with DOAD, the radiance is corrected for the first order scattering using the TMS method (Nakajima, T. & Tanaka, M. Algorithms for radiative intensity calculations in moderately thick atmospheres using a truncation approximation jqsrt, 1988, 40, 51-69). An analytical model is used for the single scattering approximation RTE solving. We emphasis the benefits of the TMS at section 3.3.2.

Several ground/surface models are accessible in ARTDECO and we use the Ross-Li BRDF model, which is a linear three parameters model (Lucht, W.; Schaaf, C. B. & Strahler, A. H. An algorithm for the retrieval of albedo from space using semiempirical BRDF models IEEE Transactions on Geoscience and Remote Sensing, 2000, 38, 977-998) for the total radiance, coupled to the Maignan, F.; Breon, F.-M.; Fedele, E. & Bouvier, M. Polarized reflectances of natural surfaces: Spaceborne measurements and analytical modeling Remote Sensing of Environment, 2009, 113, 2642 - 2650 BPDF for the polarized reflectance. For the ocean surface, we use the model developed in the the 6SV tool (Kotchenova, S. Y.; Vermote, E. F.; Matarrese, R. & Klemm Jr., F. J. Validation of a vector version of the 6S radiative transfer code for atmospheric correction of satellite data. Part I: Path radiance ao, 2006, 45, 6762-6774) which consists of a glitter (for the BRDF and BPDF) with the Cox, C. & Munk, W. Measurement of the roughness of the sea surface from photographs of the sun's glitter Journal of the Optical Society of America (1917-1983), 1954, 44, 838 model for the wave slope distribution plus a Lambertian contribution for the foam and an underwater contribution (ocean colour). Note that we use the glitter model from Mishchenko, M. I. & Travis, L. D. Satellite retrieval of aerosol properties over the ocean using polarization as well as intensity of reflected sunlight jgr, 1997, 102, 16989-17014 which is different from the one implemented in 6SV. This glitter model account for the shading.

In ARTDECO, the gas absorption is accounted for by applying the correlated-k technique (see section 3.3.1). We developed a set of specific coefficients for the 3MI bands following Dubuisson et al (2004, 2005). For a given band, the RTE is then solved (eventually several times) for the central wavelength of that band. Hence, variability of the scattering optical properties within the band is not accounted for. We defined the K-distribution coefficients for several gas species that can be used in solving the RTE : H2O, CO2, CO, N2O, O2, O3, CH4. The more we add gas species to the RTE solving, the bigger the computational demand is. We then only use few of these gases for the simulation.

We account for polarization in doing the RT for all 3MI channels, execpt for the 763, 765 and 910 nm channels because it is not measured and has a limited impact on the total radiance.

3.1.3.2 MOMO by FUB

MOMO (Matrix Operator Model: *Fischer and Grassl* 1984, *Fell and Fischer* 2001, *Hollstein and Fischer* 2012, and, *Doppler, Carbajal-Henken et al.* 2014) is the radiative transfer code of the FU Berlin.

The first version of MOMO was built by *Fischer and Grassl* 1984. It uses the Matrix-Operator method (*Plass, Kattawar and Catchings* , 1973). The atmosphere is devided in multiple sublayers, and the reflexion between the layers and the transmission of each layer is described by the operators R (reflexion), and T (transmission). These operators are p*p matrixes (with p is the number of angles for which the radiances are computed). The multiple scattering is described by the reflexion between the millions of sublayers with the operator R and the adding-doubling method. *Fell and Fischer* (2001) recapitulated the principles of adding-doubling in MOMO and proposed a radiative transfer model for the ocean-atmosphere interface, using the statistical approach of *Cox and Munk* (1954). *Hollstein and Fischer* (2012) added the vector radiative transfer to the code, allowing computation of each polarised component. Lastly, *Doppler, Carbajal-Henken et al.* (2014), introduced an operator J_{emis} for the thermal infrared emitted radiation in each sublayers. This has extended MOMO to the longwave. Hence, the spectral interval on which MOMO is valid is [0.2 – 100 µm].

In MOMO the gas transmission is first computed line-by-line with the spectroscopic module CGASA (Coefficients of Gas Absorption: *Doppler, Carbajal-Henken et al.* 2014) and the k-distribution module of the FUB is used, namely the algorithm KISS (k-distribution of Institute for Space Sciences: *Bennartz and Fischer,* 2000; *Doppler, Preusker et al.* 2014). More information about gas transmission, KISS and k-distributions in general can be found in Subsection 3.3.1.

The optical properties of the scatterers (clouds and aerosols) are given in MOMO in their macroscopic form (extinction coefficient, ω_0 – SSA: single scattering albedo – phase function).

If the scatterers are spheric, a module of MOMO named SCA can compute, using a Mie code, these macroscopic properties from the microscopic properties (refraction index, size distribution).

3.2 Input parameters, outputs format, time estimations

3.2.1 Input parameters

The input parameters required for simulation of TOA signals are:

- Geolocation data (observation angular conditions).
- Ancillary datas for each pixel (temperature profile, water vapour and ozone profile, clouds and aerosols masks and profiles , clouds and aerosols optical depths, ground properties: ground albedo/emissivity and reflection properties, temperature - skin and at 2m, pressure, wind speed, water reflectance). These Ancillary data are taken at the time and at the location of the 3 orbits of AVHRR in 2007 and 2008 that are simulated in the 4MSDS project.
- Optical and radiation database with for each channel of each instrument: the cloud and aerosol macroscopic properties for the different cloud and aerosol masks (phase function, extinction coefficient, single scattering albedo), solar irradiance.

The input parameters can be found in 5 different files:

- FAnc: Ancillary data, hdf-5 files for each segment defined in the work package WP1 (around 5 mn of observation). For the instrument METImage (VII), and for the first segment (8:46:02 am) of the third orbit (23th Februar 2008), the file is named: EPS-SG_VII_ANCILLARY_2008-02-23T08-46-02_V01.01.he5
- FWC: Optical properties for Water Clouds, name: opt_liquid_cl_metim.hdf5. For each channel, for 25 different effective radii of the clouds droplets, and 5 different effective radiances (σ), namely for 25*5=125 size distributions.
- FIC : Optical Properties for Cirrus Clouds, name: opt_baum_cirrus_metim.hdf5. For each channel, for 23 different cirrus types.
- Faer: Aerosols. The optical properties of some main aerosols models will be put in an hdf-5 file similar to those of the clouds.
- Fsol: Solar Irradiance. Text document containing the integrated solar irradiance at nadir at the TOA (Top of the Atmosphere). The data for 3MI is named solrad_kdis_game3mi_kurudz_full.dat and for METImage: solrad_kdis_gamemetim_kurudz.dat.

Parameter	**File**	**dataset**	**unit**	**source**
Solar Zenith Angle	Fanc	SZA	Degrees	4MSDS/WP1 geolocation data
Solar Azimuth Angle	Fanc	SAA	Degrees	4MSDS/WP1 geolocation data
View Zenith Angle	Fanc	VZA	Degrees	4MSDS/WP1 geolocation data
View Azimuth Angle	Fanc	VAA	Degrees	4MSDS/WP1 geolocation data
Pressure profile	Fanc	P	HPa	ECMWF
Temp profile	FAnc	T	K	ECMWF
Temp at 2m altitude	FAnc	2T	K	ECMWF

Surface temperature	FAnc	SKT	K	ECMWF
IWVP = Integrated Water Vapor path	FAnc	TCWV	mm	ECMWF
Water Vapour Profile (relative humidity)	FAnc	Humidity_Profile	%	ECMWF
Ozone Profile	Fanc	O3	%	ECMWF
Cloud Mask (type and vertical distribution)	FAnc	cloud_mask, cloud_phase, cloud_type	No unit	AVHRR level 2 data
COD (Cloud Optical Depth)	FAnc	cloud_opd_acha	No unit	AVHRR level 2 data
Cloud particle effective radius	Fanc	cld_reff_dcomp	Microns	AVHRR level 2 data
Cloud Top Altitude	Fanc	cld_heigh_acha	m	AVHRR level 2 data
Aerosol Mask (type)	FAnc	NYA	No unit	Model MACC
Aerosol optical Depth	FAnc	AOD550	No unit	Model MACC
Ground Pressure	FAnc	Surface_Pressure	hpa	ECMWF
Ground Albedo (reflection Li-Ross[1] parameters for visible and nearinfrared)	FAnc	BRDF_Albedo_Parameter X_bandY	No unit	NASA/MODIS
Ground Emissivity (for thermal infrared channels)	FAnc	NYA	No unit	NASA/MODIS
Water reflectance	FAnc	NYA		CCI Ocean Color (in discussion)
IGBP type	Fanc	Majority_Land_Cover_Type	No unit	NASA/MODIS
Surface elevation	Fanc	Elevation	m	National Geophysical Data Center
Liquid clouds optical properties (extinction coefficient, SSA, vector phase function)	FWV	extinction_efficiency, single_scattering_albedo, pxx_phase_function	No unit	Mie computation from microscopic properties.
Ice clouds optical properties (extinction coefficient, SSA, vector phase function)	FIC	extinction_efficiency, single_scattering_albedo, pxx_phase_function	No unit	Fom the databases of Pin Yang and Bryan BA Baum: *Yang et al.* (2005); *Baum et al.* (2011). http://www.ssec.wisc.edu/ice_models/
Aerosol optical properties (extinction coefficient, SSA, vector phase function)	FAer	extinction_efficiency, single_scattering_albedo, pxx_phase_function	No unit	
Solar Irradiance	FSol	(no dataset)	Wm^{-2}	From database of *Kurucz* (1992), available on: http://www.libradtran.org/

Table 3.1: *List of the input parameters, the file in which there are stored, the dataset name for the concerned parameter (in case of dataset file), units of the parameters and the origin of the parameter; NYA= Not Yet Attributed*

[1]*Li-ross parameters (k(λ), k1 and k2; k(λ) is the albedo, k1 and k2 describe the repartition of the reflexion: Lambertian/Specular; see* Maignan, Bréon, Lacaze *(2014).*

3.3 1-D radiative transfer simulations, balance time/precision

3.3.1 Gas transmission, k-distribution

Some channels of 3MI and METImage are centred on some parts of the gas transmission spectra that are very complex (a lot of lines of gas absorption, presence of water vapour or CO_2 continua). Therefore a particular attention has been given to the way to simulate the gas transmission.

In a first step, the gas transmission (t) and optical depth (τ) (associated with the relation $t = \exp(-\tau)$) is computed "line by line" (LBL) for each gas and for each layer of the studied atmospheric profile. The gases taken into account in this project are the water vapour (H_2O), the carbon dioxide (CO_2), the ozone (O_3), the Nitrogen dioxide (N_2O), the carbon monoxide (CO), the methane (CH_4) and the dioxygen (O_2).

The LBL computation consists in computing the gas transmission for each band of both instruments at a very high spectral resolution (0.01 nm for wavelengths below 1 µm and 0.1 nm for wavelengths above 8 µm). These computation leads to a huge number of spectral subintervals (an order of magnitude of 1000 -10000). In the 4MSDS project, we will need to compute thousands of radiative transfer simulations per instrument channels. It is therefore not possible to solve the radiative transfer equation (RTE) on 5000 spectral subintervals per instrument channel. K-distribution methods (*Fou and Liou* 1992, *Lacis and Oinas* 1991) are the best methods used to reduce the simulated spectral subintervals (and in this way the computation time) with the lowest losses of precision. k-distribution methods are used in both models (for ARTDECO: *Dubuisson et al.* 1996, 2005, and for MOMO: *Doppler, Preusker et al.* 2014, *Bennartz and Fischer* 2000).

3.3.1.1 Generalities about k-distribution

The general principle of the k-distribution is to group all the spectral subintervals having similar gas transmission in groups named ***bins*** or ***k-intervals*** (*k* is the gas extinction coefficient), and, to associate a weight (w_i) and an extension coefficient (k_i) to each bin i. Each bin i is therefore described by the 2-elements vector (k_i, w_i). The weight (w_i) of each bin i is proportional to the number of spectral subintervals associated to the bin. The advantage of it, is that the radiative transfer code only needs to solve the RTE on each bin and not on each spectral subintervals. The number of bins is between 1 and 200 in the 4MSDS project, what is much less than the number of spectral subintervals (between 1000 and 10000) required for a line by line approach.

The specificity of the gas absorption spectra of METImage channels and the k-distribution used in MOMO are shown in Subsection 3.3.1.2. The k-distribution used in ARTDECO is presented and validated in Subsection 3.3.1.3.

3.3.1.2 Validation of KISS k-distribution (MOMO for METImage)

K-distribution algorithm KISS

KISS (k-distribution of Institute for Space Sciences) is the k-distribution algorithm of Institute for Space Sciences (ISS) of the FUB. It is the k-distribution algorithm of radiative transfer code

MOMO. KISS has been developed in shortwave (*Bennartz and Fischer* 2000) and extended to thermal infrared (*Doppler, Preusker et al.* 2014).

KISS does not use the correlation approximation. The correlation approximation is the proper of classical k-distribution method (correlated k-distribution method). It consists in assuming that the spectra of all the layers of the atmosphere are correlated. In the correlated method, the k-distribution is therefore defined for a reference layer, in which the bins are defined. Then the extinction coefficient $\boldsymbol{k}$ of each bin is computed for this layers and the other layers. The limit of this method is reached if the spectra of transmission of the atmosphere are "overlapped" namely, if many spectra different from each others (non-correlated) can be found at different layers of the atmosphere. The "non-correlated" method used in KISS does not make this approximation and define a k-distribution that is tested for all the layers of the atmosphere.

The methods (like KISS) that do not use the correlation approximation are:

- Usually defining more bins => increasing of the computation time.
- Usually more precise (because it takes the complexity of the vertical distribution of the gaseous transmission spectrum into account)
- The balance precision/computation time is tuneable with the number of bins that are defined, what is in correlated k-distribution not possible (*West et al.* 2010).

The method used in 4MSDS for METImage is to compute the gas transmission for a 26 levels MSSA (Midlatitude Summer Standard Atmosphere) profile, with the line-by-line spectroscopy code CGASA (Coefficient of gas Absorption) of the MOMO packet (*Doppler, Carbajal et al.* 2014). The information about gas lines of absorption are taken from the HITRAN-2008 database (High Resolution Transmission Molecular Database: *Rothman et al.* 2009). The continuum (foreign and self) computation are following the model MTCKD 2.4 (Mlawer, Tobin, Clough, Kneizys, and, Davies , *Clough et al.* 1989, *Clough et al.* 2005).

Then the bins of the k-distribution are defined with KISS, also only for the 26 layers MSSA profile. The bins coefficients (extinction coefficients k_i) can be extended to other atmospheric profiles with linear (lines of gas absorption, foreign continua of absorptions) or quadratic (self continuum of absorption) laws (*Clough et al.* 1989).

It is crucial to quantify the error due to the use of the k-distribution (which is an approximation) on the TOA (top of atmosphere) radiance.

In this section, we will compare the TOA upward radiance computed with the KISS k-distribution method to the TOA radiance computed with the exact LBL method, for different angles of observation (see figures 3.4 to 3.7). We will first do this comparison for the MSSA (Midlatitute Summer Standard Atmosphere) profile for which we computed the spectroscopy.

Then, in order to validate that we can extend the k-distribution to the computation of other atmospheric profiles, we will compare the TOA upward radiance computed with the KISS k-distributions extended to the dry and cold SWSA (Subarctic Winter Standard Atmosphere) profile and to the wet and warm TRSA (Tropical Standard Atmosphere) profile to the TOA upward radiance computed with the reference and exact line-by-line method for these atmospheric profiles.

Gas spectroscopy and k-distribution spectroscopy for each channel

In the figures shown in this subsection, we will show on the left part of the figures the high resolution spectrum of gas transmission computed with CGASA, for three categories of gases: water vapour (H_2O in blue), ozone (O_3 in red) and mixed gases (CO_2, N_2O, CH_4, CO, O_2 in green).

On the right part of the pictures, we will compare for different angles of observations (OZA) the TOA upward radiance computed with the KISS k-distribution (dots) to the TOA upward radiance computed with the exact LBL method (plain line). For the MSSA profile (blue) and for the extension to SWSA (magenta) and TRSA (yellow).

Figure 3.4: *Gas Transmission spectra and KISS validation for METImage (VII) channels 1 to 5*

Figure 3.5: *Gas Transmission spectra and KISS validation for METImage (VII) channels 6 to 10*

Figure 3.6: *Gas Transmission spectra and KISS validation for METImage (VII) channels 11 to 15.*

Figure 3.7: *Gas Transmission spectra and KISS validation for METImage (VII) channels 16 to 20.*

Discussion of the speed versus precision for each channel

Table 3.2 summarises for each METImage channel, the speed (number of bins defined by the KISS k-distribution) and the precision (Error on the nadir TOA upward radiance for the MSSA profile) of the MOMO computation in the 4MSDS channel.

Chan	0.000	Width (µm)	Nb bins	NREMS*
01	0.443	0.03	2	0.002%
02	0.555	0.02	2	2.248%
03	0.670	0.02	2	-0.001%
04	0.752	0.01	2	0.002%
05	0.763	0.01	15	-1.761%
06	0.865	0.02	2	0.001%
07	0.914	0.02	6	-1.262%
08	1.240	0.02	2	-0.133%
09	1.365	0.04	77	-22.157%
10	1.630	0.02	2	-0.096%
11	2.250	0.05	2	-2.021%
12	3.740	0.18	2	-1.479%
13	3.959	0.04	2	-0.748%
14	4.040	0.06	2	-0.591%
15	6.725	0.37	22	-0.270%
16	7.325	0.29	42	-0.857%
17	8.540	0.29	8	-1.225%
18	10.690	0.5	1	-0.146%
19	12.020	0.5	1	-0.253%
20	13.345	0.31	184	-1.774%

Table 3.2: *Channels of METImage (VII), central wavelengths, spectral width of the channel, number of bins (k-intervals) defined by the k-distribution KISS algorithm and on which the MOMO computation will be done, and, *NREMS = Nadir TOA (Top of Atmosphere) Upward Radiance Error for the Midlatitude Summer Standard Atmosphere : Error in percent due to the use of the k-distribution method.*

Note, the central wavelength of some channels (4, 9, 13, 14) have been slightly changed, the changes do not change a lot the bins' estimation. Nevertheless, for the *final computing phase of the study, the computations will be done for the updated channels' position.*

Specific discussion for relevant channels:

Channel 5: The gas transmission is difficult to model for this channel, because there are a lot of very narrow O_2 absorption lines (O_2-A band). This channel is used for the cloud-top height estimation. This complex spectrum (see Figure 3.4, bottom,left) is the reason why we need 15 bins (a lot for such a narrow channel) for the computation. The precision is not the best one of this study but is acceptable (below 2%, see Table 3.2) and Figure 3.4 (bottom, right) shows that the extension to other atmospheric profile is not a problem.

Channel 9: This is a water-vapour channel (see Figure 3.5, first line of pictures). The transmission of this channel depends a lot on the IWVP (Integrated Water Vapour Path = water column in mm), thus on the kind of atmospheric profile (MSSA, TRSA or SWSA). The gas transmission in this kind of channel is difficult to simulate with the k-distribution, this is the reason why KISS needs to define 77 bins (see Table 3.2). The error on the TOA radiance (above 20% as shown in Table 3.2) is to be relativised. This big amount in percent is due to the fact that the values of the radiance are very low (of the order of 0.8: see Figure 3.5). For simulations of this channel with a profile with a larger transmission, because of smaller water vapour amount, like the SWSA profile, we have the same absolute error, and thus, because the values of the radiance are much larger, a smaller relative error (-1.061 %), as shown in purple on the right part of the graph of Figure 3.5.

Channel 15: In this channel, we observe an absorption due to an O_2 continuum (see in green on the right graph of Figure 3.6). The weak lines that we observe, are CO_2 absorption lines. To model this particularity, KISS needs to define 22 bins, but permits to model the TOA radiance with a good precision (see Table 3.2 and Figure 3.6, bottom/right), what is a good illustration of the performances of k-distribution without correlation approximation: The balance precision/rapidity is tuneable by changing the number of bins.

Channel 16: The gas transmission spectrum is very complex (see Figure 3.7, top/left). There are water vapour lines and continuum of absorption (in blue on the figure), and, some absorption lines of CH_4 and N_2O. This explains why KISS defines a large number of bins (42, see Table 3.2) for the simulation of this channel. With this large number of bins, the simulation is precise (see Table 3.2 and Figure 3.7, top/right)

Channel 20: This channel has a double difficulty: As Figure 3.7 (bottom/left) shows, the gas transmission spectrum is very complicated, with ozone lines (in red), CO_2 lines and continuum (in green), and water vapour lines and continuum (in blue). The second difficulty is that at this wavelength, the blackbody radiation, governed by the Planck Law, reach large values for the atmospheric temperature. The k-distribution algorithm needs to take all that into account, and this is the reason why, KISS defines a very large number of bins (184, see Table 3.2). The precision for the MSSA profile is below 2% what is a success of the k-distribution. The extension to other profiles is slightly less precise (between 4 and 5 % as we see on Figure 3.7, bottom/right), but still acceptable.

3.3.1.3 Validation of the correlated k-distribution (ARTDECO for 3MI)

Correlated k-distribution method used in ARTDECO

Gaseous absorption (mainly H_2O, CO_2, O_3, N_2O, CO, CH_4 and N_2) is calculated using the correlated k-distribution, following *Lacis and Oinas* (1991). Considering a layer at pressure *P* and temperature *T*, the gaseous transmission function for a spectral interval depends on T, P and on the amount u_j of each of the here above cited components.

This transmission function can be accurately calculated from a line-by-line code. In the ARTDECO (Atmospheric Radiative Transfer Database for Earth Climate Observation) approach, LBLDOM (Line-byLine radiative transfer with Discrete Ordinate Method) line-by-line code (*Dubuisson et al* , 1996, 2005) is used. As cited in Subsection 3.3.1.1 an approach using a line-by-line code leads to very important computational times.

This transmission is then approximated by an exponential summation over a limited number *N* of absorption classes (bins), like in the KISS k-distribution. Each term of the series has a weight w_i (represents the probability) associated to the mean absorption coefficient $k_{i,}$ for each absorption class *i*. The coefficients of the exponential series (w_i and k_i) are determined from reference calculations from the LBLDOM code, using the spectroscopic database HITRAN (*Rothman et al.,* 2009). Indeed, the coefficients w_i and k_i are calculated for a set of reference pressures *P* and temperatures *T* with the LBLDOM code. For a given atmospheric profile, these coefficients are then estimated using non-linear interpolations. Note that the correlated k-distribution technique allows accounting for interaction between gaseous absorption and multiple scattering with manageable computational time. In addition, the impact of the absorption continua is modelled using the CKD formulation (*Clough et al.,* 1989).

In practice, the number of coefficient *N* is generally between 3 and 15 as a function of the considered absorbers and the spectral interval. In the case of overlapping absorption coefficients, the transmission can be calculated from the k-distribution defined for each gas species. As an example, in the case of two absorbers 1 with N bins *i* and 2 with M bins *j*, with an amount of u1 and u2 respectively:

$$t(u_{1,}u_2)=\sum_{i=1}^{N}[w_i\cdot\exp(-k_i\cdot u_1)\times(\sum_{j=1}^{M}w_j\cdot\exp(-k_j\cdot u_2))]$$

This approach is not rigorous but it leads to fast and accurate calculation of gaseous absorption over large spectral intervals (see the following subsection). In this case, the number of radiative transfer calculations, for example performed with the Discrete Ordinates Method (DISORT; *Stamnes et al.,* 1988), is N * M, which represents the number of radiative transfer equations to be solved.
Note, that dissociating the transmission of each component reduce the error due to the correlation approximation, because even if it is rarely the case that 2 spectra of 2 different components are correlated, for the same component, the spectrum at different layer of the atmosphere is very often correlated, and depends only on the pressure (*P*) and temperature (*T*). Therefore, in the correlated k-distribution method used for 3MI, there are these interpolations on *P* and *T*.

In order to optimise the computational time, the number *N* of bins in the k-distribution has been defined in each spectral interval as a function of the absorption level (Table 3.3). Indeed, this computational time is proportional to the number of bins. As an example, it is not necessary to use an important number of bins for spectral intervals with a weak gaseous absorption. The spectral interval is defined as non-absorbing if the transmission is higher than 0.9999.

	N
TRS > 0.999	1
0.999 > TRS > 0.99	3
0.99 > TRS > 0.95	5
0.95 > TRS > 0.8	10
0.8 > TRS > 0.1	15
0.1 > TRS	10

Table 3.3: *Number N of bins for the k-distribution as a function of the transmission TRS of a tropical atmosphere with an air mass of 6.*

K-distribution coefficient were computed for H_2O, CO_2, CO, N_2O, O_2, O_3, CH_4.and for spectral intervals corresponding to the METimage and 3MI instrumental response function. We note however that only H_2O, O_3 and O_2 were accounted for in radiance computation for the VIS/SWIR range. Ozone absorption is accounted for in all bands because it is broad band absorption and does not require the use of multiple k-bins to be accounted for. H_2O and O_2 line absorption are accounted for (using k-distribution parametrization) in bands listed in Table 3.4.

Accuracy of the Correlated-k distribution method used in ARTDECO

The accuracy of the correlated k-distribution is reported here for each used gases in corresponding channels in Table 3.4. The error on the atmospheric transmission is obtained by comparison too the line by line model LBLDOM.

3MI				
Filter	Gas	N_{KI}	LBL trans	K-dis. error (%)
763	O2	15	0.393	0.5
765	O2	10	0.841	0.4
910	H2O	15	0.336	0.3
1370	H2O	10	0.000	11.5
METimage				
Filter	Gas	N_{KI}	LBL trans	K-dis. Error (%)
763	O2	15	0.393	0.5
914	H2O	15	0.359	0.2
1365	H2O	10	0.000	10.4

Table 3.4: For instrument channels affected by lines absorption, list of the considered gases together with the error on transmission due to k-distribution parametrization.

The line by line transmission is given for an air mass of 6 through a standard US62 atmosphere.
The error due to parametrising the absorption with a correlated K-distribution is below 1% for all channels except for the 3MI-1370 and VII-1365 for which the transmission is close to 0.0.

3.3.2 Speed/Precision Trade-off considerations

In 1-D radiative transfer codes like MOMO and ARTDECO, the user must make some critical choices in order to favour the precision in detriment of the rapidity or vice versa. These choices are the increasing/decreasing of the number of bins of the k-distribution, the increasing/decreasing of the number of Fourrier terms, the increasing/decreasing of the number of angles or streams that are computed, and, the increasing/decreasing of the number of atmospheric layers in which the modelled atmosphere is divided.

The loss o time due to the increasing of these numbers follows linear or quadratic laws that depend on the method used. In the next paragraph, we explain how the computation time is influenced for MOMO and for ARTDECO by the increasing of these numbers. And we explain the choices made for each radiative transfer code for the 4MSDS project.

MOMO:

- Fourrier term: linear -> if factor α in the amount of Fourrier term, computation time = α*(original computation time)
- Number of layers computed: : linear -> if factor α in the amount of vertical layers, computation time = α*(original computation time)
- Angles/Streams (SZA, OZA): quadratic -> if factor α in the amount of angles computed, computation time = α^2*(original computation time)

- Bins (k-intervals: k or λ subintervals): linear → if factor α in the amount of angles computed, computation time = α^2*(original computation time)

Thus, after tests in MOMO, we decide to work with 10 Fourier terms and 20 angles in visible and near infrared (until 2200 nm: channels 1 to 11), with 10 Fourier terms and 30 angles for the channels 12 and to 14 (3500 – 4200 nm), and with 1 Fourier term and 5 angles for the thermal infrared channels (15 to 20: from 8 to 13.5 µm).

ARTDECO: We present here the benefits of the TMS (single scattering) correction. The TMS roughly consist in two steps:

1. subtracting the first order of scattering from the result obtained with the RTE solver by approximating the phase matrix with a truncation and Legendre polynomial expansion.
2. add back this first order of scattering using an analytical (exact) formulation. For the phase matrix.

Figure 3.8 shows the TOA radiances obtained for 10 computational angles with and without TMS correction. The modelled scene is the Kokhanovsky benchmark (Figure 3.9) scene for cloud. The cloud is purely scattering with an optical thickness of 5.0. the surface is black and there is no Rayleigh scattering. The solar zenith angle is 60 degrees. The cloud phase matrix is truncated with the delta-M method. We clearly see that the result is dramatically changed when applying the TMS. We note that this correction has nearly no CPU cost. The TMS allows to reduce the number of computational angles. It is of great interest considering that the CPU time in DOAD varies more that quadratically with the number of computational angles (x 2 number of angles results in x 7 CPU time, x 4 number of angles results in x 32 CPU time). Finally, we note that after TMS correction, the radiance computed are within 4% of the benchmark values for most geometries (except for values close to 0). The error can be higher (up to 6% for the rainbow and up to 10-15% for polarized radiance for backward scattering) for particular geometries such has rainbow or backward scattering. We emphasis that we always apply the TMS correction in the LOA simulator.

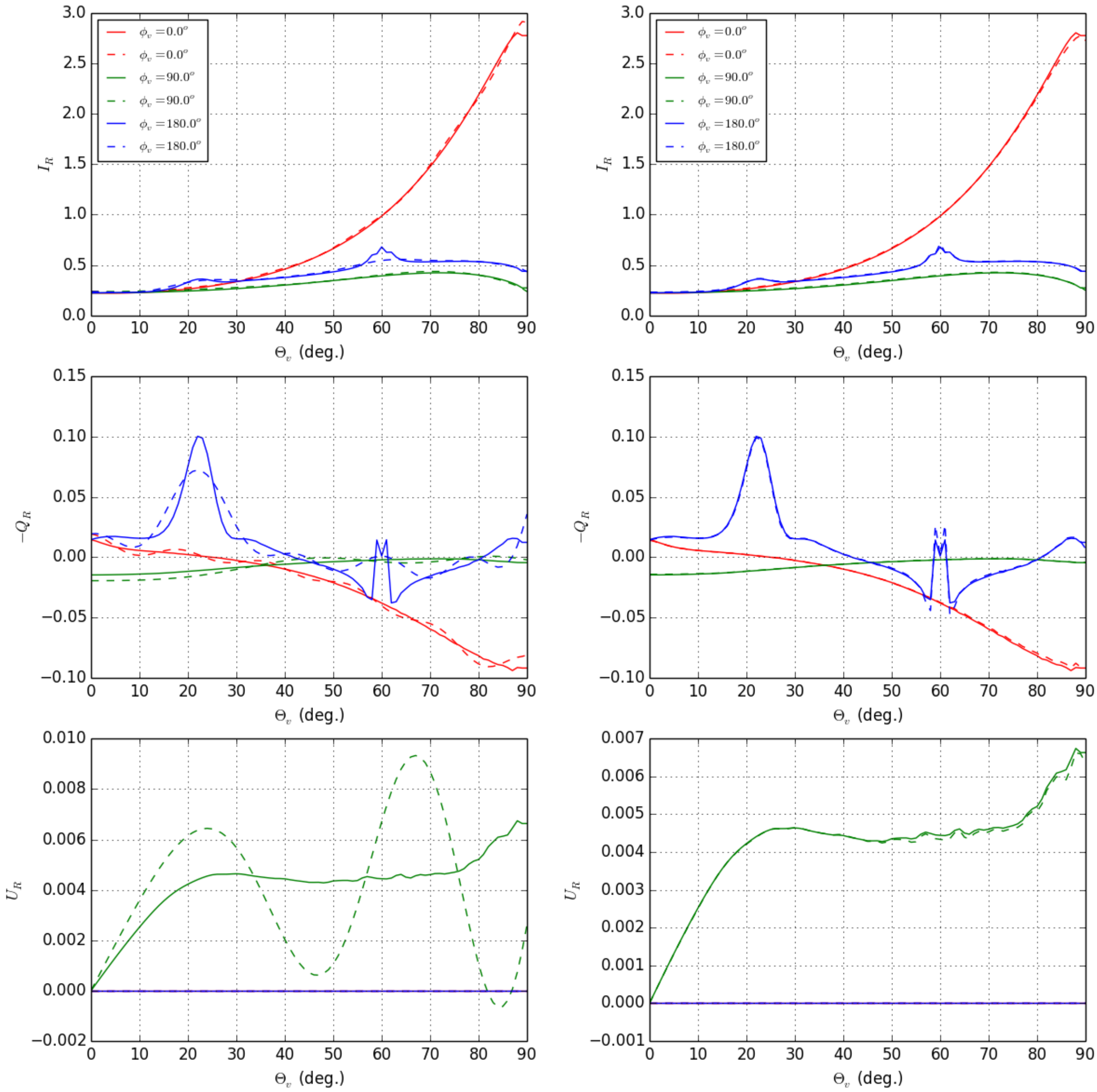

Figure 3.8: *Illustration of the TMS benefits on the Kokhanovsky benchmark test for cloud scene. The line is the reference benchmark result while the dashed line is the ARTDECO output. The two panels show the three first Stokes parameters for the TOA. The result is a function of the viewing zenith angle. Red, green and blue lines are for relative azimuthal angles of 0, 90 and 180 degrees. The left panel shows the results without TMS correction. The right panel show result with TMS correction.*

3.3.3 Cross Validation and Inter Comparison of Scattering and Surface Reflection

The radiative transfer code MOMO is used for the simulation of all METimage channels and the ARTDECO is used for the simulation of all 3MI channels. Both radiative transfer models

have been described extensively in the literature and a short overview has also been given in Subsection 3.1.3. Due to their different areas of application in the past, different design choices have been driven in the development of both models such that a model inter-comparison before starting the simulations seemed feasible.
Within the framework of this project, both radiative transfer models use RTE solvers based on the doubling adding method (see *De Haan* 1987 for ARTDECO, *Doppler, Carbajal et al.* 2014, *Hollstein and Fischer* 2012, and, *Fell and Fischer* 2001 for MOMO) with the main difference between the two models being that MOMO is a fully coupled atmosphere ocean model.

A basic set of comprehensive test cases was defined for the inter comparison of both models and an overview is given in Table 3.1. The test cases can be split up in two groups, with the first group being an independent model validation for aerosol and cloud scattering and the second group being a set of test cases which were selected to iteratively compare the scattering and reflection physics implementation in both models.

The radiative transfer simulation published in *Kokhanovsky* (2010) were used as a first test to compare the simulation of both models with an independent source. The used phase matrices are shown in Figure 3.9 and an inter comparison of MOMO and ARTDECO results is shown in Figure 3.10. Before discussing the results, we want to highlight that these two cases are actual quite hard problems for radiative transfer models. The phase functions (the 1,1 element of the phase matrices) are strongly peaked and the simulation result is dominated by the treatment of multi scattering. For various model to converge at the same result it is necessary to apply highest resolution settings for each model. Here, the angular resolution and the number of Fourier terms must be chosen quite high to reproduce the published results. For mass production of radiative transfer simulations one might settle for lower resolution settings to compromise with the limited computation time and resources.

Shown in Figure 3.10 are MOMO results and ARTDECO results with respect to viewing zenith angle, relative azimuth angle (colours) and Stokes parameters I,Q, and U. The simulations were not tuned to reproduce the exact same numbers but nevertheless show very good agreement with each other. Even better agreement could be reached if both model background parameters such as the phase function truncation method, the angular resolution, and the number of Fourier terms. While this would give much smaller residuals, this would yield no additional insight. From the shown results we can conclude that both models are very well able to reproduce the selected independent results which selectively test the implementation of scattering. The main goal of this test was to verify our understanding of the used units and the meaning of the viewing geometry in both models.

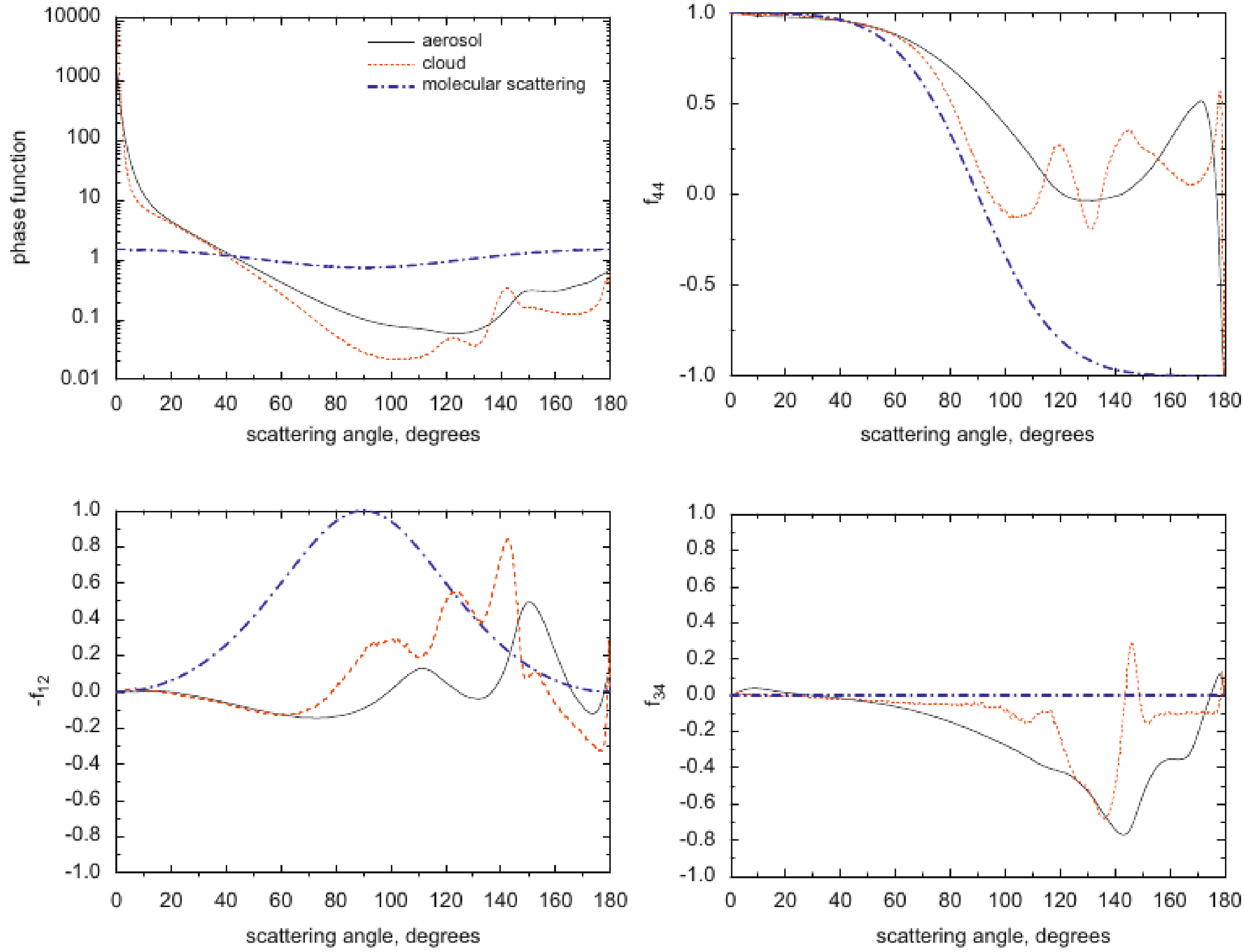

***Figure 3.9:** Aerosol and cloud phase matrices which were used for the inter-comparison cases bench_cld_5 and bench_cld_20 as defined in Table 3.1. (Figure reproduced from* Kokhanovsky *(2010))*

independent model validation cases based on Kokhanovsky (2010)	
bench_cld_5	single layer scattering with the cloud phase function given by Kokhanovsky (2010), optical thickness is set to 5, relative azimuth angle 0°, 90°, 180°, solar zenith angle 60°
bench_cld_20	same as bench_cld_5, but with an optical thickness of 20
model inter comparisons for the inter comparison of scattering and surface reflection	
mdl_1	Lambertian surface reflection of 0.0, Rayleigh optical thickness of 0.1
mdl_2	Lambertian surface reflection of 0.5, Rayleigh optical thickness of 0.1
mdl_3	rough ocean surface, wind speed = 2.0 m/s, refractive index nr =1.344
mdl_4	rough ocean surface, wind speed = 7.0 m/s, refractive index nr =1.344
mdl_5	rough ocean surface, wind speed = 2.0 m/s, refractive index nr =1.344, under surface reflectance albedo = 0.2
mdl_6	rough ocean surface, wind speed = 7.0 m/s, refractive index nr =1.344, under surface reflectance albedo = 0.2
mdl_7	rough ocean surface, wind speed = 2.0 m/s, refractive index nr =1.344, under surface reflectance albedo = 0.2, Rayleigh optical thickness of 0.1
mdl_8	rough ocean surface, wind speed = 7.0 m/s, refractive index nr =1.344, under surface reflectance albedo = 0.2, Rayleigh optical thickness of 0.1
mdl_9	Li-Ross surface BPRDF model with k_lambda=0.04, k2=0.045342, k1=0.016312 and Maignan model with Cv=5.0, nr=1.5, ni=0.0

Table 3.5: *List of selected cases for the inter-comparison of the MOMO and ARTDECO radiative transfer models.*

Figure 3.10: *Inter-comparison of ARTDECO and MOMO results for the bench_cld_5 and bench_cld_5 case as defined in Table 3.1.*

The second group of test scenarios was selected to iteratively test the implemented physics in both models and to systematically study eventual differences for both model results. The rationale behind the scenario mdl_1 to mdl_9 can be understood in the following way: With mdl_1 we test only Rayleigh scattering which is used to model molecular scattering. In the second step with mdl_2, we add a Lambertian surface and additionally test for surface reflection. With scenario mdl_3 we change the focus to the rough ocean surface which is tested for a small wind speed which leads to a small sun glint. In this test case no Rayleigh scattering is considered. In the next step with scenario mld_4 we increase the wind speed which results in a much wider and less strongly peaked sun glint. With scenario mdl_5 and mdl_6 we repeat the exercise from before but additional consider a subsurface albedo of 0.2. With scenario mdl_7 and mdl_8 we again repeat the exercise but additionally consider a Rayleigh optical thickness of 0.2. Following this path we started from a simple and artificial simulation and increased the complexity to end at a realistic simulation for an ocean case. This way we can test the physics behind the following simulations independently. The last simulation mdl_9 tests our understanding of the BPRDF model with a realistic set of parameters.

For this set of simulations we changed the solar zenith angle to 40°, which allows much better to compare the directional features in the sun glint region and the BPRDF reflectance. An overview about the model simulations for reflectance and the cases which were defined in Table 3.1 is shown in Figure 3.11 . In general, the figure shows that both models very well agree with each other. Main differences originate in differences in the angular resolution of the simulations. Small systematic differences can be seen in the simulations with ocean and prescribed ocean albedo. These can be explained by the quite different treatment of the ocean within both models. The MOMO model is a fully coupled atmosphere ocean model while the ARTDECO model uses a prescribed ocean albedo to account for the oceanic contribution to the top of atmosphere reflectance. To achieve consistency between the to be simulated data sets, we changed the implementation of the oceanic contributions in MOMO to a similar approach.

Figure 3.11*: Inter-comparison of MOMO and ARTDECO simulations for reflectance and the test cases which were described in Table 3.1.*

A more detailed inter-comparison with respect to polarization is shown in Figure 3.12 to Figure 3.14. As in the comparison for radiance only, both models show very good agreement, with minor differences only for the cases with ocean subsurface albedo. This was expected and was discussed in a previous passage. Since the agreement is very good we proceed without further discussion of the results and consider Figure 3.12 to Figure 3.14 as reference for this statement.

***Figure 3.12**: Inter-comparison of MOMO and ARTDECO simulations for Stokes parameters I,Q, and U for the test cases 1-3 which were described in Table 3.1. This overview is continued in Figure 3.13 and Figure 3.14.*

Figure 3.13: *Inter-comparison of MOMO and ARTDECO simulations for Stokes parameters I,Q, and U for the test cases 4-6 which were described in Table 3.1. Other cases are shown in Figure 3.12 and Figure 3.14.*

***Figure 3.14**: Inter-comparison of MOMO and ARTDECO simulations for Stokes parameters I,Q, and U for the test cases 4-6 which were described in Table 3.1. Other cases are shown in Figure 3.12 and Figure 3.13.*

3.4 Example simulations

3.4.1 Example simulations for 3MI

For the LOA simulator, example simulations are presented here for a sample granule. Note that we present here the final simulation setup that includes all details of atmospheric and surface properties as opposed to preliminary simulation that had been performed to illustrate simulator setup during performance of task 2. The polarization is accounted for all bands but the 910 nm. In the following we show the resulting TOA radiances (and polarized radiances) for a selected set of bands and sequences (among the 14 sequences per VIS detector and 28 sequences per SWIR detector). We also show the histogram of radiances. Both aerosols and clouds (varying effective radius, altitude and water phase following the AVHRR product) are accounted for and the ground is properly treated (BRDF for either the ocean and land). Atmospheric profiles are adjusted with respect to meteorological conditions obtained from ancillary data. We consider O3 absorption in all bands, plus H2O in 910 and 1370 nm bands.

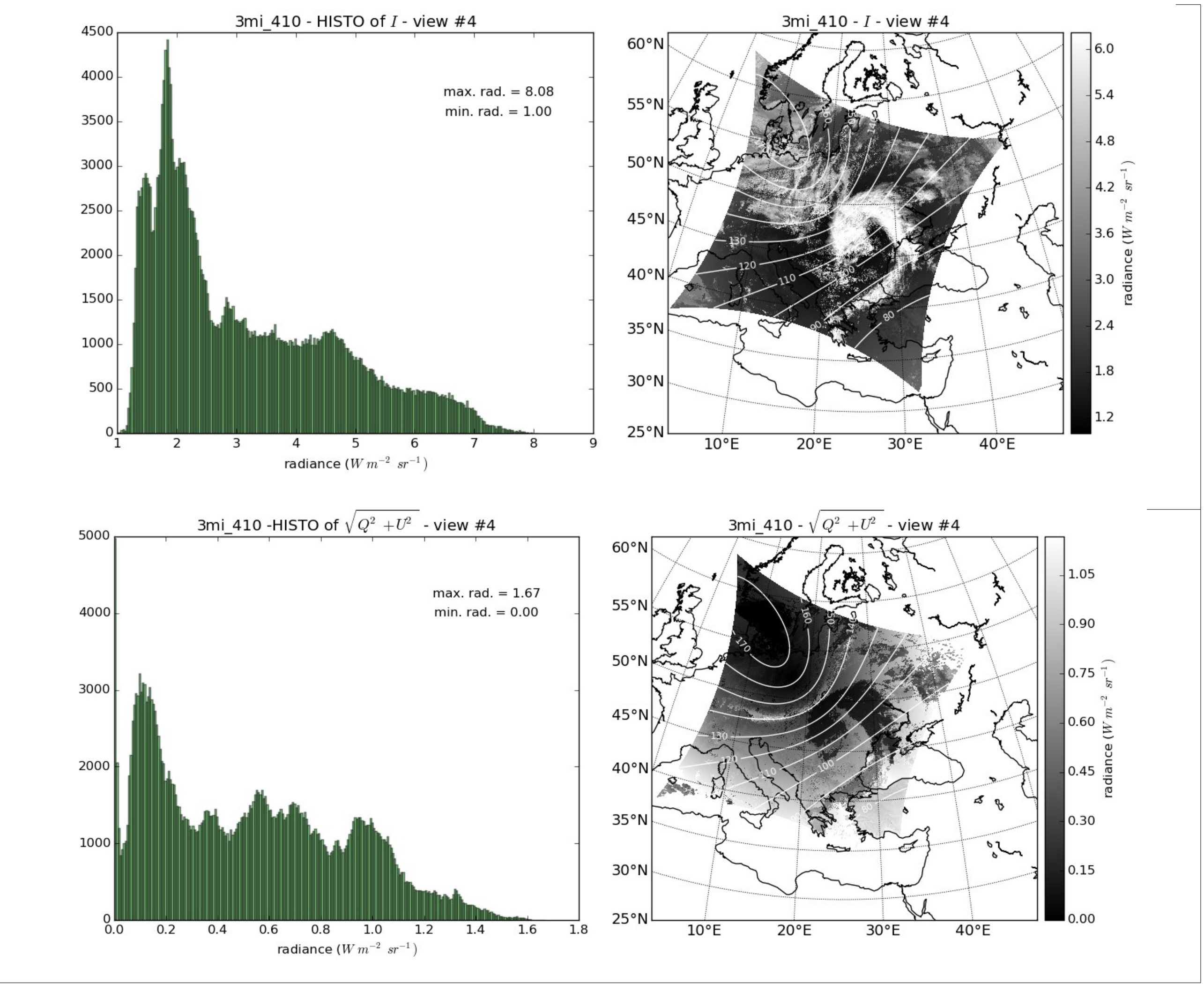

Figure 3.15: *3MI 410 nm band simulated radiances. Right panels present the mapped 512x512 detector matrix for the granule viewing sequence #4 and corresponding histograms are plotted on the left. Upper and lower panels present respectively the total and polarized radiances.*

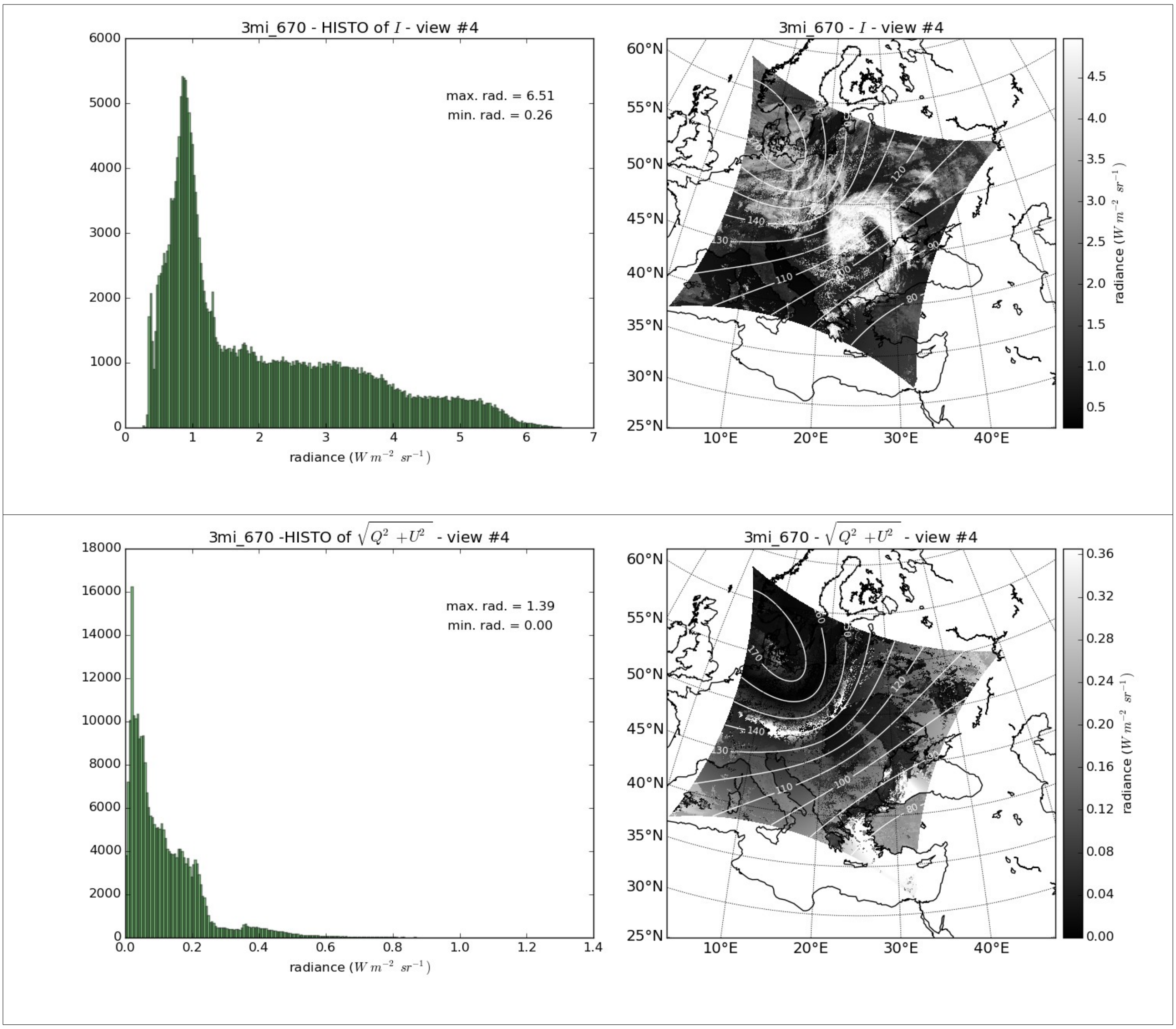

Figure 3.16*: 3MI 670 nm band simulated radiances. The right panel is the projection of the 512x512 detector matrix for the viewing sequence #4 of the granule. The left panel is the corresponding histogram. The upper panel is for total radiance while the lower one is for polarized radiance.*

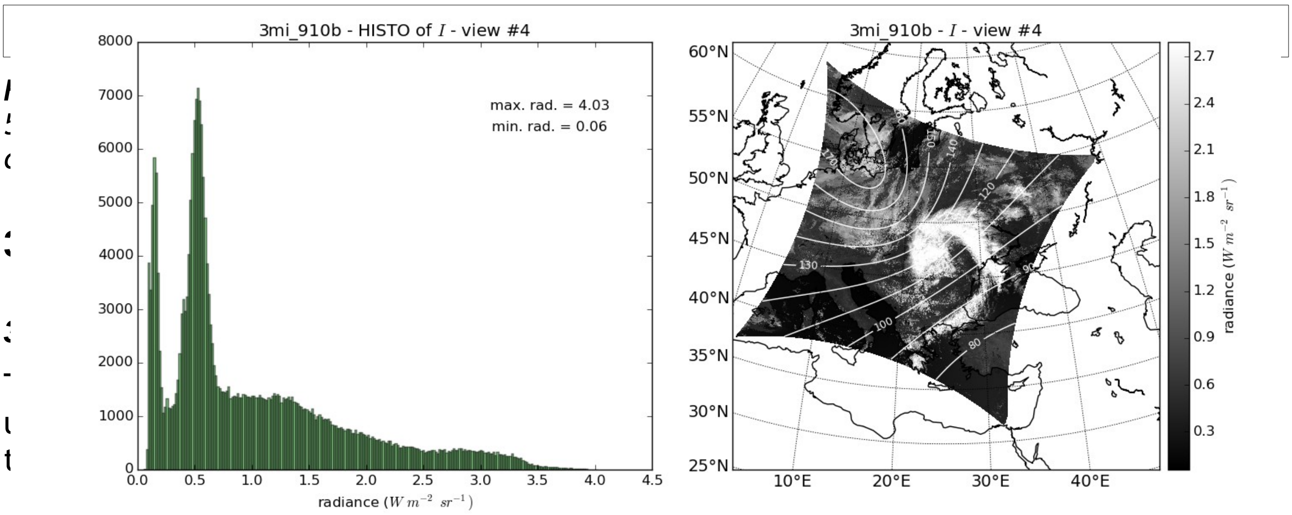

parameters required for realistic simulation of the VII observations. Therefore it was decided at a later stage to rely on direct computation from ARTDECO to simulate all VIS, NIR and SWIR channels from VII while the thermal infrared channels have been simulated using LUT precomputed with MOMO.

3.4.2.2 Example of VII simulated radiances and corresponding AVHRR observations

Example simulation for VII are presented in section 5.1 but we provide hereafter an example of full resolution VII simulated data along with corresponding AVHRR observations that have been remapped to the VII instrument geometry. As VII and AVHRR ISRF central wavelength and FWHM are not exactly similar, differences are not unexpected. For the infrared channels the use of the LUT approach for simulation also implies that discrete values were taken for atmospheric and cloud parameters which can result in the more or less pronounced peak seen in the radiance histograms between the observed and simulated data. Finally one need to bear in mind that cloud properties were obtained from retrieved properties which also induce some significant level of uncertainty in cloud altitude and emissivity. Because the same assumption are not made during retrieval stage (AVHRR cloud products) and the simulation stage (this study) this inevitably results in differences between the observed and simulated radiances. However we can still note the general very good coherence of simulated data against their corresponding AVHRR observations.

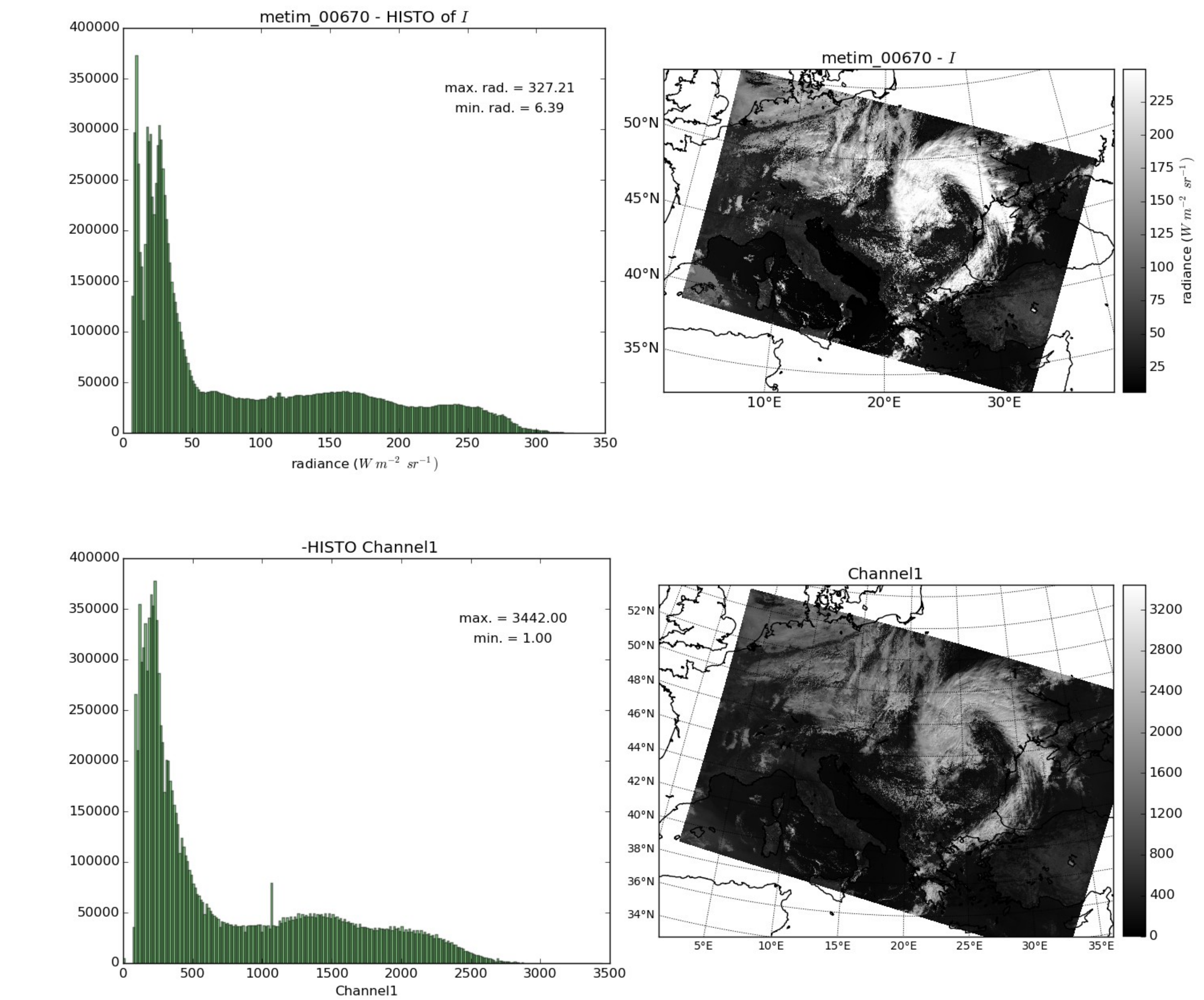

Figure 3.18: *Example of full resolution VII 670 nm channel simulation (top) for granule 2007-09-12T08-43-03 and comparison with AVHRR Channel 1 (bottom) observed radiance remapped to the same geometry (AVHRR data are radiances x 1000).*

AVHRR Channel 1 observations agree extremely well with simulated 670 nm VII radiances both in terms of cloud features distributions and in terms of histograms.

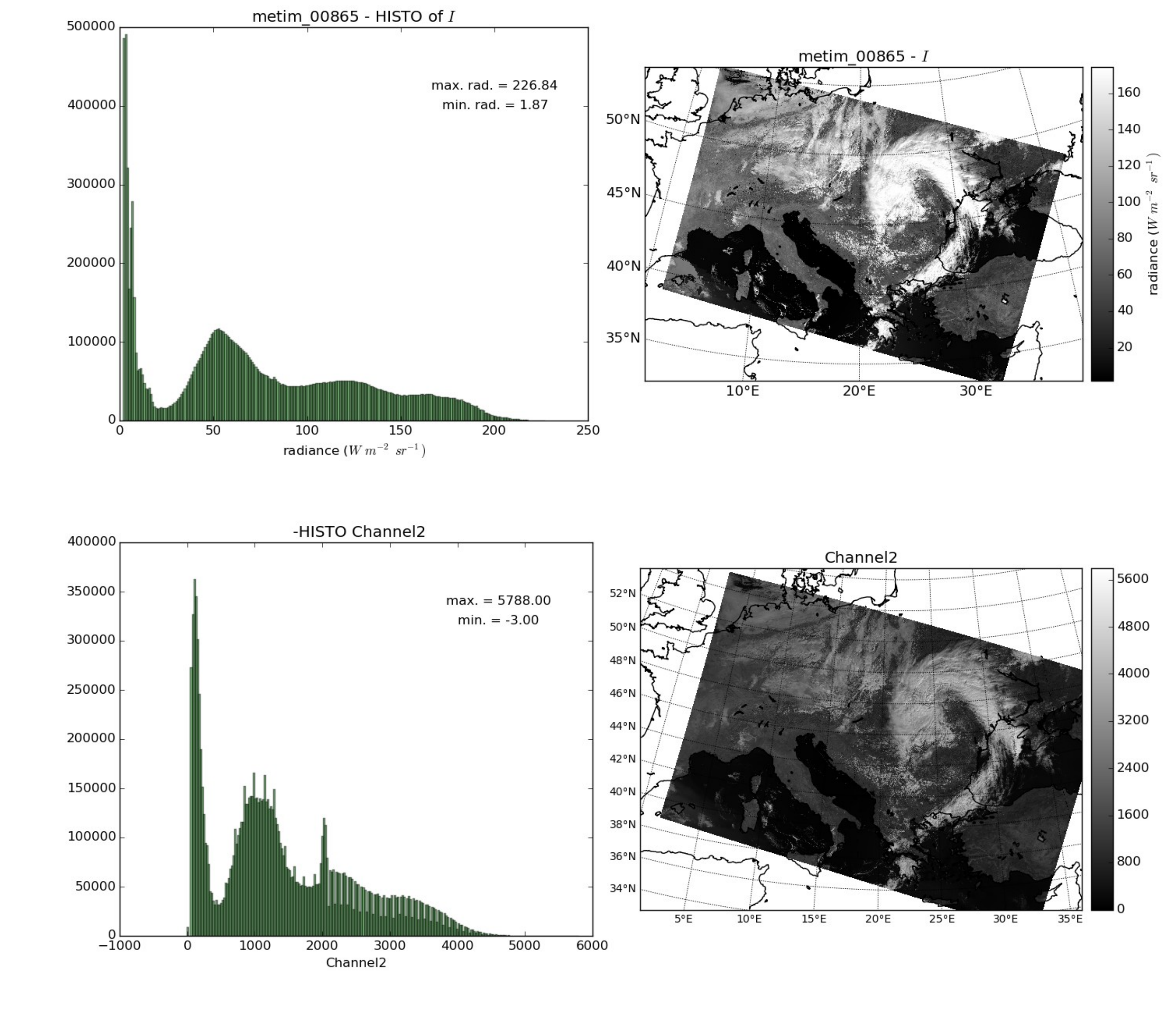

Figure 3.19: *Example of full resolution VII 865 nm channel simulation (top) for granule 2007-09-12T08-43-03 and comparison with AVHRR Channel 2 (bottom) observed radiance remapped to the same geometry (AVHRR data are radiances x 1000).*

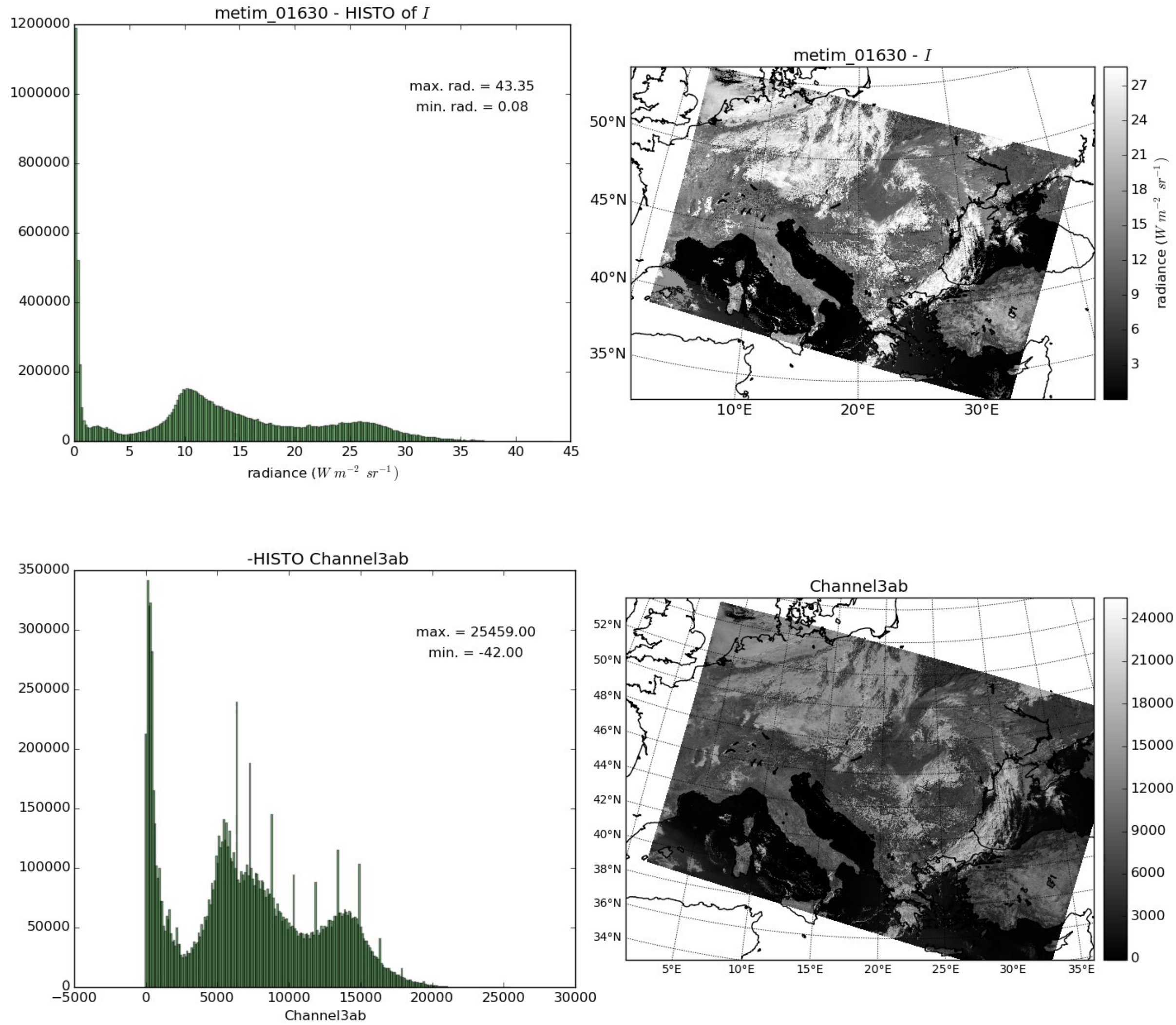

Figure 3.20: *Example of full resolution VII 1650 nm channel simulation (top) for granule 2007-09-12T08-43-03 and comparison with AVHRR Channel 3a (bottom) observed radiance remapped to the same geometry (AVHRR data are radiances x 1000).*

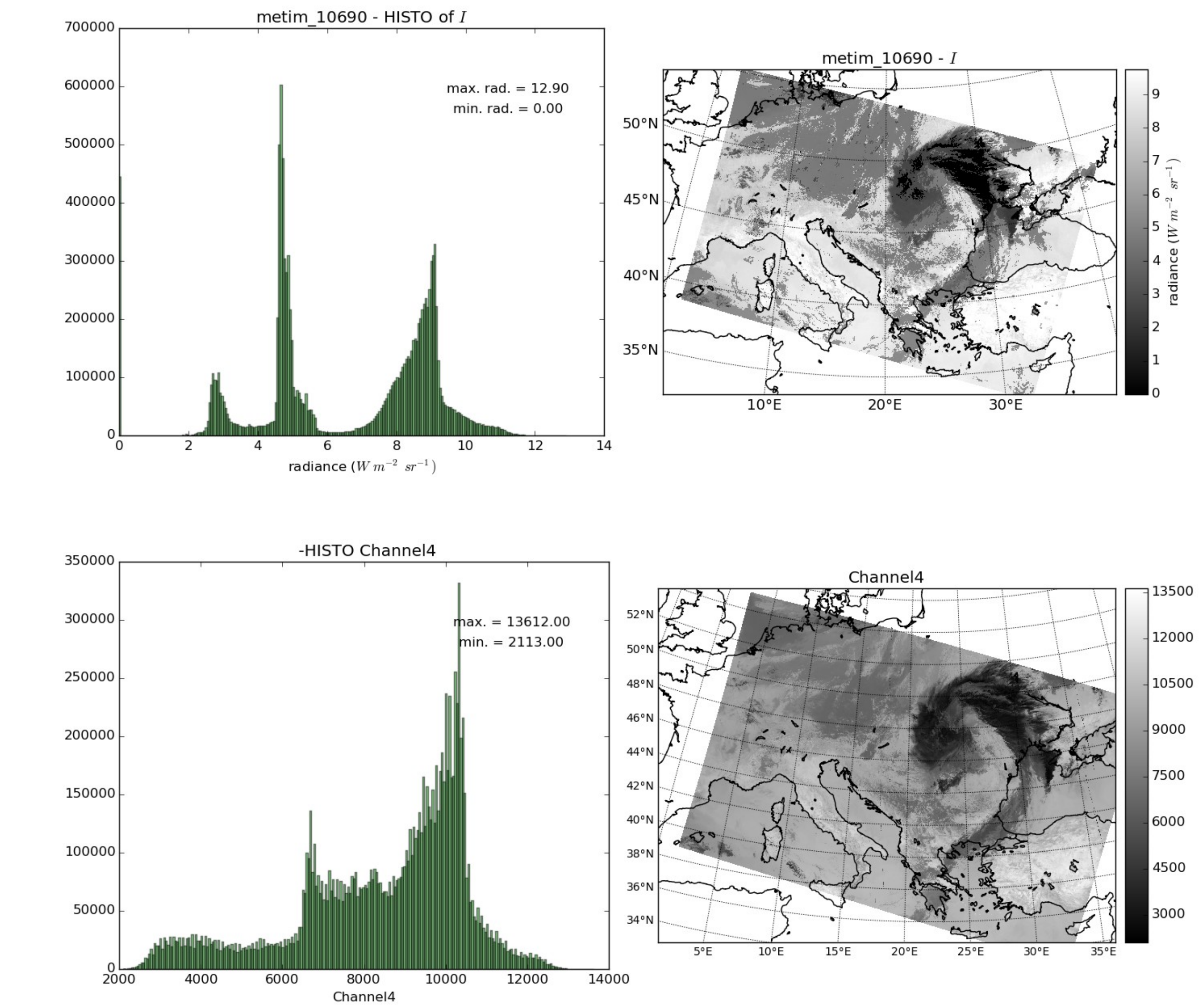

Figure 3.21: *Example of full resolution VII 10.690 micrometers channel simulation (top) for granule 2007-09-12T08-43-03 and comparison with AVHRR Channel 5 (bottom) observed radiance remapped to the same geometry (AVHRR data are radiances x 1000).*

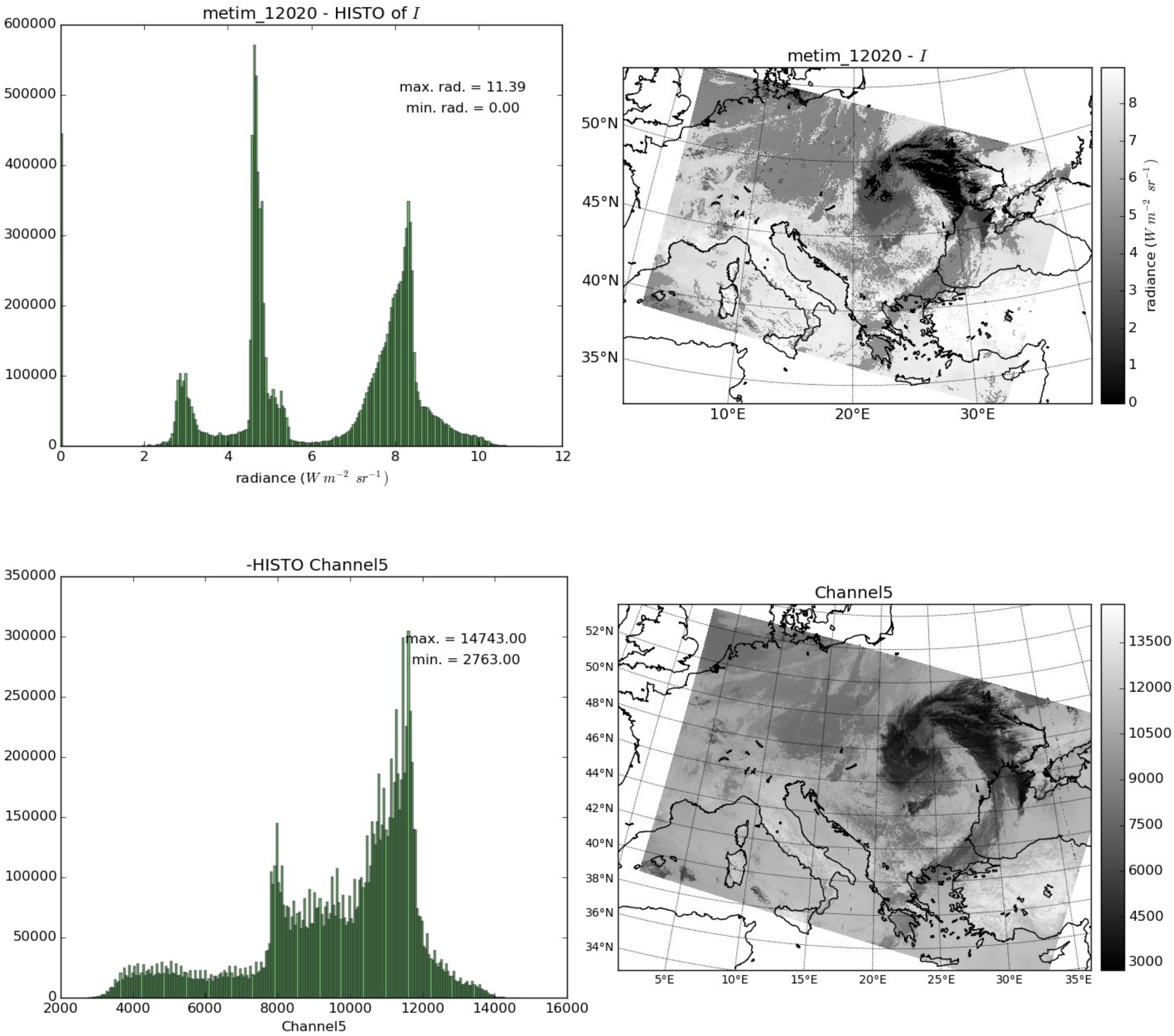

Figure 3.22*: Example of full resolution VII 12.020 micrometers channel simulation (top) for granule 2007-09-12T08-43-03 and comparison with AVHRR Channel 5 (bottom) observed radiance remapped to the same geometry (AVHRR data are radiances x 1000).*

Similarly to AVHRR visible Channel 1, the infrared window channels 4 and 5 of the AVHRR show good agreement with the simulated VII data. However due to the discrete values of input parameters used for the LUT approach the histograms of simulated radiances tend to exhibit more pronounced "peak" features, although the dynamic range is well reproduced.

4 Ancillary data for Simulation of 3MI and METImage (VII)

This section describes the ancillary data produced as part of Work Package 3 of 4MSDS to support simulation of 3MI and VII synthetic observations.

– In Section 4.1, we recall the list of parameters required as input to the two simulators and identify the source of data that have been used
– In Section 4.2, we describe in further details some of the assumption made to provide practical inputs to the simulator from the parameters provided in the ancillary files.
– In Section 4.3, we describe the approach taken to facilitate the use of ancillary data along with the geolocation and observation geometries files established in WP1 and provide a description of the content and format of the ancillary files.
– A delivery note containing the list of ancillary files for 3MI and VII is appended to this report

The output of WP3 consisting of ancillary data files supporting the simulation of test data can be obtained through the following ftp server at :

For the VII: ftp://ftp.icare.univ-lille1.fr/dev_ftp/4MSDS/VII/

For the 3MI : ftp://ftp.icare.univ-lille1.fr/dev_ftp/4MSDS/3MI/

In addition to this document, an online technical documentation of the ancillary files format and content is available at :

http://www.icare.univ-lille1.fr/dev/4MSDS/index.php

4.1 Input parameters and sources of ancillary data

4.1.1 Input parameters

The input parameters required for the simulation of signal and already identified in WP2 report are :

- Scene geometry : solar zenith and azimuth angles, view zenith and azimuth angles.
- Ancillary data for each pixel (temperature profile, water vapour profile and column amount, clouds and aerosols masks and profiles, clouds and aerosols optical depths, ground properties: ground albedo/emissivity and reflection properties, temperature - skin and at 2m, pressure, wind speed, water reflectance). These Ancillary data are taken at the time and location of the 3 orbits of AVHRR in 2007 and 2008 that are simulated in the 4MSDS project. The list and description of parameters is provided in Table 4.1 page 120.
- Optical properties and radiation database providing for each channel of each instrument: the cloud and aerosol optical properties for the different cloud and aerosol masks (phase function, extinction coefficient, single scattering albedo), solar irradiance. The list and description of those general purpose optical and radiative properties is provided in Table 4.2 page 120.

The ancillary data are provided in individual files with granularity identical to the geolocation files (approximately 5 min tiles of observation) whereas the optical properties database files are provided in hdf5 format following a different structure since information do not depend on time or location. The solar irradiance is stored in ASCII format since it is very light and simple data.

Parameter	**dataset**	**unit**	**source**
Time of observation	TAI_Time	ms	4MSDS/WP1 geolocation data
Longitude	Longitude	degrees	4MSDS/WP1 geolocation data
Latitude	Latitude	degrees	4MSDS/WP1 geolocation data
Solar zenith angle	SZA	degrees	4MSDS/WP1 geolocation data
Solar azimuth angle	SAA	degrees	4MSDS/WP1 geolocation data
View zenith angle	VZA	degrees	4MSDS/WP1 geolocation data
View azimuth angle	VAA	degrees	4MSDS/WP1 geolocation data
Temp profile	T	K	ECMWF
Temp at 2m altitude	2T	K	ECMWF
Pressure Profile	P	hPa	ECMWF
Ground “skin” temperature	SKT	K	ECMWF

IWVP = Integrated Water Vapor path	TCWV	mm	ECMWF
Water Vapour Profile (relative humidity)	Humidity_Profile	%	ECMWF
Ozone Profile (Mass mixing ratio)	O3	No unit	ECMWF
Cloud Mask	cloud_mask, cloud_phase, cloud_type)	No unit	AVHRR level 2 data
Cloud Effective radius	cld_reff_dcomp	Microns	AVHRR level 2 data
Cloud Altitude	cld_heigh_base_acha	Km	AVHRR level 2 data
COD (Cloud Optical Depth)	cloud_opd_dcomp	No unit	AVHRR level 2 data
Aerosol Mask (type)	Predominant type	No unit	Model MACC
Aerosol optical Depth	AOD550	No unit	Model MACC
Ground Pressure	Surface_Pressure	hpa	ECMWF
Ground Altitude	surface_elevation	Meter	ETOPO5
Land/water mask	land-water_mask	No unit	MODIS (MOD44W)
Ground Albedo (reflection Li-Ross[13] parameters for visible and nearinfrared)	BRDF_Albedo_ParameterX_bandY	No unit	NASA/MODIS
Ground Emissivity (for thermal infrared channels)	Emis_LAMBDA	No unit	NASA/MODIS
Ground IGBP classification	Majority_Land_Cover_1	No unit	MODIS (MOD12C1)
Wind surface U and V (zonal and longitudinal)	10U, 10V	ms^{-1}	ECMWF
Water reflectance	Rrs_LAMBDA		CCI Ocean Color

Table 4.1: *List of the input parameters with corresponding dataset name within hdf5 files, units of the parameters and the origin of the parameter.*

Parameter	**dataset**	**unit**	**source**
Liquid clouds optical	extinction_efficiency,	No unit	Mie computation from

3*Li-ross parameters (k(λ), k1 and k2; k(λ) is the albedo, k1 and k2 describe the repartition of the reflexion: Lambertian/Specular; see* Maignan, Bréon, Lacaze *(2014).*

Parameter	dataset	unit	source
properties (extinction coefficient, SSA, vector phase function)	single_scattering_albedo, pxx_phase_function		microscopic properties.
Ice clouds optical properties (extinction coefficient, SSA, vector phase function)	extinction_efficiency, single_scattering_albedo, pxx_phase_function	No unit	From the databases of P. Yang and B. A. Baum: *Yang et al* (2005); *Baum et al* (2011). http://www.ssec.wisc.edu/ice_models/
Aerosol optical properties (extinction coefficient, SSA, vector phase function)	extinction_efficiency, single_scattering_albedo, pxx_phase_function	No unit	From OPAC database and Dubovik et al., 2002a.
Solar Irradiance	(no dataset)	$W\ m^{-2}$	From database of *Kurucz* (1992), available on: http://www.libradtran.org/

Table 4.2: List of the input parameters corresponding to optical and radiative properties along with corresponding SDS name within hdf5 file, units and origin of the parameter.

4.1.2 Sources of ancillary data

The ancillary data documented here have been obtained from various sources (observation, models, reanalysis) and have been sampled and reformatted in a common data format (hdf5) to facilitate their use within the VII and 3MI simulators.

However, we have taken the approach to conserve integrity of original data product in terms of naming convention, physical meaning, physical units and valid range. It is therefore easy to relate the ancillary data provided here to their original sources and associated documentation.

Any subsequent transformation of ancillary data if performed when needed within the VII or 3MI simulators so that ancillary data provided for 3MI and VII are similar and directly comparable to their original sources.

Origin of each ancillary dataset is identified in section 4.3 of this document and is also provided within the hdf5 files through attributes associated to each Science Data Set (SDS).

Except for the full resolution AVHRR cloud products that have been obtained upon request made to Dr. Andrew Heidinger (NOAA/NESDIS Center for Satellite Applications and Research), all other sources of information are publicly available online through identified web servers or datapool centres.

4.2 Assumptions for use of ancillary data

Most parameters required for simulation can be used directly by the two simulators (MOMO and ARTDECO) after adequate handling of physical units and vertical profile sampling. However, due to the LUT approach used by MOMO and the computational constraint related to calculation of optical properties for a potentially infinite number of aerosol/cloud types and particle sizes, we have imposed a discrete selection of physical values for some aerosols and clouds properties. We describe in the following how ancillary information on clouds and aerosols are actually mapped to relevant input values within the simulator.

4.2.1 Mapping of ancillary cloud products to cloud properties

Atmosphere layering (apply to ARTDECO simulator)

We use the layering defined by the ECMWF profile levels. The layers may then be filled with aerosol or cloud. In case of clouds, we add an altitude level for the cloud top to be placed at the good altitude. The bottom of atmosphere is adjusted to account for the ground elevation either by cutting or extrapolating the ECMWF profile.

Particle phase

Only water or ice clouds are being considered and no attempt is made to simulate mixed phase clouds. The AVHRR phase class “mixed” is assumed to be liquid in the simulator. Note however that information on presence of multilayer situation is available and that this particular situation can be simulated with ARTDECO as part of the additional test data.

Particle size

For clouds we imposed a discrete selection on the potential values taken by the particle size so that cloud optical properties can be inferred directly from the corresponding LUT without further need for interpolation. Cloud particle size is allowed to take discrete values in 1 micron intervals and ancillary values obtained from AVHRR (cld_reff_dcomp parameter) are rounded to the nearest integer before being input to the atmosphere description fed to the simulator.

Particle vertical profile within cloud layer

Cloud layer are not homogeneous by nature but have been historically simulated as homogeneous layers in operational remote sensing applications using passive measurements. Platnick (2001) showed that differential vertical photon penetration occurs when considering different spectral channels and therefore it is expected that different wavelength (especially in the SWIR) will be sensitive to different vertical portion of the cloud layer.

However, specifying a realistic vertical distribution for each cloudy pixel would be computationally expensive and practically impossible if a LUT approach is being used.

Instead, to mimic different photons penetration depth within a cloud having a non homogeneous vertical distribution of particle size, we are using different effective radii values for the different SWIR channels that need to be simulated.

For this purpose, we assume that particle size is increasing slightly as we go deeper in ice clouds (sedimentation) whereas it decreases for liquid clouds (particle growth).

Based on the effective size retrieved from AVHRR using the 3.7 micrometers channel the corresponding values for the 1,37, 1.6 and 2.1 micrometers channels are derived as follows depending on cloud phase.

Reff (lambda) = C(lambda) * Reff (3.7)

For ice clouds :	For Liquid clouds :
C(1.37) = 1.2	C(1.37) = 0.90
C(1.6) = 1.2	C(1.6) = 0.90
C(2.1) = 1.1	C(2.1) = 0.95

All other visible and near-infrared channels simulations make use the Reff(2.1) value.
All thermal IR channels simulations make use of the Reff(3.7) value.

4.2.2 Mapping of ancillary aerosol products to aerosol properties

Reanalysis from the MACC project are being used to provide a complete coverage of aerosol information both in clear and cloudy conditions. MACC product provide information on total optical thickness at 550 nm as well as fractional optical thickness for the 5 following species :

BCAOD550	Black Carbon Aerosol Optical Depth at 550nm
DUAOD550	Dust Aerosol Optical Depth at 550nm
OMAOD550	Organic Matter Aerosol Optical Depth at 550nm
SSAOD550	Sea Salt Aerosol Optical Depth at 550nm
SUAOD550	Sulphate Aerosol Optical Depth at 550nm

Considering a full mixture of aerosol is again considered as computationally too expensive given the expected usage of the simulated dataset and practically impossible to handle through a LUT approach. Instead the 5 fractional optical thicknesses provided by MACC are used to identify the dominant type of aerosol (Organic and Sulfate AOD are summed up) which is then used to select relevant optical properties among fixed aerosol models chosen in the OPAC database (Hess et al, 1998) completed with the dust non spherical aerosol model from Dubovik et al (2002). The aerosol layer is assumed to be distributed over the atmospheric column following an exponential decay with a scale height given in Table 4.3 hereafter. This results in having sea salt aerosols located mostly near the surface, dust aerosols in the lower troposphere while black carbon and organic matter/sulfate aerosols are mixed homogeneously with gaseous atmosphere.

Dominant MACC AOD	Selected optical properties	Layer top altitude
Black Carbon	OPAC Continental average	8 km
Dust Aerosol	Desert Dust (Dubovik et al, 2002)	2 km
Organic Matter + Sulphate Aerosol	OPAC Urban	8 km
Sea Salt Aerosol	OPAC Maritime Clean	1 km

Table 4.3: Correspondence between MACC predominant aerosol type and selected optical properties fed to simulator.

4.2.3 Mapping of BPDF for various IGBP ground class

The land bidirectionnal polarized reflectance model that we use has one parameter that was set for each IGPB class by Maignan et al., 2009. We use the Majority_Land_Cover_1 ancillary data to set the corresponding parameter. The refractive index for the ground that is also used for the Maignan et al., 2009 model is set constant to n = 1.5 + i 0.0.

4.3 Description of the ancillary datasets content and format

The input parameters can be found in different files depending on whether they depend on time/location or are general purposes information relative to optical and radiative properties of atmospheric particles. Note that the later can be considered integral parts of the simulator and therefore are only mentioned here for completeness but are not being delivered as part of the ancillary dataset which will consist only of pixel level ancillary information.

4.3.1 General purposes ancillary information

Database of optical and radiative properties of aerosols and clouds are provided in separate hdf5 datafiles for each particle type (liquid cloud droplets, ice cloud crystals, aerosols) and for each instrument. The ancillary data provided at pixel level are used to determine which properties are to be used for describing the atmosphere. A description of ancillary information mapping to the optical properties look-up table has been provided in section 4.2.1 and 4.2.2.

- FWC: Optical properties for Water Clouds, name: opt_liquid_cl_INSTRUMENT.hdf5. For each channel, for 25 different effective radii of the clouds droplets, and 5 different effective variance (σ), namely for 25*5=125 size distributions.
- FIC : Optical Properties for Cirrus Clouds, name: opt_baum_cirrus_INSTRUMENT.hdf5. For each channel, for 23 different cirrus types.
- Faer: Aerosols. The optical properties of some main aerosols models will be put in an hdf5 file similar to those of the clouds.
- Faer: Aerosols. The optical properties of some main aerosols models will be put in an hdf-5 file similar to those of the clouds.

For ice clouds optical properties, we used the Baum models (see http://www.ssec.wisc.edu/ice_models/polarization.html). The effective radii are those sampled in the Baum LUT (from 5.0 to 60 microns with a 2.5 microns step). In the simulator, we select the nearest value corresponding to effective radius given by AVHRR. The properties (single scattering albedo, extinction coefficient, phase matrix) are interpolated (linearly) to the 3MI and METimage ISRF center wavelengths for the LUT. The angular grid for the phase matrix is the one from the original Baum LUT.

For liquid clouds, we compute optical properties using a Mie code. The size distribution is a log-normal with an effective variance of 0.09 microns. We sampled the effective radius by step of 1 micron from 5 to 30 microns. Again, the nearest radius is selected in the simulator according to the AVHRR product. The phase matrix was computed using a regular grid of 0.2 degree resolution. The optical properties are computed for each of the 3MI and METimage wavelengths (ISRF center wavelengths).

All phase matrices (aerosols, cirrus and liquid clouds) are expended into Legendre polynomials and truncated using the delta-M truncation (Wiscombe, W. J. The Delta-M Method: Rapid Yet Accurate Radiative Flux Calculations for Strongly Asymmetric Phase Functions. Journal of Atmospheric Sciences, 1977, 34, 1408-1422). We performed the expansion for various numbers of Legendre coefficients and store it in the LUT.

Additionally a text file is provided to document the TOA nadir solar irradiance

- Fsol: Solar Irradiance. Text document containing the integrated solar irradiance at nadir at the TOA (Top of the Atmosphere). 3MI and METImage datafiles are named solrad_kdis_game3mi_kurudz_full.dat and solrad_kdis_gamemetim_kurudz.dat respectively. The solar irradiance for each band is obtained by integrating the spectral irradiance into the instrument spectral response function of the band.

4.3.2 Pixels dependent ancillary information

All parameters relative to pixel level information are provided in files corresponding to approximately 5 minutes of observations with data mapping and granularity similar to the geolocation and observation geometries files. A direct relation can be made between geolocation and ancillary datafiles to match any observed pixel with the required ancillary data. Filename convention follows similar rules to the one used for geolocation and use the ANCILLARY key to identify content.

As an example, for the instrument METImage (VII), and for the first segment (8:46:02 am) of the third orbit (23 th February 2008), using the production version referenced 1.2 the file is named:

---------- EPS-SG_VII_ANCILLARY_2008-02-23T08-46-02_V1.2.he5

A similar file for the 3MI instrument would accordingly be named

---------- EPS-SG_3MI_ANCILLARY_2008-02-23T08-46-02_V1.2.he5

All files provided for VII and 3MI simulated datasets are provided in hdf5 format augmented with hdfeos5 attributes. Data are stored in different encoding (8, 16 or 32 bits) which are internally documented in the files through specific attributes. Equation to transform file counts to physical values are also specified and provided as data attributes within the hdf5 files (equation, scale_factor, offset).

4.3.3 Formatting and content of pixel dependent information files

4.3.3.1 General considerations

The hdf5 files containing pixel dependent information for VII and 3MI share a common organization meant to a direct link between each and all single IFOV that have been defined a given GEOLOCATION file and its corresponding ANCILLARY file.

Note that this approach is vastly inefficient in terms of data volume for 3MI because it yields significant information redundancy between successive views of this multiangle instrument. However it provides a uniform and direct access to ancillary information based on the GEOLOCATION files. In addition, there is no need for potential users to manipulate ancillary data fields to perform later analysis of simulated radiances as those will be provided in the exact same geometries hence again facilitating direct comparison between observation geometries, ancillary data that serve as input to simulation and simulated observations.

The geolocation information (Latitude, Longtitude and TAI) already available in the GEOLOCATION files are also duplicated in the ANCILLARY files to facilitate visualization and mapping of ancillary data independently of the availability of the corresponding geolocation file.

Finally, the ancillary data are provided at different resolution depending on their original resolution. Most properties impacting directly realism of simulated images (clouds, aerosols, land surfaces, elevation) are provided at full instrument resolution. When those ancillary datasets were not available at VII or 3MI resolution data have been interpolated to match instrument native resolution.

Other information which do not directly impact image realism such as meteorological fields and profiles (Surface pressure, Temperature, Humidity) are provided at a lower resolution (ie degraded resolution compared to VII and 3MI native resolution) which remain comparable to the original dataset resolution. Those ancillary information are defined and grouped in the hdf5 files separately from the other full resolution data has will be described in the next section.

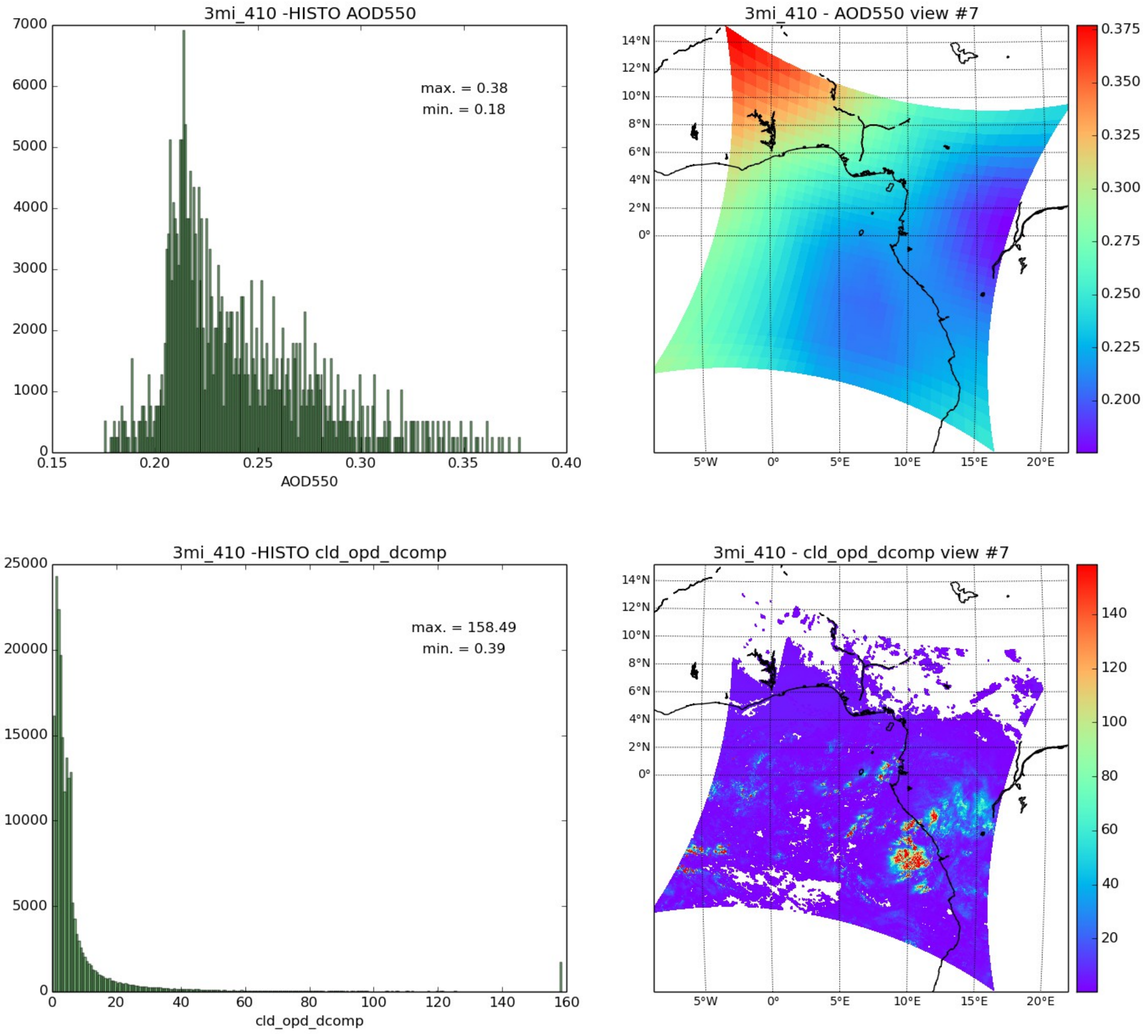

Figure 4.1 : Histogram and projection of the aerosol optical depth at 550nm (top panel) and cloud optical depth (bottom panel). Those are gridded to the 3MI 410nm band in view #7 of the granule dated 2008-02-23T09-01-26. Note that the cloud optical depth (bottom) is at instrument resolution while the aerosol optical depth (top) is at lower resolution.

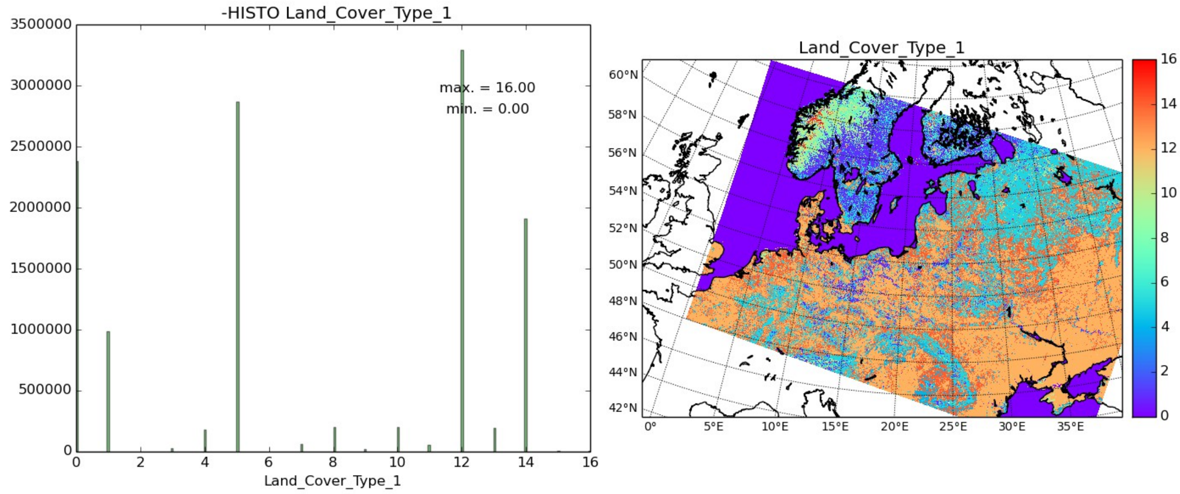

Figure 4.2 : Histogram and projection of the land cover IGPB type. Here the data are gridded to the MetImage granule dated 2008-02-23T08-46-02.

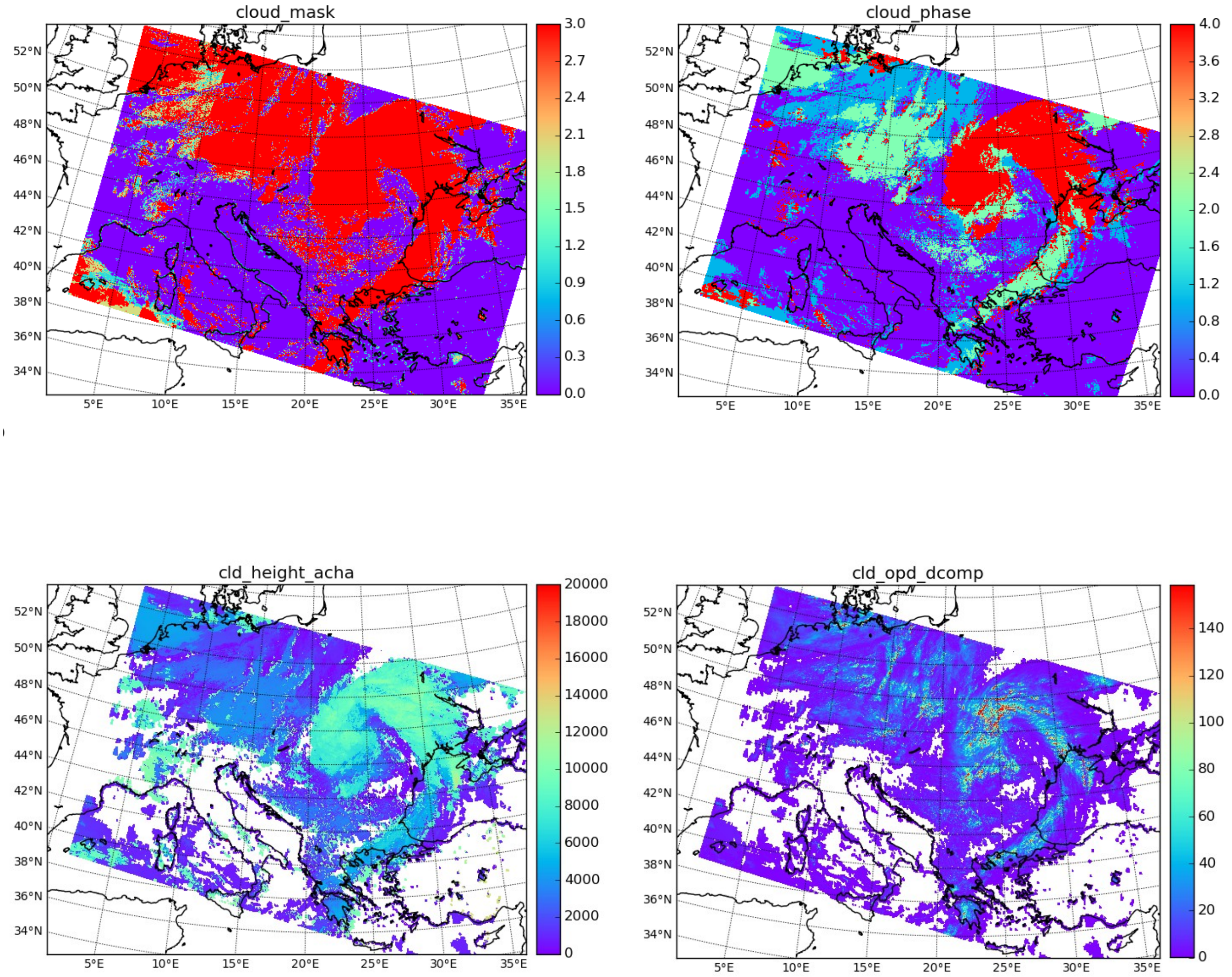

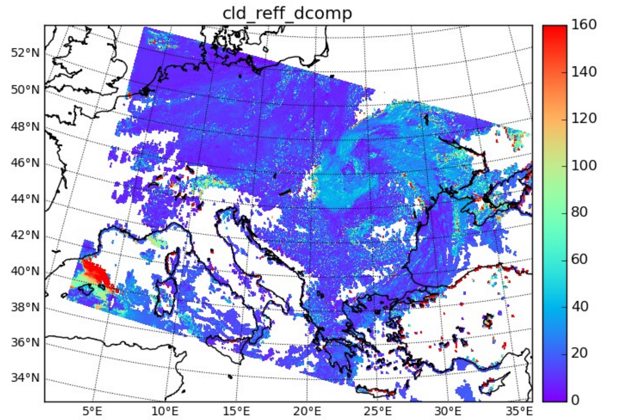

Figure 4.3: *Example of full resolution ancillary parameters used as input of the VII simulation : Total cloud coverage and cloud phase, cloud top height, cloud optical thickness and effective particle size obtained from AVHRR products for granule 2007-09-12T08-43-03.*

4.3.3.2 Datasets folders structure

For each instrument (VII or 3MI) the ancillary files contain two groups of data corresponding to full resolution and low resolution information.

For VII the groups are found in hdf5 directory :

/HDFEOS/SWATHS/VII_SWATH_Type_L1B_500m/
/HDFEOS/SWATHS/VII_SWATH_Type_L1B_LowRes/

For 3MI, information is also provided for the VIS and the SWIR channels independently and similarly to the GEOLOCATION files structure. These groups are found respectively in hdf5 directory :
- for the visible channels :

/HDFEOS/SWATHS/3MI_SWATH_VIS_Type_L1B/
/HDFEOS/SWATHS/3MI_SWATH_VIS_Type_L1B_LowRes/

- for the shortwave infrared channels :

/HDFEOS/SWATHS/3MI_SWATH_SWIR_Type_L1B/
/HDFEOS/SWATHS/3MI_SWATH_SWIR_Type_L1B_LowRes/

Each group then contains “**Geolocation Fields**” and “**Data fields**” which contents are described in the following section.

Note again that the content of each “**Data fields**” directory is similar for VII and 3MI (the same information are provided) and that only the size and shape of data arrays differ between the two instruments. The shape and size of arrays are determined by their counterparts GEOLOCATION fields and are (I) identical for the full resolution data or (ii) subsampled by a given factor for the LowRes data (see description of sampling factor in subsection “ *Low resolution (LowRes) data fields* “ hereafter).

4.3.3.3 Ancillary Fields description

The Geolocation Fields directory contains the **Latitude**, **Longitude** and **TAI_Time** datasets which are the exact replicate of the SDS that can be found in the GEOLOCATION files (subsampled for the LowRes fields).

The Data Fields directory contains all the ancillary information either at full or low resolution.

Full resolution data fields

For the ancillary information available at full resolution the following SDS are provided in the hdf5 ANCILLARY data files (parameters appear in blue bold font) :

BRDF_Albedo_Parameter1_Band1 ([...]Band2, Band3, Band4, Band5, Band6, Band7)

BRDF_Albedo_Parameter2_Band1 ([...]Band2, Band3, Band4, Band5, Band6, Band7)

BRDF_Albedo_Parameter3_Band1 ([...]Band2, Band3, Band4, Band5, Band6, Band7)

Data sources :
MODIS BRDF/Albedo Product MCD43
or MODIS BRDF/Albedo CMG Gap-Filled Snow-Free Product MCD43GF V005
http://www.umb.edu/spectralmass/terra_aqua_modis/

These parameters correspond to the 3 parameters (Parameter1, Parameter2, Parameter3) required to described the surface using a kernel-driven semiempirical BRDF model, utilizing the RossThick-LiSparse kernel functions for characterizing isotropic (Parameter1), volume (Parameter2) and surface (Parameter3) scattering (Schaaf et al., 2002; 2011).

The MODIS Albedo Product MCD43 is the baseline source for this ancillary information When no data is available for the closest 16-days period corresponding to the simulation time, the GAP-Filled snow free product (MCD43GF) is used instead to provide as much coverage as possible.

The 3 parameters are provided for the 7 MODIS bands (2 x 250 m resolution + 5 x 500m resolution) covering the following spectral range :

MODIS Band	Bandwidth (nm)
1	620 - 670
2	841 - 876
3	459 - 479
4	545 - 565
5	1230 - 1250
6	1628 - 1652
7	2105 - 2155

These values are spectrally interpolated (or extrapolated) to obtain the corresponding surface parameters for any given 3MI or VII channels.

Emis_20 , Emis_22 , Emis_23 , Emis_29 , Emis_31 , Emis_32

Data sources :
For VII High Resolution only : MODIS Land Surface Temperature and Emissivity Daily L3 Global 1 km (MOD11A1) and corresponding 8-day synthesis (MOD11A2)
For 3MI and VII Low resolution : MODIS Land Surface Temperature and Emissivity Daily L3 Global 0.05Deg CMG (MOD11C1) and corresponding 8-day synthesis (MOD11C2)
https://lpdaac.usgs.gov

Daily surface emissivity derived from MODIS for bands 20, 22, 23, 29, 31 and 32.

MODIS Band	Bandwidth (micrometers)
20	3.660 - 3.840
22	3.929 - 3.989

23	4.020 - 4.080
29	8.400 - 8.700
30	9.580 - 9.880
31	10.780 - 11.280
32	11.770 – 12.270

These values are spectrally interpolated (or extrapolated) to obtain the corresponding values for VII channels.

Majority_Land_Cover_Type_1 (or Land_Cover_Type_1 for VII 500 m resolution)

Data source :
For 3MI and LowRes : **MODIS Land Cover Type Yearly L3 Global 0.05Deg (MOD12C1)**
For VII HighRes : MODIS Land Cover Type Yearly L3 Global 500 m (MOD12Q1)
https://lpdaac.usgs.gov

Dominant IGBP land cover type within 0.05 deg cell. The primary land cover scheme identifies 17 land cover classes defined by the International Geosphere Biosphere Programme (IGBP), which includes 11 natural vegetation classes, 3 developed and mosaicked land classes, and three non-vegetated land classes. This product is used to identify relevant surface properties when other ancillary information are non available.

Rrs_412, Rrs_443 , Rrs_490 , Rrs_510 , Rrs_555 , Rrs_670

Data source : ESACCI-OC-L3S-RRS-MERGED-1D_MONTHLY_4km
http://www.esa-oceancolour-cci.org/?q=documents

Sea surface reflectance defined as the ratio of water-leaving radiance to surface irradiance at 412, 443, 490, 510, 555 and 670 nm. Product provided by the Ocean Colour Climate Change Initiative (Remote sensing reflectance).

These values are spectrally interpolated (or extrapolated) to obtain the corresponding surface parameters for any given 3MI or VII channels.

land-water_mask

Data source : MODIS product MOD44W
https://lpdaac.usgs.gov/

The MODIS 250 m land-water mask (MOD44W product) is a Land Water mask derived from MODIS and SRTM L3 Global 250 m SIN Grid.

elevation

Data source : World digital elevation model (ETOPO5).
Ref : Data Announcement 88-MGG-02, Digital relief of the Surface of the Earth. NOAA,

National Geophysical Data Center, Boulder, Colorado, 1988

Global land and sea- floor elevations on a 5-minute latitude/longitude grid

AVHRR Cloud Products and related ancillary data.
http://cimss.ssec.wisc.edu/clavr/clavr_page_files/clavrx_users_guide_v0.4.pdf
contact : Andrew Heidinger NOAA/NESDIS Center for Satellite Applications and Research.

Ancillary information on clouds and associated information used during processing of AVHRR data have been obtained through The Clouds from AVHRR Extended System (CLAVR-x). CLAVR-x is a processing system developed at NOAA/NESDIS and UW/CIMSS for generating quantitative cloud products in real-time from the Advanced Very High Resolution Radiometer (AVHRR). Data have been obtained per request made to Andrew Heidinger.

From the processing of Full Resolution Area Coverage (FRAC) the following 7 parameters on clouds are obtained and used at 1km resolution to describe cloud cover and properties in the simulation of VII and 3MI observations. VII (500m) and 3MI native resolution corresponding fields have been obtained through nearest pixel interpolation when required.

cld_height_base_acha

cloud base height estimate derived from the AWG Cloud Height Algorithm (ACHA)

cld_height_top_acha

cloud top height estimate derived from the AWG Cloud Height Algorithm (ACHA)

cld_opd_dcomp

Cloud Optical Depth retrieval from the Daytime Cloud Optical and Microphysical Properties (DCOMP) algorithm.

cld_reff_dcomp

Cloud particle effective radius retrieval from the Daytime Cloud Optical and Microphysical Properties (DCOMP) algorithm.

cloud_mask

cloud mask obtained from CLAVR-X (Heidinger et al. 2012).

cloud_phase

cloud thermodynamic phase index obtained from the cloud type index
(0=clear,1=water,2=supercooled water,3=mixed,4=ice,5=unknown)

cloud_type

integer classification of the cloud type including clear and aerosol type : 0=clear, 1=probably clear, 2=fog, 3=water, 4=supercooled water, 5=mixed, 6=opaque_ice, 7=cirrus, 8=overlapping, 9=overshooting, 10=unknown, 11=dust, 12=smoke
For details refer to : Pavolonis et al. (2005) and Pavolonis and Heidinger (2004)

The 6 following additional ancillary information have been extracted from AVHRR CLAVR-X products for redundancy and cross verification purposes but are not of primary use for the simulation unless when other directly relevant information is missing.

mean_sealevel_pressure_background

mean sealevel pressure assumed using ancillary data sources

surface_elevation

surface elevation above mean sea level

surface_relative_humidity_nwp

near-surface relative humidity from NWP ancillary data

surface_temperature_background

surface temperature assumed using ancillary data sources

surface_type

UMD surface type: water=0, evergreen_needle=1, evergreen_broad=2, deciduous_needle=3, deciduous_broad=4, mixed_forest=5, woodlands=6, wooded_grass=7, closed_shrubs=8, open_shrubs=9, grasses=10, croplands=11, bare=12, urban=13

wind_speed_10m_nwp

wind speed from the NWP ancillary data at 10m above ground level

Low resolution (LowRes) data fields

Except for the ancillary information obtained from the AVHRR CLAVR-X processing, all high resolution information described in the previous subsection are also available in the low resolution data fields.
In addition, the LowRes data fields provide information on :

- atmospheric state variables from meteorological reanalysis (ECMWF reanalysis)
- aerosol concentration and type from reanalysis provided by the MACC-II project (https://www.gmes-atmosphere.eu/services/gac/reanalysis/)

Both type of information are provided only at lower resolution for several reasons. First, because the corresponding quantities vary more slowly in space than cloud fields and surface properties, having low resolution description of those do not impact realism of simulated images. Secondly, those information are provided by models reanalysis with resolution that are much coarser than the VII and 3MI native resolution. Therefore any attempt to create high resolution fields from those data would simply increase the data volume through highly redundant oversampled information.

High Resolution (native) and Low Resolution grid definition

The low resolution fields have reduced resolution compared to the high resolution (native) geolocation fields as described in Table 4.4 page 134.
For 3MI a 2D ancillary field is a 4-dimensional array with data field array dimension corresponding to : nb of sequences x nb of spectral channels x along track nb of samples x across track nb of samples .
In case of 3D ancillary fields (meteorological profiles) the array has a 5th dimension corresponding to the number of profile levels (21, 60 or 91 depending on variable).

For VII a 2D ancillary field is a 2-dimensional array with data field array dimension corresponding to : along track nb of samples x across track nb of samples .
In case of 3D ancillary fields (meteorological profiles) the array has a 3rd dimension corresponding to the number of profile levels (21, 60 or 91 depending on variable).

	HighRes Data fields	LowRes Data Fields
3MI - VIS	14 x 9 x 512 x 512	14 x 9 x 32 x 32 (x Z)
3MI - SWIR	28 x 4 x 256 x 500	28 x 4 x 16 x 31 (x Z)
VII	3800 x 3264	200 x 204 (x Z)

Table 4.4: Dimension of data field arrays for 3MI-VIS, 3MI-SWIR and VII ancillary dataset.

Meteorological fields

The following parameters are extracted directly from ECMWF reanalysis distributed by ECMWF and available at ICARE Data and Services Center

10U 10 metre U wind component
10V 10 metre V wind component
2T 2 metre temperature
CC Cloud cover (Profile[4])
LNSP Logarithm of surface pressure
LSM Land-sea mask

4Provided on 60 or 91 pressure levels depending on date – see ECMWF model levels definition for details at http://old.ecmwf.int/products/data/technical/model_levels/

O3	Ozone mass mixing ratio
R	Relative humidity (Profile[5])
SKT	Skin temperature
T	Temperature (Profile[5])
TCC	Total cloud cover
TCWV	Total column water vapour
Z	Geopotential (Profile[5])

Aerosol fields

The following aerosols parameters are extracted directly from MACC reanalysis distributed by the MACC project and available at ICARE Data and Services Center

AOD550	Total Aerosol Optical Depth at 550nm
BCAOD550	Black Carbon Aerosol Optical Depth at 550nm
DUAOD550	Dust Aerosol Optical Depth at 550nm
OMAOD550	Organic Matter Aerosol Optical Depth at 550nm
SSAOD550	Sea Salt Aerosol Optical Depth at 550nm
SUAOD550	Sulphate Aerosol Optical Depth at 550nm

5Provided on 21 levels at pressure levels (hPa) :
1,2,3,5,7,10,20,30,50,70,100,150,200,250,300,400,500,700,850,925,1000

5 Delivered synthetic observation dataset

5.1 Simulated observations example

We present in the following sample images extracted from the simulated dataset.

Figure 5.1 : Artistic view of two consecutive daytime VII overpasses illustrating the complete coverage at Equator obtained from the simulated orbit and swath. Orange lines on ground indicate cross-track coverage for part of the first overpass allowing to observe overlap between successive orbits.

Figures 5.1, 5.2 and 5.3 illustrate final outcome from the study performed and help to verify compliance of the simulated dataset with the initial SOW. In particular the complete coverage that shall be obtained from VII can be observed on figure 5.1 where continuous coverage is observed at equator while overlapping orbits at higher latitude is also evident. Further the cross-track swath indicated by orange lines have been established from an independent software (Ixion) and confirm the correct determination of the orbit and sampling performed using our simulator (based on NASA SDP Toolkit).

Figure 5.2 presents one instantaneous snapshot of the 3MI VIS-NIR optical head (true colour composite) on which the temporally simultaneous SWIR observations have been overlaid to illustrate the different size and respective positioning of the two FOV.

Figure 5.3 allows to view an instantaneous snapshot of the 3MI polarization observation (false color RGB composite from 865, 670 and 443 nm channels) overlaid on top of the VII swath (true color RGB composite).

Figure 5.2 : Example of a 3MI false color SWIR composite image overlaid on top of the wider VIS/NIR instantaneous FOV (true color composite).

Figure 5.3 : Example of a 3MI false colour polarized radiance composite image (RGB : 865, 670 and 443 nm) overlaid on top of the wide VII swath image (true colour composite).

5.1.1 Example observations for 3MI

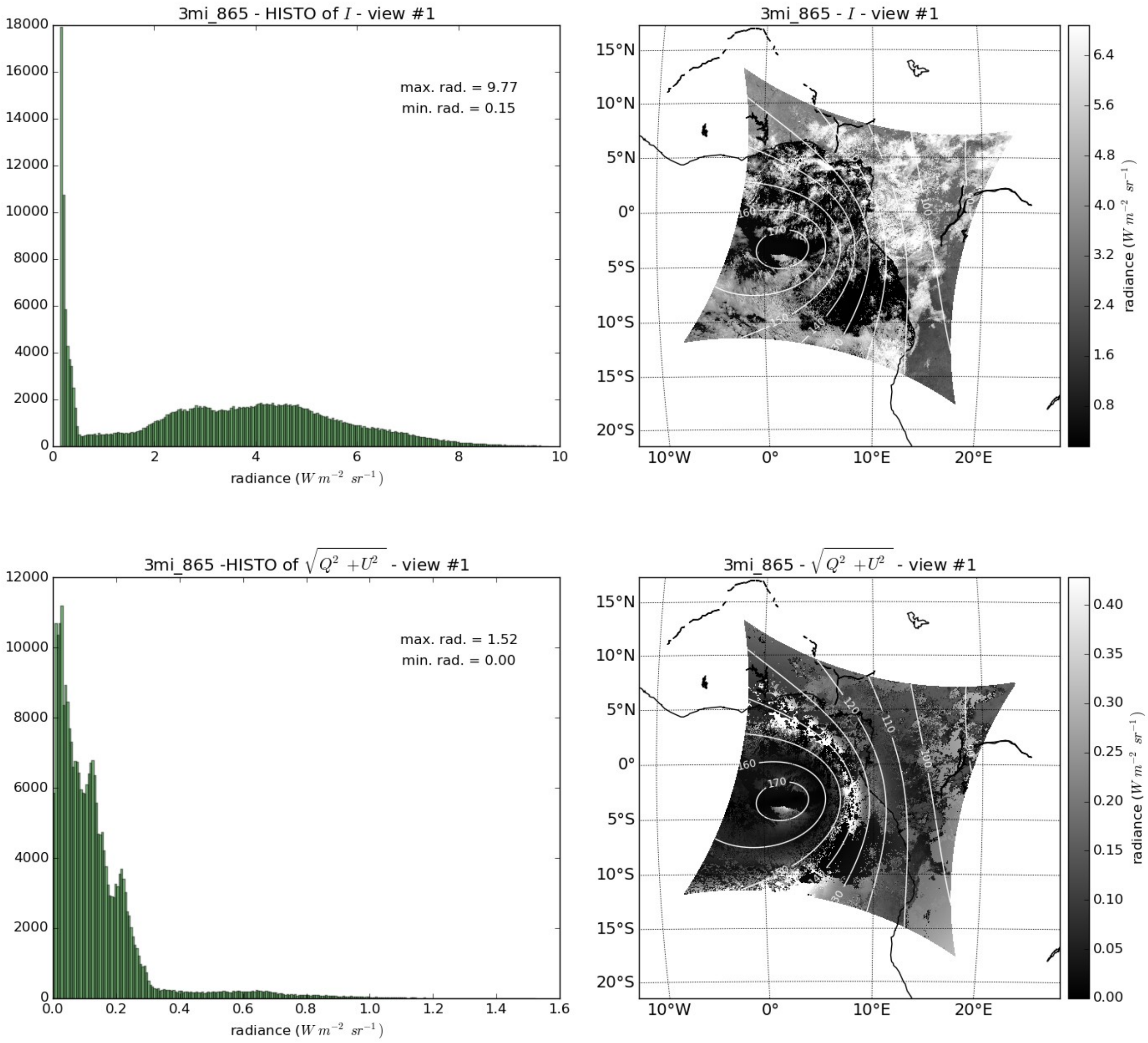

Figure 5.4 : Example of 3MI observations in the 865 nm channel with total radiance (top) and polarized radiance (bottom). Histograms of simulated values are provided for indication of signal levels.

From the polarized radiance images illustrating 3MI observations, typical features from the cloud bow are clearly visible. To help in interpretation of polarization features isolines of scattering angles have been added every 10 degrees allowing to easily identify the backscatter direction (180 degrees) and the cloud bow produced by liquid clouds around 140 degrees of scattering angle.

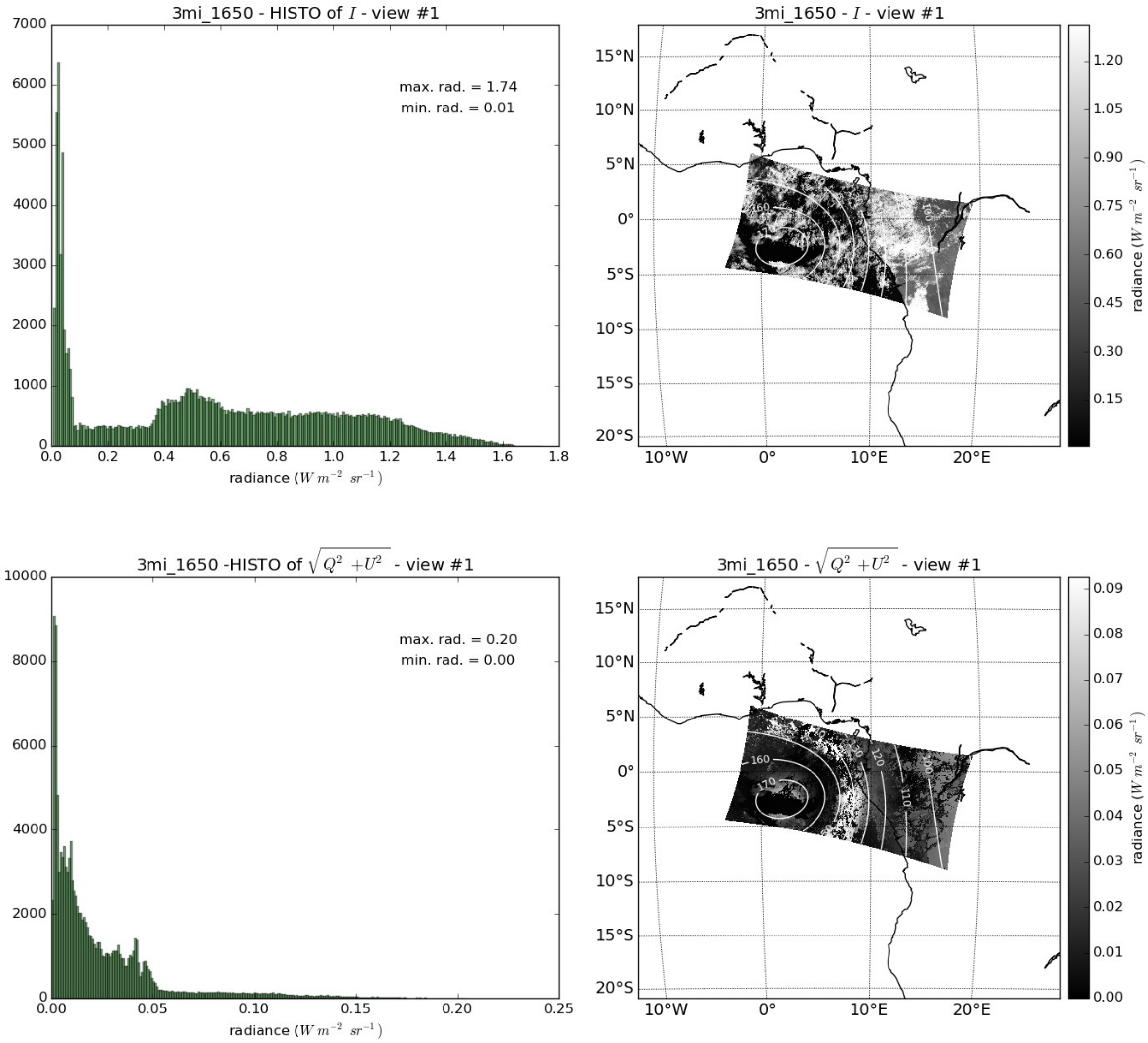

Figure 5.5 : Example of 3MI observations in the 1650 nm channel with total radiance (top) and polarized radiance (bottom). Histograms of simulated values are provided for indication of signal levels. The reduced SWIR FOV can be compared to the VIS FOV from figure 5.4 (p. 137).

The above images illustrate the reduced along track FOV of the SWIR optical head. Note that in the final simulated dataset, the SWIR focal plane array is centred on the VIS one as depicted here.

5.1.2 Example observations for VII

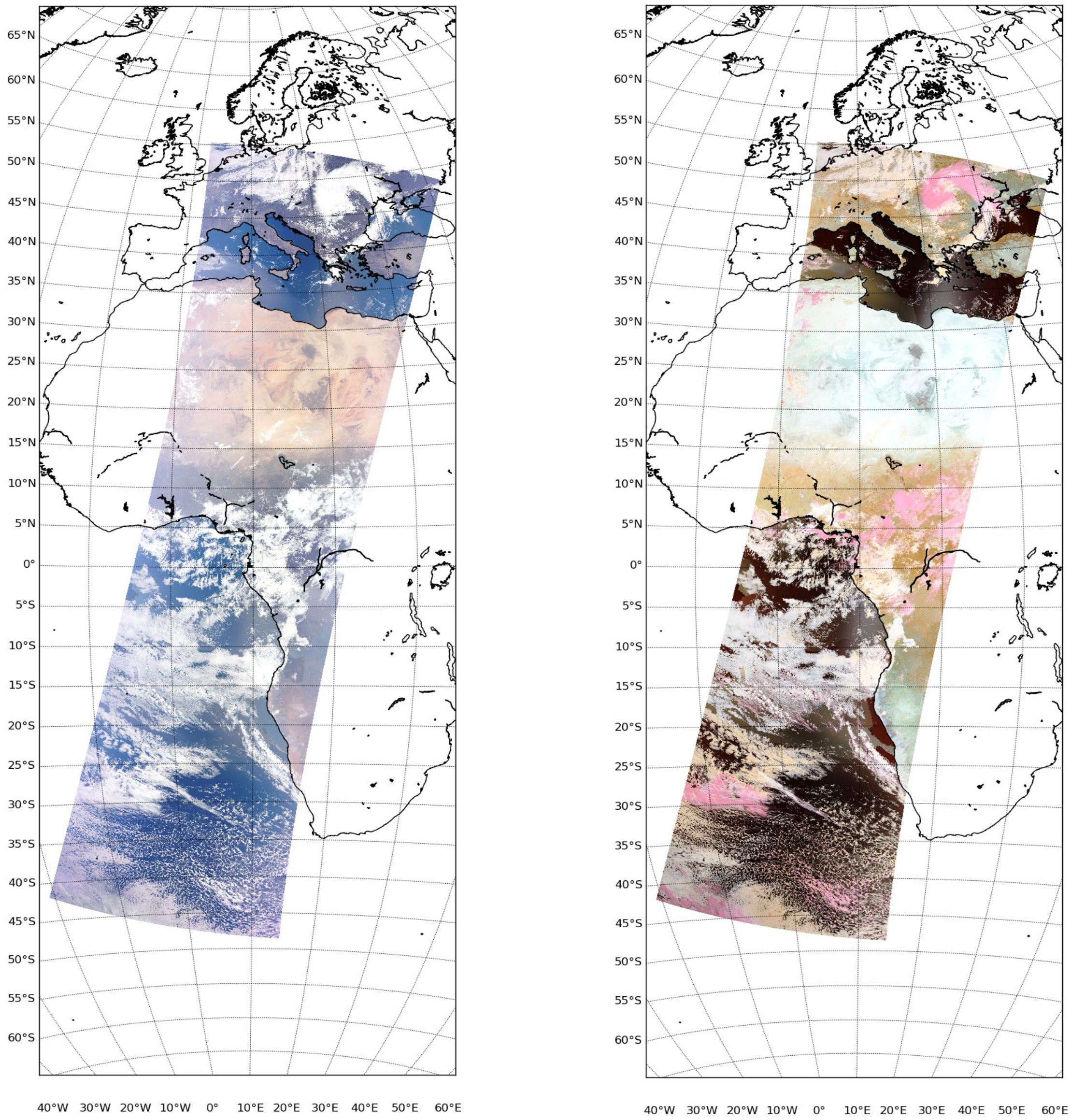

Figure 5.6 : True colour (left : 443, 555 and 670 nm) and false color (right : 865, 1650 and 2230 nm) RGB composite images obtained from aggregation of several VII granules

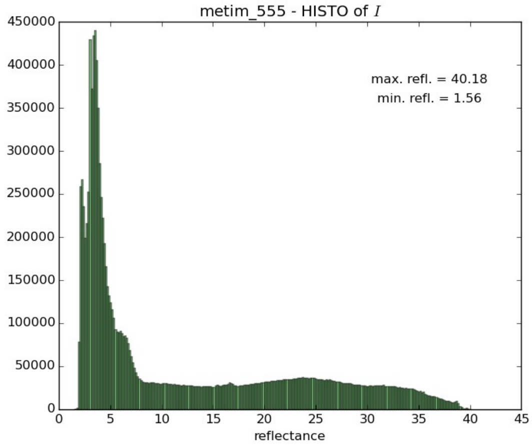
metim_555 - HISTO of I
max. refl. = 40.18
min. refl. = 1.56
reflectance
450000
400000
350000
300000
250000
200000
150000
100000
50000
0
0
5
10
15
20
25
30
35
40
45

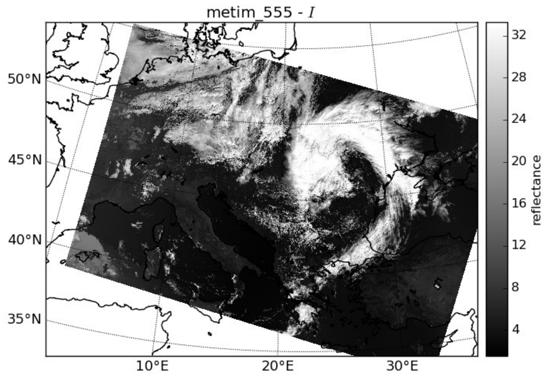
metim_555 - I
50°N
45°N
40°N
35°N
10°E
20°E
30°E
reflectance
32
28
24
20
16
12
8
4

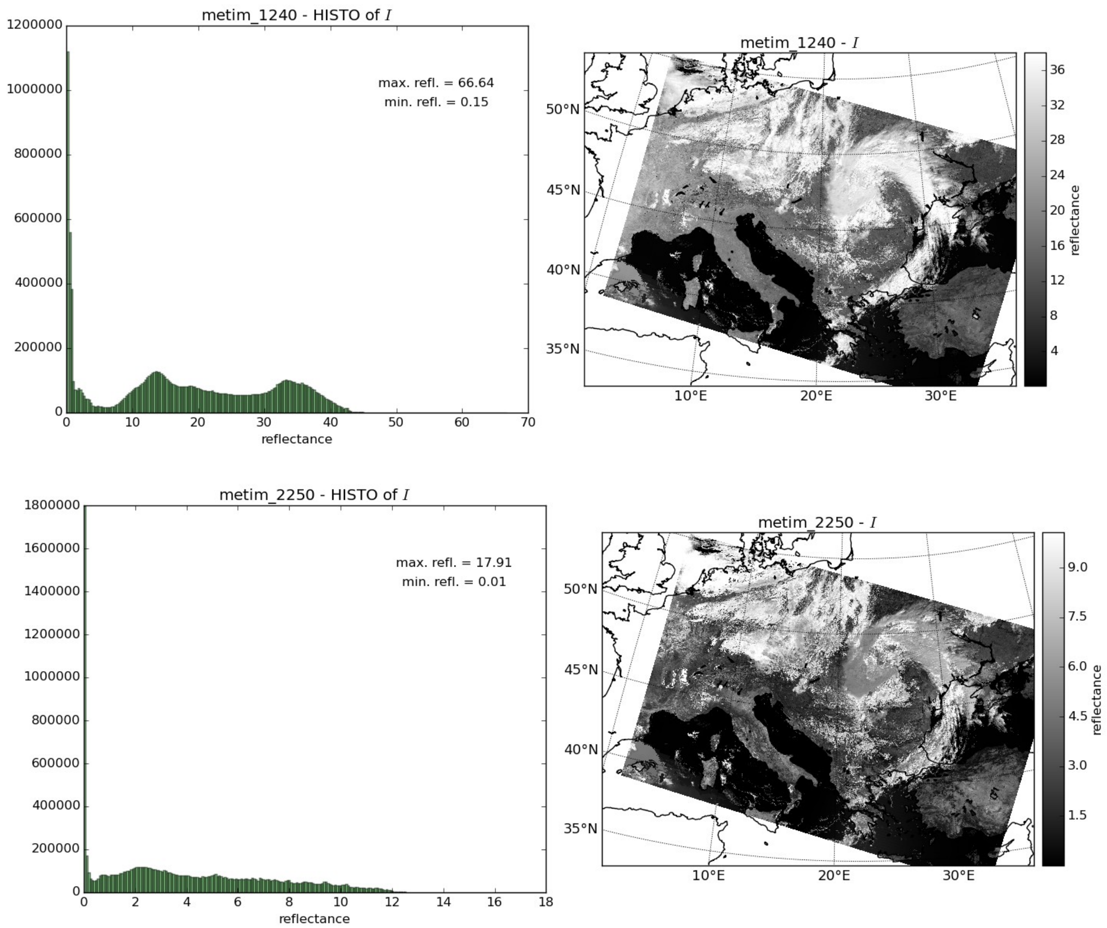

Figure 5.7 : Example of VII observations for the 555 nm (top) 1240 nm (center) and 2250 nm channels (bottom). Histograms of simulated values are indicative of signal levels. Separation of liquid (white) and ice (grey tones) clouds is clearly visible from the 2250 nm channels.

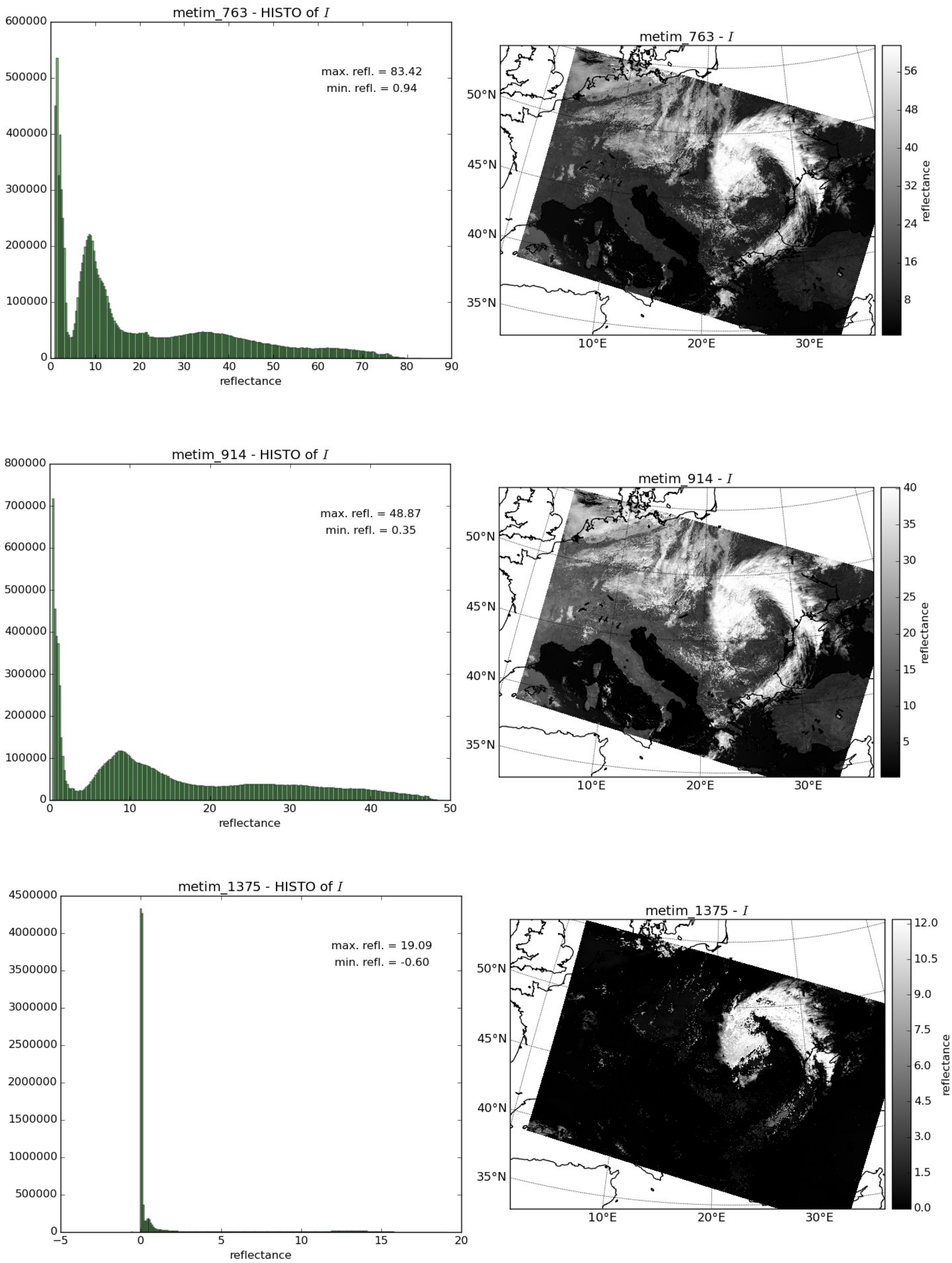

Figure 5.8 : Example of VII observations for the 763 nm (top) 914 nm (centre) and 1375 nm channels (bottom) illustrating several of the VII absorption bands. Histograms of simulated values are provided for indication of signal levels.

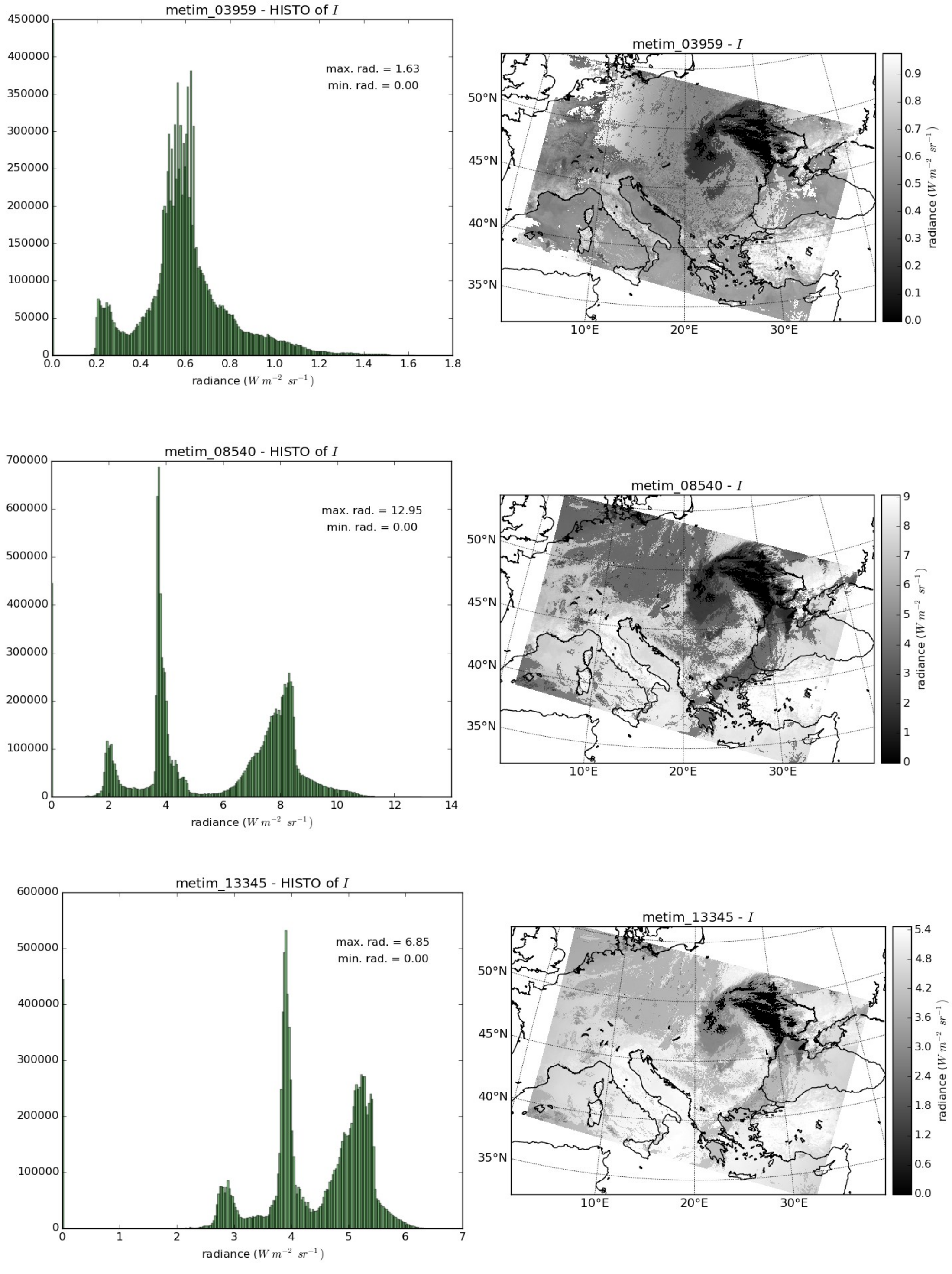

Figure 5.9 : Example of VII observations for the 3.959 micrometers (top) 8.540 micrometers (centre) and 13.345 micrometers channels (bottom) illustrating several of the thermal IR. Histograms of simulated values are provided for indication of signal levels.

5.2 Simulated radiances files format and content

The format of the final output radiances dataset of the project is hdf5 and similarly to the geolocation and ancillary data files, radiances are provided in elementary granules of ~approx 5 min. For each observed pixel, we deliver either the total intensity (for VII) or the Stokes vector components I, Q and U (for 3MI) as spectral radiance in $W.m^{-2}.sr^{-1}.\mu m^{-1}$. Radiances are provided using one dataset per channel in the hdf files. Each dataset is named after the corresponding channel central wavelength and SDS names have been padded with leading 0 to maintain spectral ordering of the various channels when files are opened with graphical interfaces.

Note that each SDS is documented internally to the hdf files using a set of attributes providing ancillary information for the correct interpretation and use of data. In particular, we added to the radiances SDS information on extraterrestrial flux average over the channel width, its central wavelength and considered Full Width at Half Maximum (FWHM) so that users can easily compute normalized radiances from the provided data. Figure 5.10 provides example of such attributes.

HDFEOS/SWATHS/VII_SWATH_Type_L1B/Geolocation Fields/Latitude dataset attributes

Dataset attribute	DataType	Dimensions	Value
physical_units	string	1	degrees_north
long_name	string	1	Geodetic Latitude
_FillValue	float64	1	-999.0

HDFEOS/SWATHS/VII_SWATH_Type_L1B/Data Fields/metim_00443 dataset attributes

Dataset attribute	DataType	Dimensions	Value
computation_status	int64	1	2
unit	string	1	W m-2 sr-1 microns-1
_FillValue	int64	1	32768
unitF0	string	1	W m-2 microns-1
unitFWHM	string	1	microns
unitLAMBDA	string	1	microns
LAMBDA	float64	1	0.443
FWHM	float64	1	0.03
F0	float64	1	1811.51557333

Figure 5.10 : Examples of ancillary attributes added to SDS for internal documentation of data content, format and interpretation.

In addition to this document, an online technical documentation of the radiances files format and content is available at :

http://www.icare.univ-lille1.fr/dev/4MSDS/index.php

5.2.1 3MI radiances file format and content

The 3MI radiances files are structured following the same internal organisation as their corresponding GEOLOCATION files so that VIS/NIR and SWIR data can be found respectively under the directories :

HDFEOS/SWATHS/3MI_SWIR_SWATH_Type_L1B/Data Fields

HDFEOS/SWATHS/3MI_VIS_SWATH_Type_L1B/Data Fields

VIS/NIR and SWIR radiances are provided with different dimensions according to the different VISNIR and SWIR acquisition frequencies. The following table provide a description of the included dataset name and dimensions.

Dataset name	Description and units	Dimension
3mi_00410	I, Q and U Stokes vector components for the 410 nm channel (in W m-2 sr-1 microns-1)	4-D (14x3 x512x512)(1) vector
3mi_00443	I, Q and U Stokes vector components for the 443 nm channel (in W m-2 sr-1 microns-1)	4-D (14x3 x512x512)(1) vector
3mi_00490	I, Q and U Stokes vector components for the 490 nm channel (in W m-2 sr-1 microns-1)	4-D (14x3 x512x512)(1) vector
3mi_00555	I, Q and U Stokes vector components for the 555 nm channel (in W m-2 sr-1 microns-1)	4-D (14x3 x512x512)(1) vector
3mi_00670	I, Q and U Stokes vector components for the 670 nm channel (in W m-2 sr-1 microns-1)	4-D (14x3 x512x512)(1) vector
3mi_00763	I, Q and U Stokes vector components for the 763 nm channel (in W m-2 sr-1 microns-1)	4-D (14x3 x512x512)(1) vector
3mi_00765	I, Q and U Stokes vector components for the 765 nm channel (in W m-2 sr-1 microns-1)	4-D (14x3 x512x512)(1) vector
3mi_00865	I, Q and U Stokes vector components for the 865 nm channel (in W m-2 sr-1 microns-1)	4-D (14x3 x512x512)(1) vector
3mi_00910b	I, Q and U Stokes vector components for the 910 nm channel (in W m-2 sr-1 microns-1)	4-D (14x3 x512x512)(1) vector

Table 5.1: List and description of radiances datasets for VNIR channels

(1) 14 = number of acquisition for a given spectral channel in a 5 mn (308 s) segment; 3 = number of Stokes vectore components provided as I, Q and U for 3MI-VIS; 512 = along-track pixels of a granule, 512 is the number of across-track pixels.

Dataset name	Description and units	Dimension
3mi_00910a	I, Q and U Stokes vector components for the 763 nm channel (in W m-2 sr-1 microns-1)	4-D (28x3 x512x512)(1) vector
3mi_01370	I, Q and U Stokes vector components for the 765 nm channel (in W m-2 sr-1 microns-1)	4-D (28x3 x512x512)(1) vector
3mi_01650	I, Q and U Stokes vector components for the 865 nm channel (in W m-2 sr-1 microns-1)	4-D (28x3 x512x512)(1) vector
3mi_02130	I, Q and U Stokes vector components for the 910 nm channel (in W m-2 sr-1 microns-1)	4-D (28x3 x512x512)(1) vector

Table 5.2: List and description of radiances datasets for SWIR channels

(1) 28 = total number of SWIR acquisition in a 5 mn (308 s) segment; 3 = number of Stokes vectore components provided as I, Q and U for 3MI-SWIR; 256 = along-track pixels of array

5.2.2 VII radiances file format and content

The VII radiances files are structured following the same internal organisation as their corresponding GEOLOCATION files so radiances data can be found under the directory :

HDFEOS/SWATHS/VII_SWATH_Type_L1B/Data Fields

In addition and due to the limited size overload the non corrected latitude and longitude fields have been included in the following directory :

HDFEOS/SWATHS/VII_SWATH_Type_L1B/Geolocation Fields

The following table provide a description of the included dataset name and dimensions.

Dataset name	Description and units	Dimension
HDFEOS/SWATHS/VII_SWATH_Type_L1B/Geolocation Fields		
Latitude	Geodetic Latitude	2-D (3800x3264)[1] array
Longitude	Geodetic Longitude	2-D (3800x3264)[1] array
HDFEOS/SWATHS/VII_SWATH_Type_L1B/Data Fields		
metim_00443	Spectral radiance for the 443 nm channel (in W m-2 sr-1 microns-1)	2-D (3800x3264)[1] array
metim_00555	Spectral radiance for the 555 nm channel (in W m-2 sr-1 microns-1)	2-D (3800x3264)[1] array
metim_00670	Spectral radiance for the 670 nm channel (in W m-2 sr-1 microns-1)	2-D (3800x3264)[1] array
metim_00752	Spectral radiance for the 752 nm channel (in W m-2 sr-1 microns-1)	2-D (3800x3264)[1] array
metim_00763	Spectral radiance for the 763 nm channel (in W m-2 sr-1 microns-1)	2-D (3800x3264)[1] array
metim_00865	Spectral radiance for the 865 nm channel (in W m-2 sr-1 microns-1)	2-D (3800x3264)[1] array
metim_00914	Spectral radiance for the 914 nm channel (in W m-2 sr-1 microns-1)	2-D (3800x3264)[1] array
metim_01240	Spectral radiance for the 1240 nm channel (in W m-2 sr-1 microns-1)	2-D (3800x3264)[1] array
metim_01375	Spectral radiance for the 1375 nm channel (in W m-2 sr-1 microns-1)	2-D (3800x3264)[1] array
metim_01630	Spectral radiance for the 1630 nm channel (in W m-2 sr-1 microns-1)	2-D (3800x3264)[1] array
metim_02250	Spectral radiance for the 2250 nm channel (in W m-2 sr-1 microns-1)	2-D (3800x3264)[1] array
metim_03740	Spectral radiance for the 3740 nm channel (in W m-2 sr-1 microns-1)	2-D (3800x3264)[1] array
metim_03959	Spectral radiance for the 3959 nm channel (in W m-2 sr-1 microns-1)	2-D (3800x3264)[1] array
metim_04050	Spectral radiance for the 4050 nm channel (in W m-2 sr-1 microns-1)	2-D (3800x3264)[1] array
metim_06725	Spectral radiance for the 6725 nm channel (in W m-2 sr-1 microns-1)	2-D (3800x3264)[1] array
metim_07325	Spectral radiance for the 7325 nm channel (in W m-2 sr-1 microns-1)	2-D (3800x3264)[1] array
metim_08540	Spectral radiance for the 8540 nm channel (in W m-2 sr-1 microns-1)	2-D (3800x3264)[1] array
metim_10690	Spectral radiance for the 10690 nm channel (in W m-2 sr-1 microns-1)	2-D (3800x3264)[1] array
metim_12020	Spectral radiance for the 12020 nm channel (in W m-2 sr-1 microns-1)	2-D (3800x3264)[1] array
metim_13345	Spectral radiance for the 13345 nm channel (in W m-2 sr-1 microns-1)	2-D (3800x3264)[1] array

Table 5.3: List and description of datasets for VII radiances files

[1] 3800 = along-track pixels of a granule (=100 scans), 3264 is the number of across-track pixels.

5.3 Details on delivered data files

5.3.1 List of delivered 3MI and VII files

A complete list of delivered data has been established and is included in the data delivery note.

5.3.2 Information on additional test files

In addition to the realistic atmospheric and surface conditions provided by the master AVHRR test orbits, we have produced four additional test granules for both 3MI and VII in order to provide somehow more extreme observation conditions.

The selected granules corresponds to the following references :

VII	3MI
2007-09-12T08-57-15 2008-02-23T08-50-47	2007-09-12T08-58-27 2008-02-23T08-51-10

A first scenario has been computed for fully clear granules where cloud cover has been removed.

A second scenario has been computed for fully clear granules again but with aerosol optical thicknesses multiplied by 4 in order to enhance the aerosol signal.

The 4 granules are clearly identified in the delivered dataset through decorated radiance file names referring to “clear_sky” and “heavy_aerosols”.

6 List of Acronyms and parameters symbols

2T	Temperature at altitude = 2m
3MI	Multi-Viewing, Multi-Channel, Multi-Polarization Imager
4MSDS	METImage/3MI Synthetic Dataset Simulator
ACE-2	Altimeter Corrected Elevations -2
Albe	Albedo (no unit, between 0 and 1)
AOD	Aerosol Optical Depth
ARTDECO	Atmospheric Radiative Transfer Database for Earth Climate Observation
AVHRR	Advanced Very High Resolution Radiometer (MeTop, EUMETSAT)
BPRDF	Bidirectional Polarised Reflectance Distribution Function
BRDF	Bidirectional Reflectance Distribution Function
CCI	Climate Change Initiative (ESA's initiative)
CGASA	Coefficients of Gas Absorption
CKD	Clough, Kneizys, and, Davies' continuum of absorption
CNES	Centre National d'Etudes Spatiales (French Space Agency)
COD	Cloud Optical Depth
CPU	Central Processing Unit
CS	Clear Sky
DEM	Digital Elevation Model
DISORT	Discrete-Ordinate-Method of Radiative Transfer.
ECI	Earth Centred Inertial (Coordinates)
ECR	Earth Centred Rotating (Coordinates)
ECMWF	European Centre for Medium-Range Weather Forecasts
Em	Emissivity (no unit, between 0 and 1)
ENVISAT	Environmental Satellite (ESA)
EPS-SG	EUMETSAT Polar System – Second Generatin
ESA	European Space Agency
EUMETSAT	European Organisation for the Exploitation of Meteorological Satellites
FASDOM	Fast radiative transfer modelling with Discrete Ordinate Method
FOV	Field Of View
FUB	Freie Universität Berlin
HDF	Hierarchical Data Format
HITRAN	High-Resolution transmission molecular database
ICARE	Cloud-Aerosol-Water-Radiation Interactions (http://www.icare.univ-lille1.fr)
IFOV	Instantaneous Field of View
IPLT	Input Parameters and Limits Table

ISS	Institute for Space Sciences (FUB)
IWV	Integrated Water Vapour (in mm)
IWVC	Integrated Water Vapour Content (in mm)
IWVP	Integrated Water Vapour Path (water vapour column in mm)
k	Extinction coefficient of the gases (in m^{-1})
k_i	Extinction coefficient of the bin i
KISS	k-distribution of Institute for Space Sciences
LBL	Line-by-line
LBLDOM	Line-by-line radiative transfer modelling with Discrete Ordinate Method
LOA	Laboratoire d'Optique Atmosphérique (Université de Lille-1)
LUT	Look up Table
MACC	Monitoring Atmospheric Composition and Climate
MERIS	Medium Resolution Imaging Spectrometer (ENVISAT, ESA)
MODIS	Moderate-resolution Imaging Spectroradiometer (Aqua and Terra of NASA)
MOMO	Matrix-Operator Model
MSSA	Mid-Latitude Summer Standard Atmosphere
MTCKD	Mlawer, Tobin, Clough, Kneizys, and, Davies' continuum of absorption
NASA	National Aeronautics and Space Administration
NYA	Not Yet Attributed
OAA	Observation Azimuth Angle
OZA	Observation Zenith Angle
PARASOL	Polarization & Anisotropy of Reflectances for Atmospheric Sciences coupled with Observations from a Lidar (CNES, A-Train) POLDER Polarization and Directionality of the Earth's Reflectances
POLDER	Polarization and Directionality of the Earth's Reflectances
RGB	Red-Green-Blue
RTE	Radiative Transfer Equation
SAA	Solar Azimuth Angle
SKT	Skin Temperature (in K)
SSA	Single Scattering Albedo (ω_0)
SWIR	Short-Wave Infrared (channels of 3MI)
SWSA	Subarctic Winter Standard Atmosphere
SZA	Solar Zenith Angle
T-2m	Temperature at altitude = 2m
TAI	Temps Atomique International (International)
TCC	Total Cloud Cover
TCWV	Total Column Water Vapour (in mm)
TLE	Two Lines Elements
TOA	Top of the Atmosphere

TRSA	Tropical Standard Atmosphere
VII	Visible and Infrared Imager (other name of METIMage)
VIS	VISible (wavelength)
VISNIR	VISible and Near Infrared (wavelength)
WP	Work Package
τ	Optical depth (no unit)
ω_0	Single Scattering Albedo (SSA)

7 List of references

Baum, B. A., P. Yang, A. J. Heymsfield, C. Schmitt, Y. Xie, A. Bansemer, Y. X. Hu, and Z. Zhang, 2011: Improvements to shortwave bulk scattering and absorption models for the remote sensing of ice clouds. J. Appl. Meteor. Clim., 50, 1037-1056.

Bennartz R, Fischer J. A modified k-distribution approach applied to narrow band water vapour and oxygen absorption estimates in the near infrared. J Quant Spectrosc Radiat Transfer 2000;66:539–53.

Clough SA, Kneizys FX, Davies RW. Line Shape and the Water Vapor Continuum. Atmos Res 1989;23:229-41.

Clough SA, Shephard MW, Mlawer EJ, Delamere JS, Iacono MJ, Cady-Pereira K, Boukabara S, Brown PD. Atmospheric radiative transfer modeling: a summary of the AER codes, Short Communication. J Quant Spectrosc Radiat Transfer 2005;91:233–44.

Cox C, Munk W. Measurements of the roughness of the sea surface from photographs of the sun's glitter. J Opt Soc Am 1954;44(11):838}50.

Doppler L, Preusker R, Bennartz R, Fischer J. k-bin and k-IR: k-distribution methods without correlation approximation for non-fixed instrument response function and extension to the thermal infrared. Applications to satellite remote sensing. J of Quant Rad Transfer 2014;133:382-395.

Dubovik, O., B. N. Holben, T. F. Eck, A. Smirnov, Y. J. Kaufman, M. D. King, D. Tanre, and I. Slutsker (2002a), Variability of absorption and optical properties of key aerosol types observed in worldwide locations, J. Atmos. Sci., 59, 590–608.

Dubuisson P, Buriez JC, Fouquart Y. High Spectral Resolution Solar Radiative Transfer in Absorbing and Scattering media, application to the satellite simulation. J Quant Spectros Radiat Transfer 1996;55:103-126.

Dubuisson P, Giraud V, Chomette O, Chepfer H, Pelon J. Fast Radiative transfer modeling for infrared imaging radiometry. J Quant Spectrosc Radiat Transfer 2005;95:201–20 .

Dubuisson P., D. Dessailly, M. Vesperini and R. Frouin, Water Vapor Retrieval Over Ocean Using Near-IR imagery, J. Geophys. Res., 109, D19106, doi:10.1029/2004JD004516, 2004.

Friedl, M. A., Sulla-Menashe, D., Tan, B., Schneider, A., Ramankutty, N., Sibley, A., andHuang, X. (2010). MODIS Collection 5 global land cover: Algorithm refinements and characterization of new datasets. Remote Sensing of Environment, 114, 168–182

Fell F, Fischer J. Numerical simulation of the light field in the atmosphere-ocean system using the matrix-operator method, J Quant Spectrosc and Radiat Transfer 2001;69:351-88.

Fischer J, Grassl H. Radiative transfer in an atmosphere-ocean system: an azimuthally dependent matrix-operator approach. Applied Optics 1984;23(7):1031-39.

Fu Q, Liou KN: On the Correlated k-Distribution Method for Radiative Transfer in Nonhomogeneous Atmospheres. J Atm Sc 1992;49(22):2139-56.

de Haan JF, et al. The adding method for multiple scattering calculations of polarized light , A&A 1987;183, 371-391

García O.E., J. P. Ďıaz, F. J. Expósito, A. M. Dıaz, O. Dubovik, Y. Derimian, P. Dubuisson, and J.-C. Roger, Shortwave Radiative Forcing and Efficiency of Key Aerosol Types using AERONET Data, Atmos. Chem. Phys., 12, 5129–5145, 2012 doi:10.5194/acp-12-5129-2012

Garnier A., Pelon J., Dubuisson P., Faivre M., Chomette O., Pascal N., Kratz D. P., Retrieval of cloud properties using CALIPSO Imaging Infrared Radiometer. Part I: effective emissivity and optical depth , Journal of Applied Meteorology and Climatology, 2012.

Garnier A., Pelon J., Dubuisson P., Yang P., Faivre M., Chomette O., Pascal N., Lucker P., Murray T. Retrieval of cloud properties using CALIPSO Imaging Infrared Radiometer. Part II: effective diameter and ice water path, Journal of Applied Meteorology and Climatology 52, 11 (2013)

Heidinger, A.K., A.T. Evan, M.J. Foster, and A. Walther 2012. A naïve Bayesian cloud-detection scheme derived from CALYPSO and applied within PATMOS-x. Journal ofApplied Meteorology and Climatology, 51:1129 – 1144

Hess, M., P. Koepke, I. Schult, 1998: Optical Properties of Aerosols and Clouds: The Software Package OPAC. Bull. Amer. Meteor. Soc., 79, 831–844.

Hollstein A, Fischer J. Radiative transfer solutions for coupled atmosphere ocean systems using the matrix operator technique. J Quant Spectrosc Radiat Transfer 2012;113:536-548.

Kokhanovsky, Alexander A., et al. "Benchmark results in vector atmospheric radiative transfer." Journal of Quantitative Spectroscopy and Radiative Transfer 2010;111(12): 1931-1946.

Kurucz, R.L., Synthetic infrared spectra, in Infrared Solar Physics, IAU Symp. 154, edited by D.M. Rabin and J.T. Jefferies, Kluwer, Acad., Norwell, MA, 1992.

Lacis AA, Oinas V. A description of the correlated k-distribution method for modeling nongray gaseous absorption, thermal emission, and multiple scattering in vertically inhomogeneous atmospheres. J of Geophys Res 1991;96(D5): 9027-63.

Maignan F, FM Bréon, R Lacaze. Bidirectional reflectance of Earth targets: Evaluation of analytical models using a large set of spaceborne measurements with emphasis on the Hot Spot. Rem Sens Env 2004;90:210-220.

Mallet M., V. Pont, C. Liousse, L. Gomes, J. Pelon, S. Osborne, J. Haywood, J.C. Roger, P. Dubuisson, A. Mariscal, V. Thouret and P. Goloub, Aerosol direct radiative forcing over Djougou (northern Benin) during the AMMA dry season experiment, J. Geophys. Res., 113, D00C01, doi:10.1029/2007JD009419, 2008.

McClatchey RA, Fenn RW, Shelby JEA, Voltz FE, Garing JS. Optical properties of the atmosphere. Research paper AFCRF-72-0497, 1972, Hanscom Air Force Base, Bedford, 1972. 108p.

Pavolonis, Michael J.; Heidinger, Andrew K. and Uttal, Taneil. 2005: Daytime global cloud typing from AVHRR and VIIRS: Algorithm description, validation, and comparisons. Journal of Applied Meteorology, Volume 44, Issue 6, 2005, pp.804-826.

Pavolonis, Michael J. and Heidinger, Andrew K.. 2004: Daytime cloud overlap detection from AVHRR and VIIRS. Journal of Applied Meteorology, Volume 43, Issue 5, 2004, pp.762-

77

Péré J.C., A. Colette, P. Dubuisson, B. Bessagnet, M. Mallet, V. Pont, Impacts of future air pollution mitigation strategies on the aerosol direct radiative forcing over Europe, http://dx.doi.org/10.1016/j.atmosenv.2012.08.046, Atmospheric Environment 62, 451-460, 2012.

Plass G, Kattawar G, Catchings F. Matrix-operator theory of radiative transfer. 1: Rayleigh scattering. Applied Optics 1973;12(2):314-29.

Rothman LS, Gordon IE, et al. The HITRAN 2008 molecular spectroscopic database. J of Quant Spectrosc and Radiat Transfer 2009;110(9–10):533-72.

Schaaf, C. B., F. Gao, A. H. Strahler, W. Lucht, X. Li, T. Tsang, N. C. Strugnell, X. Zhang, Y. Jin, J.-P. Muller, P. Lewis, M. Barnsley, P. Hobson, M. Disney, G. Roberts, M. Dunderdale, C. Doll, R. d'Entremont, B. Hu, S. Liang, and J. L. Privette, and D. P. Roy,First Operational BRDF, Albedo and Nadir Reflectance Products from MODIS, Remote Sens. Environ., 83, 135-148, 2002.

Schaaf, C. L. B., J. Liu, F. Gao and A. H. Strahler, MODIS Albedo and Reflectance Anisotropy Products from Aqua and Terra, In Land Remote Sensing and Global Environmental Change: NASA's Earch Observing System and the Science of ASTER and MODIS, Remote Sensing and Digital Image Processing Series, Vol.11, B. Ramachandran, C. Justice, M. Abrams, Eds, Springer-Cerlag, 873 pp.,2011.

Sicard M., M Mallet, D García-Vizcaíno, A Comerón, F Rocadenbosch, P Dubuisson and C Muñoz-Porcar, Intense dust and extremely fresh biomass burning outbreak in Barcelona, Spain: characterization of their optical properties and estimation of their direct radiative forcing, doi:10.1088/1748-9326/7/3/034016, 2012 Environ. Res. Lett. 7 (034016), 2012.

Stamnes K, Tsay SC, Wiscombe W, Jayaweera K. Numerically stable algorithm for discrete-ordinate-method radiative transfer in multiple scattering and emitting layered media. Applied Optics 1988;27(12).

West R, Goody R, Chen L, Crisp D. The correlated-k method and related methods for broadband radiation calculations. J Quant Spectrosc and Radiat Transfer 2010;111:1672-1673.

Yang P, H Wei, HL Huang, BA Baum, YX Hu, GW Kattawar, MI Mishchenko and Q Fu. Scattering and absorption property database for nonspherical ice particles in the near-through far-infrared spectral region. Applied Optics 2005;44:5512:523.